2018

Spatial characteristics of the midnight temperature maximum and equatorial spread F from multi-instrument and magnetically conjugate observations

BOSTON UNIVERSITY

GRADUATE SCHOOL OF ARTS AND SCIENCES

Dissertation

SPATIAL CHARACTERISTICS OF THE MIDNIGHT TEMPERATURE MAXIMUM AND EQUATORIAL SPREAD F FROM MULTI-INSTRUMENT AND MAGNETICALLY CONJUGATE OBSERVATIONS

by

DUSTIN A HICKEY

B.A., Colby College, Waterville, ME, 2011
M.A., Boston University, Boston, MA, 2014

Submitted in partial fulfillment of the

requirements for the degree of

Doctor of Philosophy

2018

Approved by

First Reader

Carlos R. Martinis, PhD
Professor of Astronomy

Second Reader

Joshua L. Semeter, PhD
Professor of Electrical and Computer Engineering

Acknowledgments

I would like to thank my advisor, Carlos Martinis, for all of your help and support along the way. I would like to my committee for their input on this dissertation.

Thank you to all the graduate students in the department for being great friends and supportive colleagues.

Thank you to my parents, Dan and Susan Hickey, for their unwavering support for all my time in school.

A final thanks to my fiancèe, Eliza Carrera, for supporting me through all these years of graduate school.

SPATIAL CHARACTERISTICS OF THE MIDNIGHT TEMPERATURE MAXIMUM AND EQUATORIAL SPREAD F FROM MULTI-INSTRUMENT AND MAGNETICALLY CONJUGATE OBSERVATIONS

DUSTIN A HICKEY

Boston University, Graduate School of Arts and Sciences, 2018

Major Professor: Carlos Martinis, Professor of Astronomy.

ABSTRACT

The upper atmosphere, a region above ∼85 km called the ionosphere and thermosphere, has been studied extensively for over one hundred years. Measurements were often considered in isolation, but today, advances in technology and ground-based distributed arrays have allowed concurrent multi-instruments measurements. In this dissertation, I combine measurements from all-sky imagers (ASIs), coherent scatter radars, incoherent scatter radars (ISRs), and Fabry-Perot interferometers (FPIs). I focus on two phenomena, the midnight temperature maximum (MTM) and equatorial spread F (ESF), using observations from equatorial to mid-latitudes. The spatial characteristics of these phenomena are not fully understood. I combine observations at various latitudes and longitudes to extend MTM detection to mid-latitudes. I present the first simultaneous detections of the MTM at multiple altitudes and latitudes over North America and the first observations below the F-region peak using the Millstone Hill Observatory ISR in a south pointing, low-elevation mode. The

MTM can also be observed with an ASI and I present concurrent measurements of the MTM with an ASI and ISR. The Whole Atmosphere Model, a global circulation model, was found to be consistent with these observations. This further verifies that the MTM is partially created by lower atmospheric tides, demonstrating coupling between the lower and upper atmosphere. In addition to the MTM, I investigate different aspects of ESF using ASIs concurrently with other instruments. I compare various scale sizes (sub-meter to kilometers) using coherent scatter radar and an ASI and conclude that the lower hybrid drift instability causes radar echoes to occur preferentially on the western wall of large-scale depletions. The source of day-to-day variability in ESF is not fully known but I show that one driver may be large-scale wave structures ($\sim$400 km) that modulate the development of ESF. Finally, I compare concurrent observations of ESF plasma depletions with ASIs at magnetically-conjugate foot points and show how the magnitude and structure of the Earth's magnetic field is responsible for differences in the morphology and velocity of these depletions. In summary, I have used multi-instrument observations of ESF and the MTM to provide a deeper understanding of the dynamics of the upper atmosphere.

Contents

List of Tables

List of Figures

List of Abbreviations

AMISR	Advanced Modular Incoherent Scatter Radar
ASI	All-Sky Imager
BU	Boston University
BW	Brightness Wave
C/NOFS	Communications Navigation Outage Forecast System
EAR	Equatorial Atmosphere Radar
EIA	Equatorial Ionization Anomaly
ESF	Equatorial Spread F
EUV	Extreme Ultraviolet
F10.7	Solar Radio Flux at 10.7 cm
FOV	Field of View
FPI	Fabry-Perot Interferometer
GPS	Global Positioning System
GRT	Generalized Rayleigh-Taylor instability
HWM	Horizontal Wind Model
IDEA	Integrated Dynamics in the Earth's Atmosphere
IGRF	International Geomagnetic Reference Field
IRI	International Reference Ionosphere
ISR	Incoherent Scatter Radar
JULIA	Jicamarca Unattended Long-term Investigations of the Ionosphere and Atmosphere
LT	Local Time

LISN	Low-latitude Ionospheric Sensor Network
LSWS	Large Scale Wave Structure
MTM	Midnight Temperature Maximum
MH	Millstone Hill
NATION	North American Thermosphere Ionosphere Observing Network
NRL	Naval Research Laboratory
NRLMSISE	Naval Research Laboratory Mass Spectrometer
	Incoherent Scatter Exosphere
PARI	Pisgah Astronomical Research Institute
PRE	Pre-reversal enhancement
RTI	Range-Time-Intensity
RTDI	Range-Time-Doppler-Intensity
SAMI3	SAMI is Another Model of the Ionosphere in 3D
SNR	Signal to Noise Ratio
TEC	Total Electron Content
TECU	Total Electron Content Units (10^{16} e^{-}/m^{2})
UT	Universal Time
UV	Ultraviolet
WAM	Whole Atmosphere Model

Chapter 1

Introduction

1.1 Motivation

The upper atmosphere of the Earth differs from the rest of the atmosphere due to the presence of ionized species within it. The ionized region is known as the ionosphere and was first postulated to exist by Carl Gauss in 1839 to explain variations in the Earth's magnetic field (*Glassmeier and Tsurutani*, 2014). In the early 1900s Guglielmo Marconi successfully transmitted a radio message across the Atlantic Ocean and Oliver Heaviside and Arthur Kennelly predicted the presence of the ionosphere that explained Marconi's work (*Green*, 1974). The presence of the ionosphere was finally confirmed in 1925 by Edward Appleton (*Appleton and Barnett*, 1925). Since this time it has been studied extensively but due to its complex nature there are many aspects of the ionosphere that are not understood.

In this dissertation I focus on two features of the ionosphere, equatorial spread F (ESF) and the midnight temperature maximum (MTM). I analyze these phenomena to understand their formation, morphology, evolution, and influence on the overall upper atmospheric system. Measurements have often been considered in isolation, but I take advantage of advances in technology and ground-based distributed arrays that have allowed concurrent measurements with multiple instruments.

The work in this dissertation answers the following three major questions along with providing many other contributions to the field.

1. *What are the characteristics of the midnight temperature maximum on a global scale?*

2. *What are the characteristics of large-scale (10-500 km) ESF plasma density structures and how do they relate to small-scale (0.3-3 m) density irregularities?*

3. *To what extent does the Earth's magnetic field influence magnetically conjugate observations of ESF?*

The answers to these questions not only further the knowledge of equatorial spread F and the midnight temperature maximum but also begin to probe other aspects of the ionosphere such as its day-to-day variability and coupling with the lower atmosphere.

In the rest of this chapter I provide context and background on the ionosphere and these two phenomena. In Chapter 2 I focus on the instrumentation and models used in the work presented here. The following three chapters present the work that I have done and I finish with a summary and conclusions.

1.2 Earth's thermosphere and ionosphere

The Earth's neutral atmosphere is typically divided into four vertical regions by the temperature profile in that region. The troposphere is the bottom layer and extends from the ground to about 15 km. In this region the temperature decreases with altitude. Above the troposphere is the stratosphere that extends from about 15 km to 50 km. In this region the presence of ozone causes the temperature to increase. The mesosphere extends from about 50 km to 85 km. The bottom of the mesosphere is the local peak in temperature and throughout this region the temper-

ature decreases. The thermosphere is above the mesosphere and starts at around 85 km and extends up to around 1000 km. The upper part of the thermosphere, about 600 km and above, is referred to as the exosphere. In this region particles have enough energy to escape Earth's gravity. Figure 1.1 shows the temperature profile of the atmosphere, from the Naval Research Laboratory Mass Spectrometer and Incoherent Scatter Radar (NRLMSISE-00) model, and the different regions described in this paragraph.

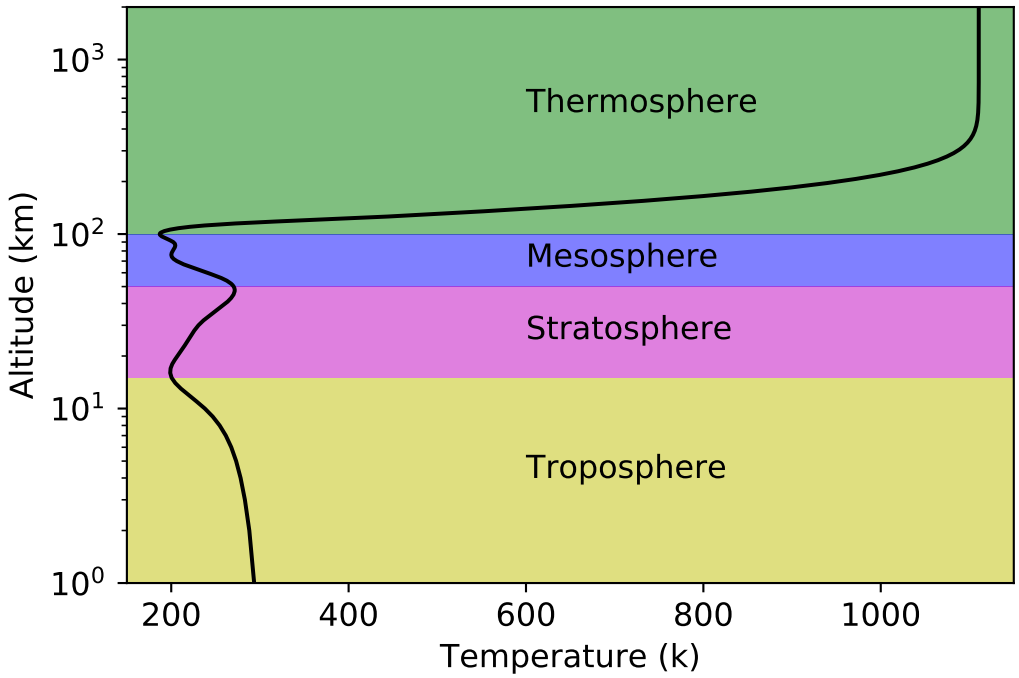

Fig. 1.1: An example of a temperature profile in the Earth's atmosphere. The altitude scale is logarithmic to show all the regions of the atmosphere. Temperatures are from the NRLMSISE-00 model. This an example of the atmosphere during the day in the equatorial region.

The thermosphere, the neutral component of the upper atmosphere, increases in temperature and reaches high temperatures because this region of the atmosphere is absorbing ultraviolet (UV) and extreme ultraviolet (EUV) radiation from the sun.

Temperatures in the thermosphere range from around 700 K to 2500 K. The difference between the night and day temperature can be over 200 K.

The majority of the thermosphere is above the turbopause, the boundary that separates the homosphere from the heterosphere. In the homosphere, also known as the turbosphere, the atmosphere is well mixed by turbulence so the relative composition does not depend on altitude. In the heterosphere the particles are able to diffuse faster than they are mixed by turbulence and they begin to separate according to their masses. The heavier species are more prevalent at lower altitudes.

Figure 1.2 shows a model of the upper atmosphere from 60 km to 1000 km. This figure is made using outputs from two models, the International Reference Ionosphere (IRI-2016) and the NRLMSISE-00 model of the neutral atmosphere. These are empirical climatological models. The solid lines show the major neutral species of the upper atmosphere. The dashed lines show the major ion species of the atmosphere. This graph is showing an example of the upper atmosphere during the day.

The major constituents of the thermosphere are molecular nitrogen (N_2, blue line), molecular oxygen (O_2, green line), and atomic oxygen(O, red line). Some other minor species shown here are atomic nitrogen (N, dashed gray line), helium (He, dashed turquoise line), and Hydrogen (H, dashed yellow line). As seen in Figure 1.2, at altitudes above about 200 km atomic oxygen is the dominant gas and then around 700 km the dominant gas is helium. Above 1000 km hydrogen starts to become the dominant gas. Atomic nitrogen is always a minor species and has a maximum around 200 km.

Within the thermosphere and mesosphere is the ionosphere, the ionized part of the Earth's atmosphere. During the day the ionosphere extends from about 60 km up to about 1000 km. Above 1000 km hydrogen becomes the dominant ion and the region above this altitude is referred to as the protonosphere. The EUV radiation

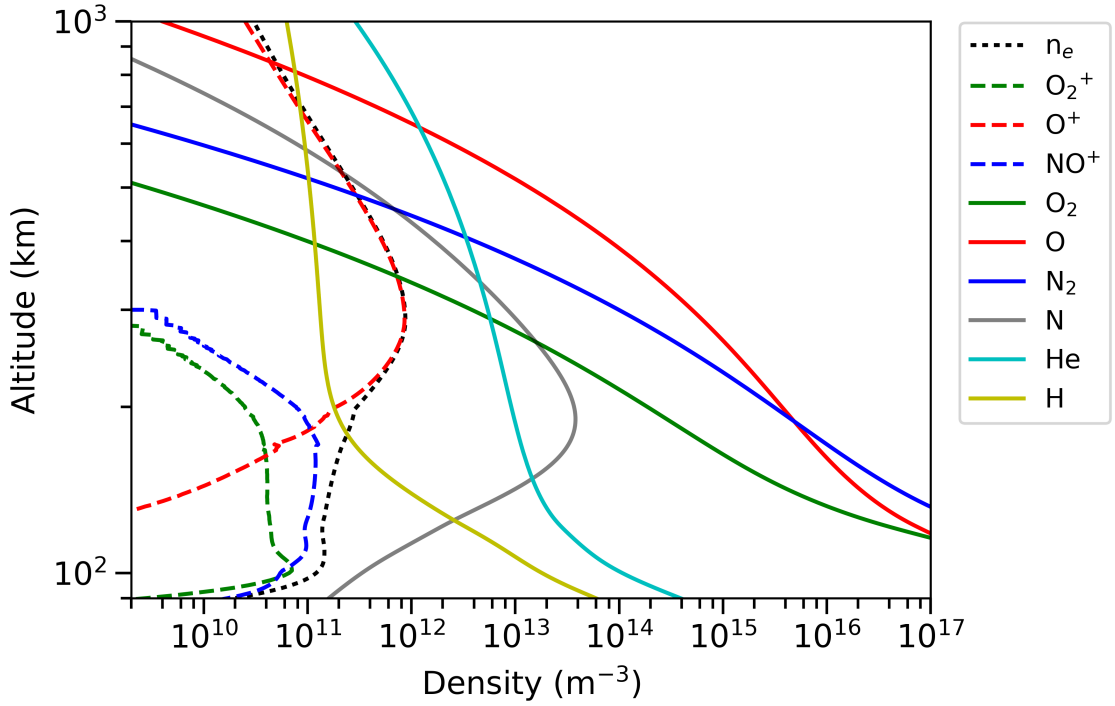

Fig. 1.2: Densities of the major neutral and ion species in the thermosphere and ionosphere. Ions are dashed lines and neutral species are solid lines. Electron density is also shown as the black dotted line. The neutral densities are determined using NRLMSISE-00 and the ion densities are determined using IRI-2016. This an example of the upper atmosphere during the day in the equatorial region.

that is responsible for heating the thermosphere is also the source of ionization. Photons with high enough energy are able to ionize the gas in the upper atmosphere. The region around the maximum density of the ionosphere is the F region. In Figure 1.2 this occurs around 300 km. In this region O^+ is the dominant ion (dashed red line). Below the peak and where the molecular ions, O_2^+ (dashed blue line) and NO^+ (dashed green line), dominate is the E region. There is a local maximum in the E region near 100 km. The region below the E peak is the D region of the ionosphere.

1.3 Equatorial, low-latitude, and mid-latitude regions

The upper atmosphere of the Earth is frequently separated into regions based on latitude due to the different processes that occur there. These regions, especially when referring to the ionosphere, are often defined using magnetic latitude because of the influence that the magnetic field has on the ionosphere. In this dissertation I will be focusing on the equatorial, low-latitude, and mid-latitude regions. These do not have definite boundaries and the processes that are mostly confined to one region can sometimes overlap into other regions. For the purpose of this thesis approximate magnetic latitudes will be provided.

The equatorial and low-latitude ionospheric regions are the areas close to the magnetic equator of the Earth. The equatorial region is confined to about $\pm 5^\circ$ around the magnetic equator and the low-latitude region usually extends to $\pm 10^\circ - 20^\circ$. The Earth's magnetic field is approximately a dipole that is tilted by about 11° and as a result the geographic and geomagnetic equators are usually not in the same location. The magnetic equator is where the field lines are horizontal and this leads to unique processes.

The horizontal field at the magnetic equator plays a crucial role in the physics of the equatorial region. It creates a particular interaction with the eastward and westward electric fields in these regions. These electric fields are driven by the neutral winds in these regions that separate the ions and electrons. The electric fields then in turn create an $\mathbf{E} \times \mathbf{B}$ drift in the plasma. During the day there are strong eastward electric fields that combined with the horizontal electric field create an upward drift of the plasma. One consequence of this upward drift is the formation of the equatorial ionization anomaly (EIA). The EIA is a persistent feature of the low latitude ionosphere (*Appleton*, 1946). The upwelling ionospheric plasma created by the electric fields that then follows the magnetic field as it descends, moving it away

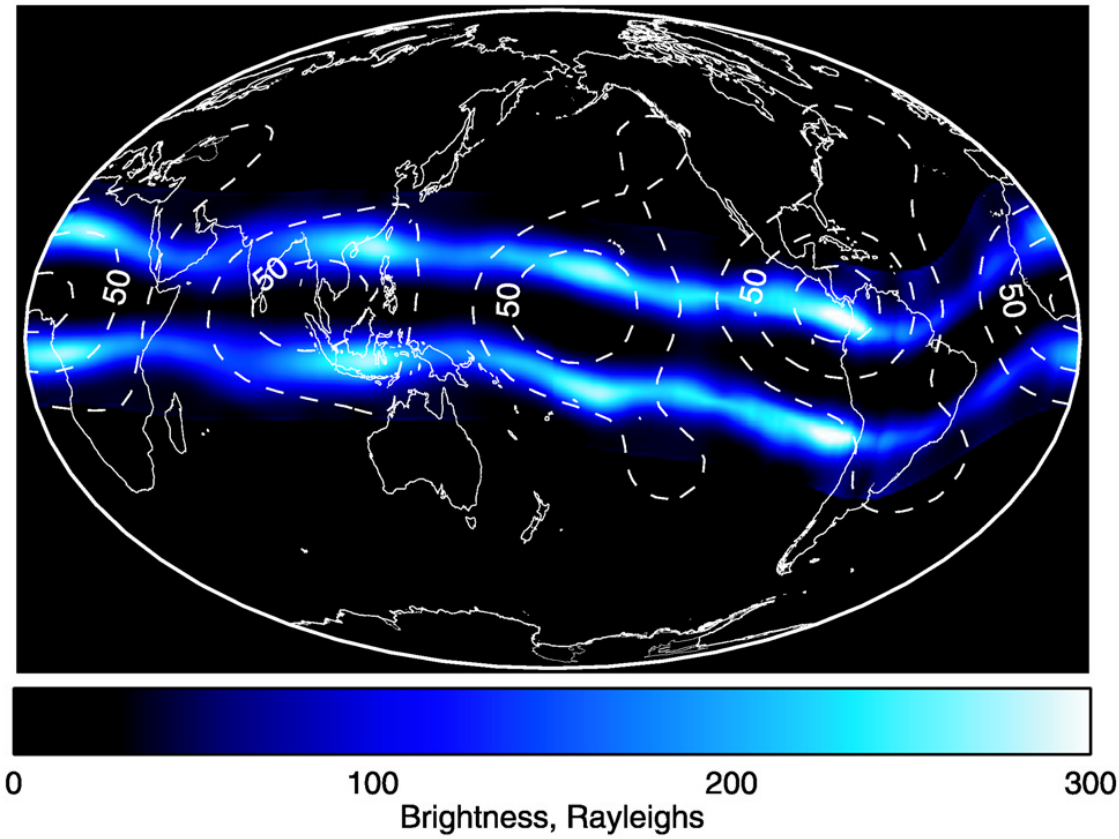

Fig. 1.3: Atmospheric emissions from 30 days of observations from the IMAGE-FUV imager. The crests of the EIA are visible at all longitudes. Due to poor sampling of the southern crest of the EIA, the southern crest in this image is a represented as a mirror of the northern crest.(*Immel et al.*, 2006)

from the magnetic equator. This creates a trough at the magnetic equator and two crests to the north and south that are typically 10° to 20° of latitude away. Figure 1.3 shows the crests of the EIA measured with the IMAGE-FUV imager. There is variability of the EIA throughout the day and it has day-to-day, seasonal, and solar cycle variability. Additionally, there is longitudinal variability that is attributed to atmospheric forcing from atmospheric tides, planetary waves, and atmospheric gravity waves. These drivers also impact the day-to-day variability. When observing the crest-to-trough ratio there are typically two maxima, one during the day, due to a

daytime eastward electric field, and one during post-sunset (*Yue et al.*, 2015), due to the pre-reversal enhancement (PRE) of the electric field after sunset (*Kelley et al.*, 2009).

The post-sunset PRE also is important in the creation of equatorial irregularities known as equatorial spread F. The upwelling of the ionosphere after sunset and the horizontal magnetic field can create the correct conditions for ESF to form. ESF is a major topic of this dissertation and will be discussed in more detail in the next section.

In addition to ESF another prominent low-latitude phenomena in the upper atmosphere and major focus of this dissertation is the midnight temperature maximum (MTM). The MTM is an increase in neutral temperature in the upper atmosphere that occurs around local midnight. Unlike ESF, the occurrence of the MTM is related to the Earth's geographic equator and not the geomagnetic equator. The MTM extends from low-latitudes to mid-latitudes.

The mid-latitude region of the Earth's upper atmosphere is the next region beyond the low-latitude region where the angle between the Earth's magnetic field is no longer near horizontal. Mid-latitudes typically cover from about 20° to 50° magnetic latitude. Impacts of ESF are typically constrained to low latitudes but come sometimes extend into the mid-latitude region. The MTM occurs throughout both the low-latitude and mid-latitude regions.

1.4 Perturbations in the upper atmosphere

Throughout the upper atmosphere there are many different perturbations. In this section I provide some background on and context to the two phenomena in the upper atmosphere that this dissertation is focused on, the MTM and ESF.

1.4.1 The midnight temperature maximum

The MTM is an increase in neutral temperature in the upper atmosphere. This increase of about 50 to 200 K creates a local maximum in the temperature near local midnight. The formation mechanism for the MTM is not fully understood but results from the Whole Atmosphere Model (WAM) indicate that the generation of the MTM may be largely due to effects from an upward propagating terdiurnal tidal wave (*Akmaev et al.*, 2009), in addition to other, smaller, nonlinear interaction effects.

The MTM has been measured remotely using Fabry-Perot interferometers (FPIs) (*Faivre et al.*, 2006) and incoherent scatter radars (ISR) (*Harper*, 1973; *Bamgboye and McClure*, 1982; *Oliver et al.*, 2012; *Martinis et al.*, 2013). FPIs are optical instruments used to measure neutral temperatures and winds around 250-300 km by computing the Doppler width and shift in 6300 Å airglow emissions. Figure 1.4 shows examples of the MTM observed with an FPI in Arequipa, Peru. FPIs measure the temperature at an altitude of around 250 km, with a spread of 25 km, using 6300 Å emission. While these measurements provide the temperature at just one altitude, ISRs can simultaneously measure ion and electron temperatures at night from ∼200 km to the top of the ionosphere. At night in the F region of the ionosphere, ion and electron temperatures become nearly equal to the neutral temperature, so a measure of the increase in ion temperature becomes a measure of the increase in neutral temperature (*Ruan et al.*, 2013). This allows the use of ISR techniques to provide information on the neutral MTM at other heights besides those measured by the FPI.

In addition to FPI and ISR measurements, there have also been in situ satellite observations of the MTM. Measurements from the Atmosphere Explorer-E satellite (*Herrero and Spencer*, 1982), covering the range from 20°S to 20°N, show the MTM at

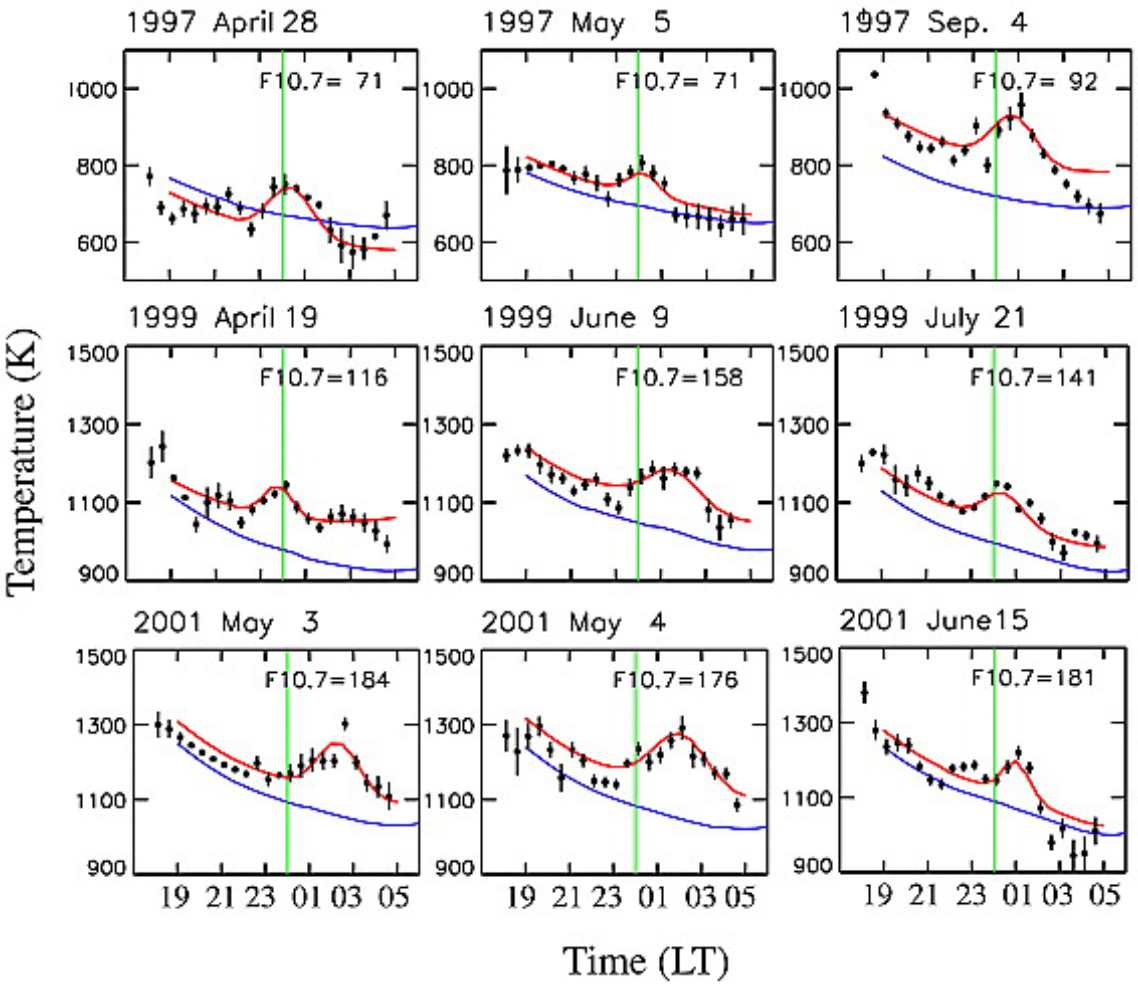

Fig. 1.4: Measurements of the MTM in neutral temperature using an FPI in Arequipa Peru. The neutral temperature is on the y axis and local time is on the x axis (*Faivre et al.*, 2006)

all of these latitudes. Figure 1.5 show these observations of the MTM during northern hemisphere summer. These satellite observations not only show the latitudinal extent of the MTM but also indicate that the MTM often occurs earlier at the equator and then later at higher latitudes. The earlier occurrence at lower latitudes is often described as a sideways V structure in longitude and latitude space.

The MTM has mostly been studied at low latitudes (*Meriwether et al.*, 2008), but recent model and observational results show that MTM effects can occur as high

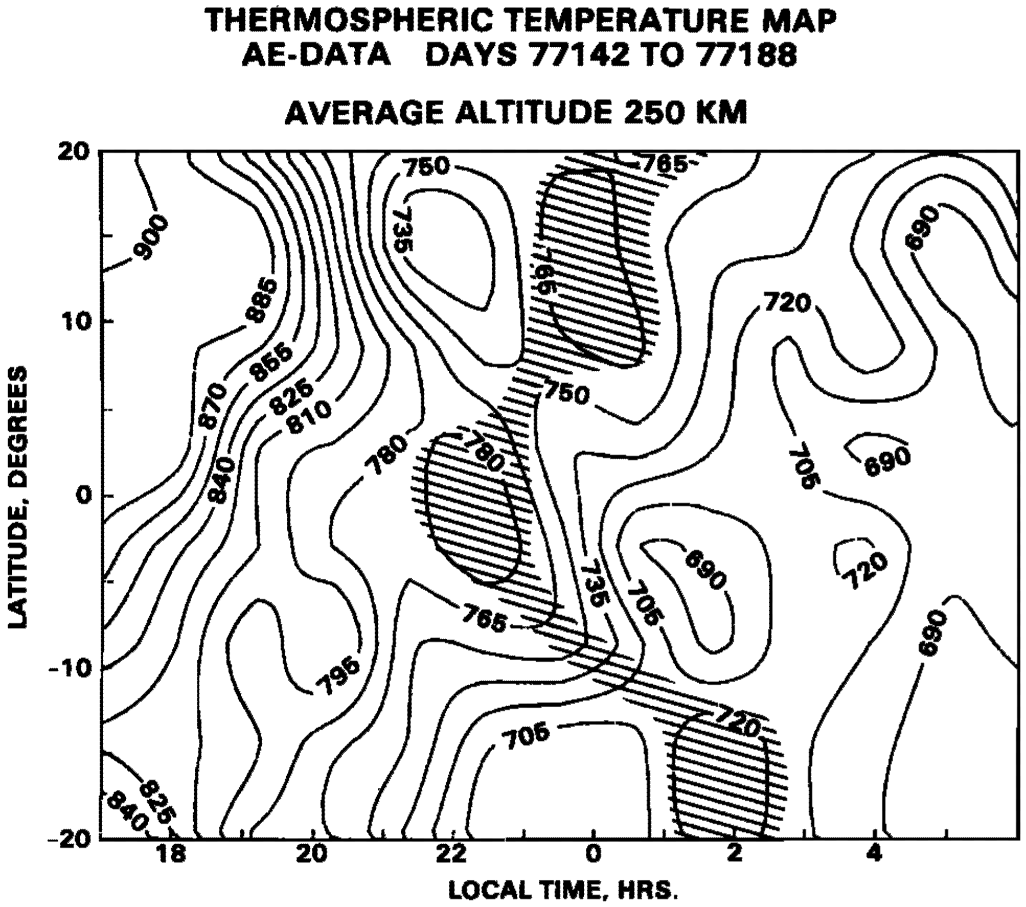

Fig. 1.5: A contour plot of thermospheric temperature with geographic latitude on the y-axis and and geographic longitude on the x-axis. The MTM is shown by shading. Data were collected from the Atmosphere Explorer-E satellite (*Herrero and Spencer*, 1982)

as ∼30° in both hemispheres (*Akmaev et al.*, 2009, 2010; *Martinis et al.*, 2006). Other recent studies show an enhancement in ion and neutral temperature at ∼40° N that could be attributed to the MTM (*Oliver et al.*, 2012; *Ruan et al.*, 2013).

Observations of the brightness wave, an optical signature of the MTM (*Colerico et al.*, 1996), by all-sky imagers have been used as evidence of the MTM occurring at mid-latitudes in the Southern Hemisphere. These optical signatures in airglow emissions at 6300 Å have been observed as far as 40°S (*Colerico et al.*, 2006).

Even though these previous studies have provided valuable measurements of the MTM there are still questions about its formation. WAM was the first model to reproduce a realistic MTM. In this model the formation of the MTM was traced to an upward propagating terdiurnal (8 h) wave in the lower atmosphere. The solar heating of the atmosphere is not simply sinusoidal and is thus a superposition of wave modes with different periods. These atmospheric tidal harmonics are analyzed in WAM to determine the source of the MTM (*Akmaev et al.*, 2009, 2010). The terdiurnal wave was found to be the main source of the MTM but the full MTM feature is a result of non-linear interactions with other tidal harmonics. As the three-peak terdiurnal wave propagates upward the two maxima are suppressed by increased dissipation during the day and only the maxima near midnight survives, resulting in the MTM. In *Akmaev et al.* (2009) it is postulated that the success of WAM over other models in reproducing the MTM is related to the interaction of other tidal harmonics with the terdiurnal wave, the vertical resolution of the model, and less imposed numerical dissipation in the thermosphere.

Measurements in the lower atmosphere that could provide observational insight into the source of MTM are very scarce, and the full generation mechanism of the MTM is not fully understood. The latitudinal extent of the MTM is also not well known due to the absence of concurrent MTM measurements at multiple latitudes. In this dissertation I will fill this gap in knowledge by analyzing measurements at multiple latitudes and altitudes, with multiple instruments. These measurements constrain the production mechanisms for the MTM and provide a way to assess the role of waves and tides in the coupling from the lower atmosphere to the upper atmosphere.

1.4.2 Equatorial spread F

ESF is the name commonly given to plasma irregularities that typically occur after sunset in the equatorial and low-latitude F region. These irregularities are attributed to plasma bubbles, depletions in the background plasma that begin to form due to the generalized Rayleigh-Taylor instability (*Hysell*, 2000). ESF was first observed in the 1930s (*Booker and Wells*, 1938) with an ionosonde in Peru and its name comes from the spreading of the signal observed with this instrument. Since then it has been studied extensively but there are still many aspects of it that are not fully explained (*Woodman*, 2009). ESF scales sizes cover a wide range, from hundreds of kilometers down to centimeters (*Kelley and Hysell*, 1991). The large-scale (kilometers to hundreds of kilometers) features consist of regions of lower plasma density and are referred to as plasma bubbles or depletions. When these depletions extend to the topside of the ionosphere they are often referred to as plumes. These large scale structures are flux tube integrated such that topside structures are also present at lower altitudes away from the magnetic equator. The small-scale density fluctuations are referred to as irregularities. Throughout this dissertation ESF will be used to refer to the overall process that includes both the large-scale and small-scale aspects.

The largest scale sizes of ESF are a result of the generalized Rayleigh-Taylor instability (GRT). A simplified expression of the growth rate from *Sultan* (1996) is shown in Equation 1.1.

$$\gamma = -\frac{g}{\nu_{in}}\frac{1}{n_e}\frac{\delta n_e}{\delta h} - Rs^{-1} \tag{1.1}$$

g is the gravitational acceleration (up is positive), ν_{in} is the ion neutral collision rate, n_e is the background electron density, h is altitude, and R is recombination rate. If the F-layer rises, the growth rate of the generalized Rayleigh Taylor instability increases because the smaller background neutral density at higher latitudes decreases both the

ion neutral collision rate and the recombination rate. A larger growth rate means that bottomside ESF is more likely to form. The rising of the ionosphere during the PRE, that also creates a maxima in the EIA, increases the growth rate of the GRT. This results in most ESF being observed just after sunset. The development of these large-scale structures is fairly well understood but the short-term (day-to-day) variability is not.

The GRT is the mechanism for the development of the large-scale structures but there are also many smaller scale sizes, ranging from hundreds of meters to centimeters. These smaller irregularities are related to the larger-scale structures, although the production method for some small-scale irregularities is not fully understood. It is often assumed that a cascade mechanism is responsible for the intermediate and small-scale irregularities but the exact method is still debated (*Woodman*, 2009). In this dissertation I discuss two instabilities that have been proposed in previous studies as the source of small-scale irregularities at 3 m and 0.3 m. The wind driven gradient drift instability has been proposed as a source of 3 m irregularities that occur within certain regions of the large-scale plasma depletions (*Miller et al.*, 2010; *Sekar et al.*, 2007). At the magnetic equator this instability can occur at night when there is a zonal neutral wind that is anti-parallel to the plasma density gradient. If there is a small perturbation in the plasma, the $\mathbf{U} \times \mathbf{B}$ drift creates a perturbation electric field that is unstable under these conditions and can produce 3m irregularities. The lower-hybrid-drift instability has been proposed for sub-meter irregularities (*Huba and Ossakow*, 1981b). This instability is an excitation of the lower hybrid oscillation propagating across magnetic field lines by the ion diamagnetic drift. A density gradient perpendicular to the magnetic field provides the diamagnetic drift. A sufficient density gradient must be present to excite the instability. The ions must be demagnetized in order to move across field lines, which puts a threshold on the densities

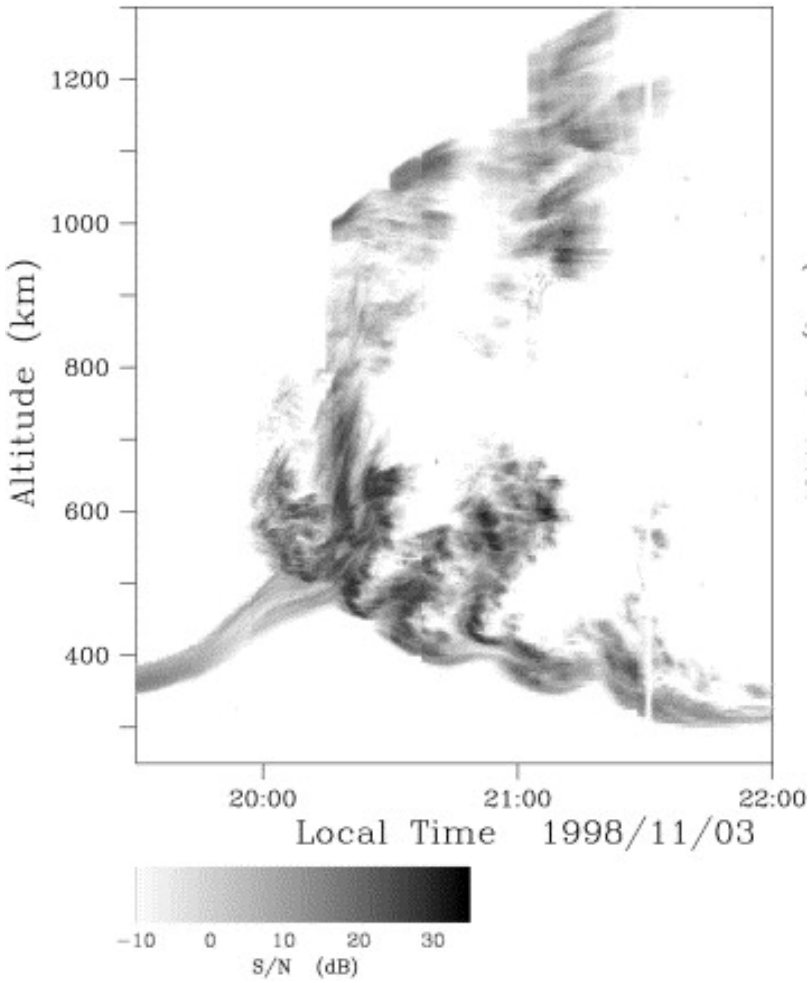

Fig. 1.6: Observations of ESF from the main radar at the Jicamarca Radio Observatory. The x-axis is altitude in km, the y-axis is time, and the gray scale shows the signal to noise ratio of the radar echoes from ESF (*Hysell*, 2000)

where this can occur. A more detailed analysis of the lower-hybrid-drift instability can be found in *Huba and Ossakow* (1981a).

Many observations of ESF have been done using coherent scatter radar. In this technique, the radar detects irregularities with scale sizes equal to half the radar wavelength. Figure 1.6 shows observations of ESF using coherent scatter radar in Jicamarca, Peru that measures structures with 3 m scale sizes.

Large-scale ESF structures (10-500 km) can also be observed as airglow depletions within the field of view of ASIs (*Weber et al.*, 1978). These structures are regions that have less plasma and thus are darker than the background. Depletions can be associated with three types of ESF: bottom-type, bottomside, and topside (*Woodman and La Hoz*, 1976). At the magnetic equator we observe bottomside ESF and these structures appear as dark bands oriented along magnetic field lines. Observations away from the magnetic equator measure topside ESF and are visible as bifurcated structures extending away from the magnetic equator. ESF processes are flux tube integrated (e.g., *Sultan*, 1996; *Weber et al.*, 1996; *Keskinen et al.*, 1998) so the topside structures at the magnetic equator map down to their magnetic foot points at higher latitudes (e.g., *Mendillo and Baumgardner*, 1982). Including northern and southern hemisphere coupling in simulations of ESF development produces a more accurate development of plasma bubbles (*Keskinen et al.*, 1998). The flux tube that contains the plasma bubble has low density all along the magnetic field lines from one hemisphere to the other. Figure 1.7 shows the 3-D nature of large-scale ESF bubbles and how the entire flux tube is depleted.

It is difficult to observe the full 3-D structure of ESF due to its large altitude and latitude extent. Many observations of ESF have only used one instrument yet the complex 3-D structure of ESF requires multiple instruments to fully understand. Although coherent scatter radars have provided valuable observations of ESF, their drawbacks come from the inability to capture large horizontal ESF structure and their lack of direct detection of the large-scale plasma bubbles formed by the GRT. Additionally, other studies have used space-based imaging to capture the latitudinal extent and morphology of the plasma bubbles but do not provide any altitude information and do not have fine resolution (*Kil et al.*, 2009). Satellite measurements of plasma density are used to measure the magnitude of the plasma density decrease

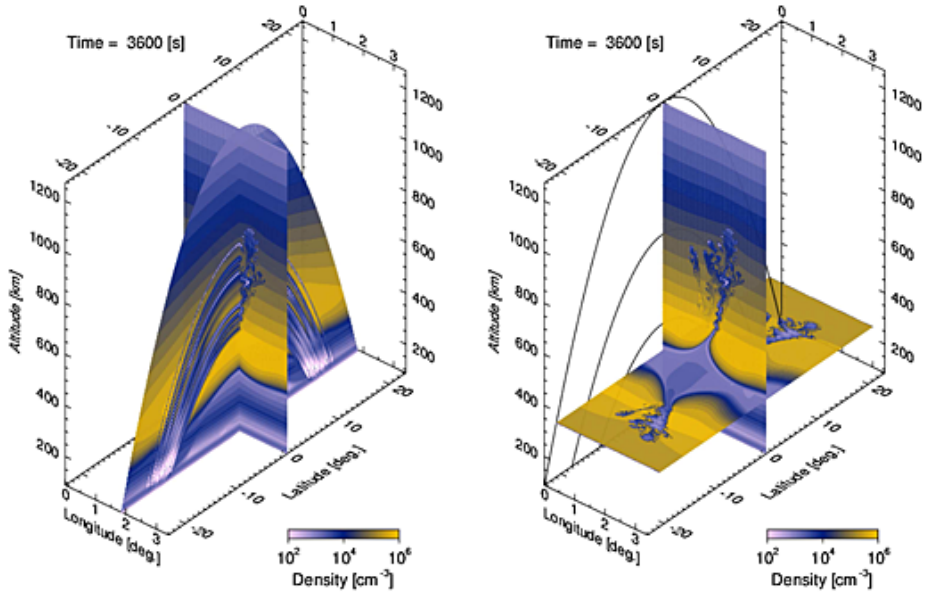

Fig. 1.7: A model of ESF showing how the structures are depleted all along the magnetic flux tubes. (*Yokoyama et al.*, 2014)

and are used for determining morphology (*Rino et al.*, 2016). Challenges of observing ESF with satellites are that they are limited to one altitude and change position with time. Airglow observations provide large horizontal coverage of ESF. All-sky imagers (ASI) are often used to observe plasma depletions associated with ESF and their field of view covers an area with about a ∼2000 km diameter.

One of the reasons why it is so important to understand ESF is because it can disrupt communication and navigation signals. ESF irregularities cause the fading (scintillation) of trans-ionospheric radio signals, cause variations in the ionospheric delay of these signals, and cause Doppler spreading of over-the-horizon radar signals. As a result, ESF is known to degrade the performance of technological assets such as satellite-based systems used for global navigation (e.g. GPS) and communication (e.g., *Demyanov et al.*, 2012; *Kelly et al.*, 2014), and radar systems used to detect moving targets.

In this dissertation I use ASIs in combination with other instruments to observe ESF. I combine radar and optical observations to connect the small-scale irregularities with the large scale structures. Additionally, ASI observations are used to understand the formation and evolution of ESF.

1.5 Influence of the Earth's Magnetic field on the Ionosphere

The Earth's magnetic field is approximately a dipole that is tilted by about 11° from the Earth's rotation axis. The dipole configuration means that field lines that pass through the ionosphere in one hemisphere connect back to the ionosphere in the opposite hemisphere. Places in opposite hemispheres that share the same field line are know as conjugate locations.

As discussed in the previous section, ESF depletions are flux tube integrated. That means that ESF depletions are present at both footpoints of a magnetic field line. Although the Earth's magnetic field resembles a dipole it differs in ways that affect ESF. In particular, a region of the Earth's magnetic field known as the South Atlantic Anomaly differs significantly from a dipole. In this region the Earth's magnetic field is significantly weaker than at the conjugate location. The exact reason for this weak region is not fully understood but may be related to the interaction of the Earth's outer core and mantle (*Pinto et al.*, 1992). Figure 1.8 shows the inclination, declination, and total field strength of the Earth's magnetic field from the International Geomagnetic Reference Field 12 (IGRF-12). If the Earth's magnetic field was a dipole aligned with the rotation axis then the declination would zero everywhere, inclination would be constant with longitude at a given geographic latitude, and conjugate locations would have the same magnetic field strength. In can be seen from Figure 1.8 that none of these characteristics hold true for every location on Earth.

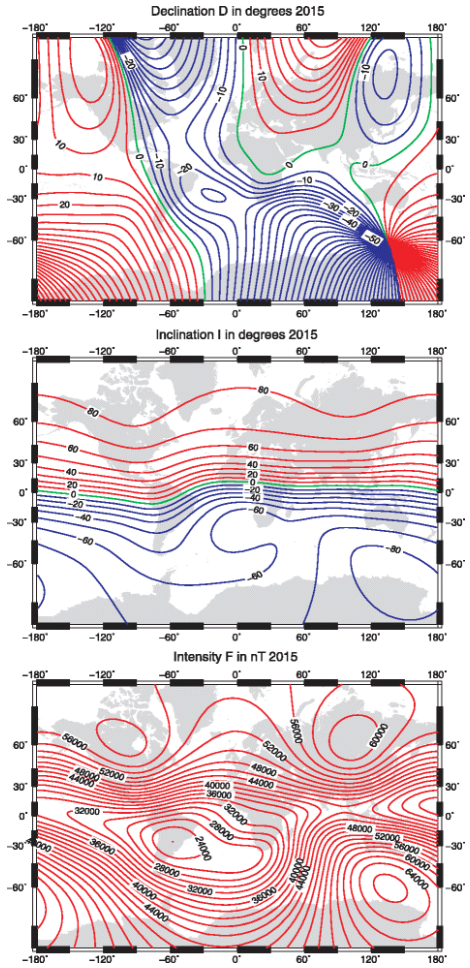

Fig. 1.8: Parameters of the Earth's magnetic in 2015 field from IGRF-12. (Top) Magnetic declination in degrees. (Middle) Magnetic inclination in degrees. (Bottom) Total field strength in NT (*Thébault et al.*, 2015)

The flux tube integrated nature of ESF means that variations in the magnetic field between conjugate points will impact the ESF structures. In this dissertation I compare and explain the differences in morphology and velocity of ESF structures observed at conjugate locations.

1.6 Scientific Contributions of this Work

In this dissertation I provide new insights into the MTM and ESF, both prominent upper atmospheric processes. I summarize here the major contributions that this work will provide.

- I expand the detection of the MTM, a prominent feature in the upper atmosphere, with radar to North America, showing that the Millstone Hill steerable incoherent scatter radar can be used for these measurements.

- I present new measurements of the MTM concurrently at multiple altitudes and latitudes. These measurements provide evidence for the source of the MTM.

- I show the advantages of using an all-sky imager concurrently with other instruments when observing ESF at the magnetic equator. All-sky imagers and radar systems complement each other by detecting aspects of ESF that the other cannot.

- The observations of ESF at the magnetic equator provide new information about the morphology and evolution of ESF. I show how the a large-scale wave structure may modify bottomside ESF depletions, I present a connection between the large-scale depletions and small-scale irregularities, and I present other new measurements of ESF morphology, variability, and evolution.

- I show a case study where the MTM interacts with ESF and turns an ESF depletion into an enhancement. This shows a connection between the two processes here that are often considered separately.

- With concurrent magnetically conjugate observations with all-sky imagers I demonstrate the advantages of this observational set up. I show how lining up conjugate features can constrain 6300 Å emission altitudes.

- I explain that the difference between ESF depletion morphology at conjugate sites is due to differences in the strength and morphology of the magnetic field and due to neutral winds. I show that differences in depletion velocity at conjugate sites is also due to differences in the strength and morphology of the magnetic field.

Together, these results provide new knowledge about the MTM and ESF and leads to a more complete understanding of the upper atmosphere.

Chapter 2

Instrumentation, data, and models

2.1 Instruments and data

In this dissertation I make use of observations from a variety of instruments. I often use multiple instruments concurrently in order to better understand the system I am studying. There are two categories of instruments included here, radar and optical. In addition to these I also discuss a few other instruments that supplement these observations.

2.1.1 Radar

Radar systems are key tools for studying the upper atmosphere of the Earth. The radar systems used in this dissertation both use radar scatter techniques. There are two types of scatter techniques that I discuss in this dissertation: incoherent scatter and coherent scatter.

Incoherent scatter radar (ISR) is used to measure characteristics of the ionosphere such as electron density, electron temperature, ion temperature, ion velocity, and composition. The major advantage of an ISR system is that it measures these parameters at multiple altitudes simultaneously. I present here a brief introduction to ISR. A more complete discussion of the theory can be found in (*Evans*, 1969).

ISR works by scattering off of electrons via Thomson scatter (*Evans*, 1969), the re-radation of incident electromagnetic waves by free electrons. The incident wave is produced by the radar transmitter and the backscatter is detected by the radar

receiver. The frequency of these waves are greater than the plasma frequency of the ionosphere so that the majority of the wave passes through the atmosphere. If electron temperature and ion temperature are constant, the received signal power is proportional to the density of electrons in the scattering region. The radar cross section of the scattering region is very small due to the very small classical radius of the electron. This means that a lot of power is necessary to operate an ISR. As a result, there are not many of these systems around the world.

In the ionosphere there are both free electrons and ions that are coupled together. The ions influence the motion of the electrons so that the properties of the returned spectra depends on both the properties of the ions and the electrons. In order to determine the parameters of the plasma a forward analytic model of the ionosphere is produced and then is fit to the received spectrum. From the best fit the plasma parameters can be determined. The returned spectra is double humped due to ion-acoustic waves moving toward and away from the receiver. Figure 2.1 shows a example of an ISR spectrum. This was produced using a model from the group at the MIT Haystack Observatory.

As mentioned previously, in this model the total power of the returned signal is dependent on the electron density. The line of sight velocity of the bulk plasma is determined from the Doppler shift of the entire spectrum. The rest of the parameters are not as straightforward to determine.

The returned spectrum is dependent on the ratio of the electron temperature to the ion temperature and the ratio of the ion temperature to the ion mass. This leads to some degeneracy in the solutions if all the parameters are allowed to be free. There are different approaches to breaking this degeneracy. In the F-region of the ionosphere O^+ is the dominant ion species and it is very reasonable to assume that all the mass in this region is equal to the mass of O^+. Once the ion mass is known then

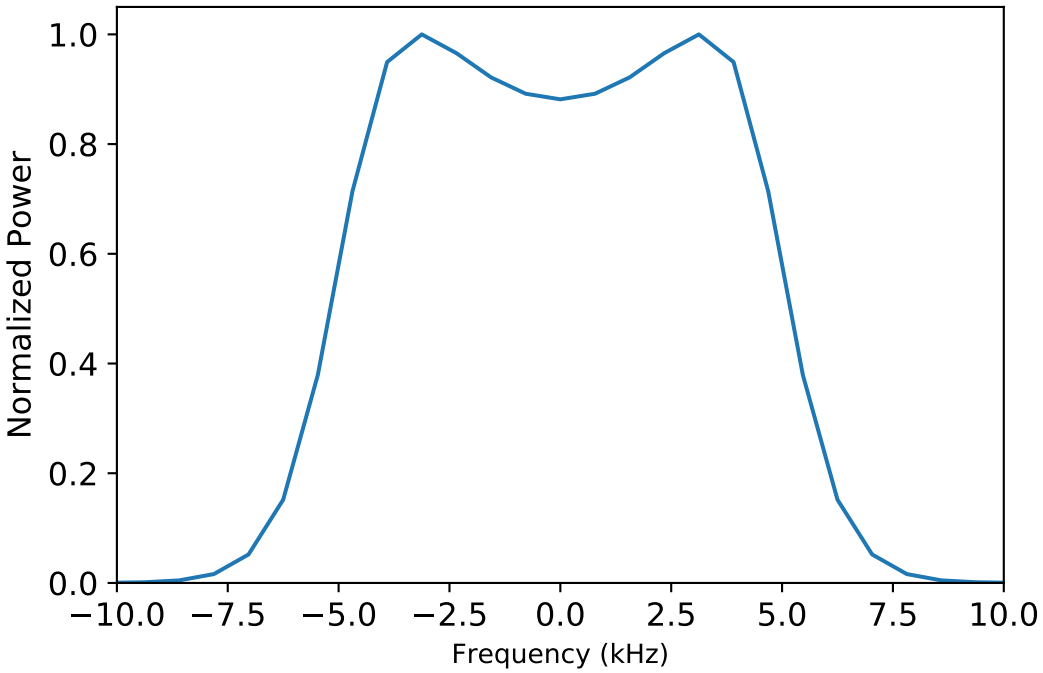

Fig. 2.1: An example of an ISR spectrum. This is from a model and the vertical axis shows normalized power and the horizontal axis the frequency. The center frequency is 440.2 MHz. This example uses an ion and electron temperatures of 1200 K. It assumes that the only ion is atomic oxygen and the electron density is 1.0×10^{11} m^{-3}.

the ion temperature and electron temperature can be determined. Another way to break the degeneracy is to assume that the ion temperature is equal to the electron temperature. This is often true at night in the F-region and with this assumption the region where the major ion transitions from O^+ to H^+ can be determined.

In this dissertation I use three ISRs to measure these plasma parameters: the Jicamarca ISR, the Arecibo ISR, and the Millstone Hill ISR. The Jicamarca ISR is the main radar array at the Jicamarca Radio Observatory (11.95° S, 76.87° W, 0.3° S magnetic latitude) in Peru. This array consists of 18,432 dipole elements that is about 300 m x 300 m and operates at 50 MHz (*Ochs*, 1960). The Arecibo ISR is located at the Arecibo Observatory (18.34° N, 66.75° W, 26.2° N magnetic latitude)

in Puerto Rico. This radar is a 305 m dish and operates at 430 MHz (*Gordon*, 1964). There are two Millstone Hill ISRs. One is a 46 m steerable antenna and the other is a 68 m fixed zenith pointing antenna (*Zhang and Holt*, 2004) that both operate at 440 MHz. These are located at the MIT Haystack Observatory (42.62° N, 71.19° W, 50.77° N magnetic latitude) in Massachusetts.

The Jicamarca ISR has the advantage of being located at the magnetic equator which allows for unique observing conditions. These conditions also lead to two different ISR modes: perpendicular and oblique. In the perpendicular mode the beam is pointed such that it is perpendicular to the magnetic field. This creates a sharply peaked spectrum that allows the line of sight velocities to be easily determined. In the oblique mode it is pointed oblique to the magnetic field to get a more standard ISR spectrum to determine the other ISR parameters. The beam positioning must be done manually so it is not simple to switch between the two modes.

At Arecibo the pointing is done by moving the receiver above the dish. This allows the antenna to point up to about 18° from zenith at all azimuth angles. The dip angle at Arecibo means that these are all oblique observations. A difference between Jicamarca and Arecibo is that the power and sensitivity at Arecibo allows for accurate line of sight velocity measurements even though observations are oblique to the magnetic field.

The steerable antenna at Millstone Hill can point in many more directions than the other two radars. The limits on elevation angle are mostly due the presence of other buildings at the facility and the pointing can be as low as about 5° elevation angle and can point in all azimuth directions.

As mentioned, there are slightly different ways to analyze ISR that can impact the determination of ionospheric parameters. At night, these different techniques can have a significant impact on the results. Many ISR stations publish their data online

through the Madrigal Database (http://madrigal3.haystack.mit.edu/). The results published there are the temperatures, densities, and velocities determined using the facilities fitting technique. The error is also provided but is not always indicative of the accuracy of the fit because sometimes the fit can give a non-physical result.

At night, it is expected that the ion and electron temperatures at low-latitudes and mid-latitudes are approximately equal. Additionally, since the electrons have a lower mass compared to the ions and because during the day the electron temperature is greater than the ion temperature, the ion temperature should not be significantly greater than the electron temperature at night. In our analysis we found cases, from both the Arecibo ISR and the Millstone ISR, where a large increase in ion temperature occurred at the same time as a large drop in electron temperature such that the ion temperature could be over 100 K greater than the electron temperature. This major difference in the two temperatures, with the electron temperature being lower, indicated that this was an error due to the fitting. At first it seemed that the increase in ion temperature was an interesting geophysical feature but it turned out to be an inaccurate fit. This increase in ion temperature always accompanied a large drop in electron density. This caused the signal to be too low for an accurate fit. We found cases like this in the Madrigal Database and in the data product provided to us directly from the facilities.

For the Arecibo ISR data we ignored this part of the data and for the Millstone Hill ISR the fits were redone so that if the electron temperature was less than the ion temperature then they were forced to be equal. This was more of a problem at the Millstone Hill observatory because of the smaller antenna, and thus smaller gain, compared with Arecibo antenna. At the Jicamarca Observatory, the standard fitting procedure is to force the ion and electron temperature to be equal so that this problem is not encountered.

In addition to being used for ISR these radar systems can be used for coherent scatter. Coherent scatter happens when there are density irregularities in the plasma. If the scale size of these irregularities is equal to half the wavelength of the radar then the incident wave will be scattered and can be detected by the radar receiver, this is similar to Bragg scattering in crystals. This technique uses much less power than ISR so it can be used more frequently and with relatively smaller antennae. Coherent scatter is important at low-latitude regions where it can be used to detect field-aligned irregularities associated with ESF. In particular, we use the main array at Jicamarca in the Jicamarca Unattended Long Term Investigations of the Ionosphere and Atmosphere (JULIA) mode to detect irregularities associated with equatorial spread-F. These are irregularities with scale sizes of 3 m since the radar operates at 50 MHz.

2.1.2 Optical instruments

(A) All-Sky Imagers

A large part of this dissertation is focused on observations of the upper atmosphere using all-sky imagers (ASI). An ASI is a camera that uses a wide-angle lens with a 180° field of view (FOV), also known as a fisheye lens, to capture an image of the entire sky at once. For aeronomy, these ASIs are used to measure airglow emission from various altitudes in the upper atmosphere. The Imaging Science Team at Boston University operates 13 ASIs throughout the world. Figure 2.2 shows the locations and fields of view of these imagers.

For the work presented here I focus on three ASIs in South America. One ASI is located in El Leoncito, Argentina (31.8° S, 69.3° W, 19.7° S magnetic latitude) and has been operating there since 1999. In March 2014 I helped install one of the other ASIs at Jicamarca Radio Observatory in Peru. The third ASI was installed in October 2014 in Villa de Leyva, Colombia (5.6° N, 73.52° W, 16.2° N magnetic

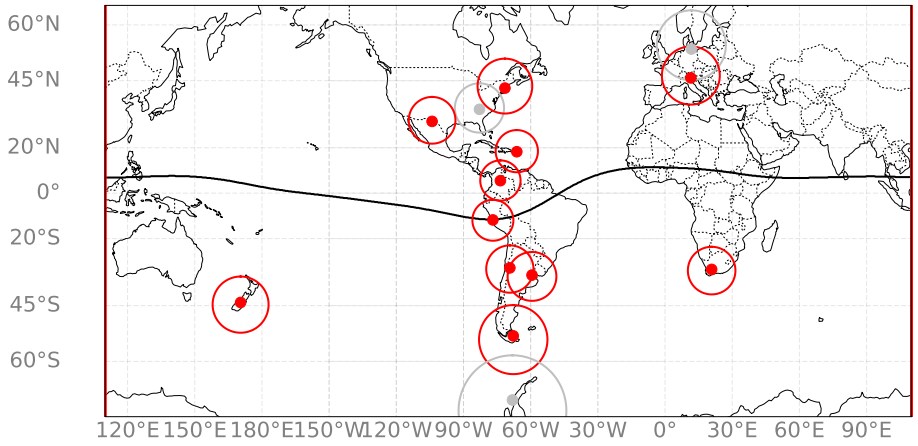

Fig. 2.2: A map showing the locations of the BU ASIs around the world. The circles show an 80° field of view at 300 km. The dots are the locations of the imagers. The color red shows imagers operated totally by BU and the gray circles are partially operated by other groups.

latitude). The Villa de Leyva ASI is located close to the magnetic conjugate point of El Leoncito ASI and the field of view of the ASI contains the conjugate point. Figure 2.3 shows a map of South America with the location of these three ASIs with their conjugate locations and fields of view.

These three ASIs, and the others operated by BU, have narrow band interference filters selected for emissions from the ionosphere and mesosphere. Each ASI has a filter wheel that cycles through each of the filters such that it there is about 9 minutes between exposures of the same filter. The El Leoncito ASI has the following filters: 5577 Å, 5893 Å, 6950 Å, 7774 Å and 6300 Å. The Jicamarca ASI takes images at four wavelengths: 5577 Å, 6950 Å, 7774 Å and 6300 Å. Each filter is used to observe different processes in the upper atmosphere that produce airglow emissions. Additionally there is a filter at 6050 Å that is used for calibration purposes. The Villa de Leyva ASI has the following filters: 5577 Å, 6950 Å, 7774 Å and 6300 Å.

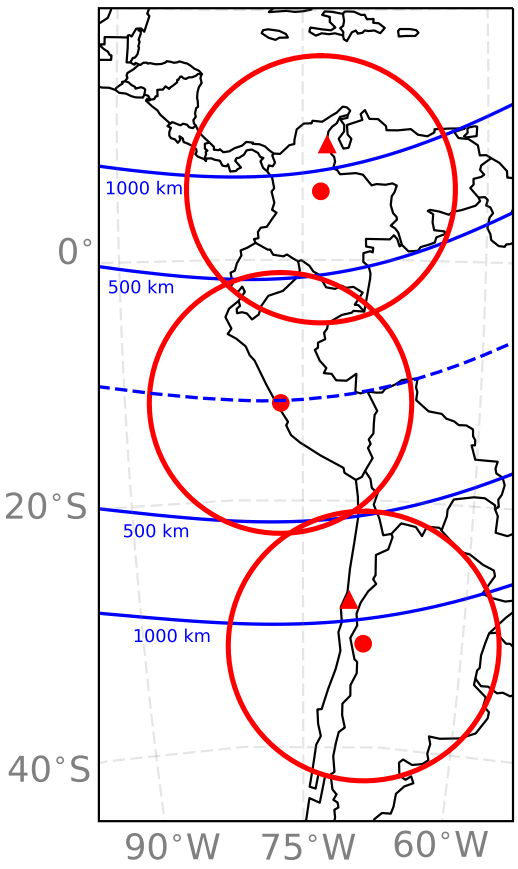

Fig. 2.3: A map of western South America showing the location of the Villa de Leyva (top), Jicamarca (middle), and El Leoncito (bottom) ASIs as red dots. The red circles around the dots are the fields of view for an airglow layer at 300 km and a zenith angle of 80°. The red triangle in the Villa de Leyva field of view is the conjugate location of the El Leoncito ASI. The red triangle in the El Leoncito field of view is the conjugate location of the Villa de Leyva ASI. The blue dotted line is the magnetic equator and the solid blue lines are lines of constant magnetic apex altitude.

The 6300 Å filter has a full width at half maximum of about 10 Å. The optical assembly limits the angle of incidence on the filter to less than about 4° to the normal. The filter transparency varies by no more than 10% within this angle and the greatest deviation is only from the edge of the images at 90° viewing angles (*Baumgardner*, 1993). Production of 6300 Å is multi-step process involving oxygen. The first step

is charge exchange between molecular oxygen and ionized atomic oxygen (Equation 2.1). When the ionized molecular oxygen recombines it dissociates and creates an excited neutral atomic oxygen in the ^1D state (Equation 2.2). The excited oxygen can de-excite by quenching with neutrals or by the spontaneous emission of a 6300 Å photon (Equation 2.3).

$$O_2 + O^+ \rightarrow O_2^+ + O \tag{2.1}$$

$$O_2^+ + e^- \rightarrow O(^1D) + O(^3P) \tag{2.2}$$

$$O(^1D) \rightarrow O(^3P) + h\nu(6300\text{Å}) \tag{2.3}$$

The conditions for this to occur are met in the bottomside of the F region of the ionosphere. Emission is limited to a small altitude range (about 50 km) that is typically centered near 250 km but varies and can be as high as 400 km early in the night. The emission is dependent of the electron density and the neutral density. For a more detailed analysis of 6300 Å emission see *Colerico et al.* (2006). 7774 Å emission is caused by the radiative recombination of O^+ and is directly proportional to total electron content (2.4).

$$O^+ + e^- \rightarrow O + h\nu(7774\text{Å}) \tag{2.4}$$

The majority of 7774 Å emission is typically in the 300-400 km range.

The dependence on electron density is what makes the airglow images useful. When analyzing the images we make the reasonable assumption that the background neutral density does not vary a lot throughout the field of view or during the course of night. This means that that variations in emission throughout the image are due

to variations in electron density. Regions of low density will appear darker than the rest of the image and the brighter regions are due to higher electron density.

To analyze the data from the ASIs we must unwarp the images to get accurate sizes and shapes for the features we are observing. To unwarp an image we assume an emission height and use zenith angles between 0° to 80° to determine the longitude and latitude of each pixel. We then overlay a geographical map with grid lines. We subtract the background image from the 6300 Å image, divide by the exposure time, and multiply by a constant factor to determine the emission in rayleighs (*Baumgardner et al.*, 2008). We remove the stars from the images using an algorithm that replaces brighter pixels with the median of the surrounding pixels. The plasma depletions in the raw images are curved and extend from north to south, covering the entire field of view. In the unwarped images they are visible as mostly straight bands that are aligned in the N-S direction. Figure 2.4 shows a raw image on the left and a calibrated unwarped image on the right from the Jicamarca ASI. The features visible in these images are the dark bands covering the full meridional extent of the images. These are plasma depletions associated with ESF.

(B) Fabry-Perot interferometer

Another optical instrument that we use is a Fabry-Perot interferometer (FPI). FPIs are used to measure neutral winds and temperatures in the upper atmosphere. FPIs can operate at multiple wavelengths but for this dissertation FPIs with a wavelength filter of 6300 Å are the focus. This is the same wavelength as the majority of ASI observations. Although the intensity of 6300 Å is proportional to electron density the output from an FPI provides diagnostics of the neutral atmosphere. This is because the origin of the excited oxygen atom is O_2. The FPI creates an interference pattern from the 6300 Å emission using two plates placed closely together.

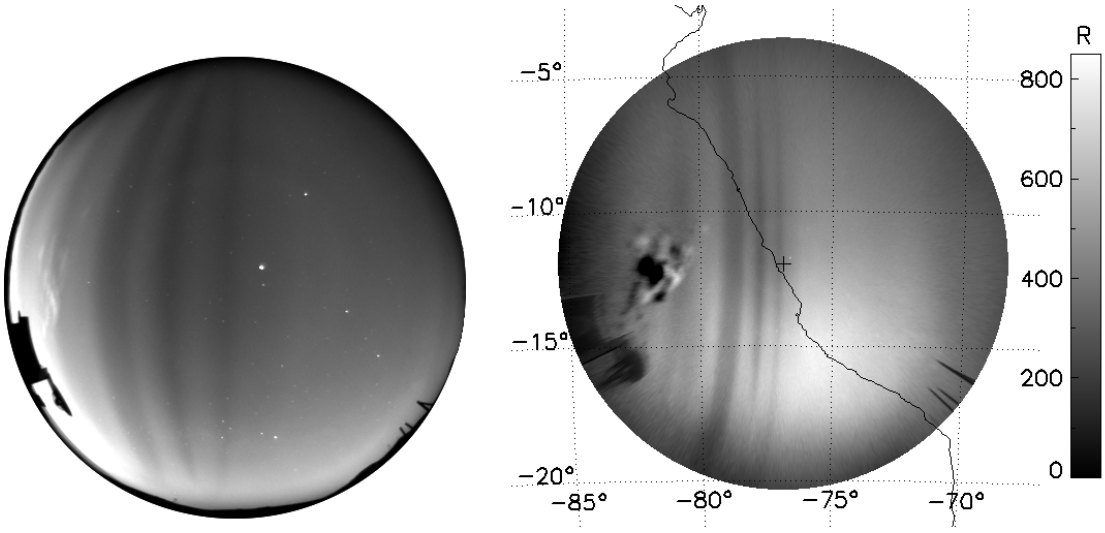

Fig. 2.4: (left) A raw image at 05:18 UT on 3 Apr 2014 from the Jicamarca ASI. The exposure time is 120 s and the image was obtained using a 6300 Å filter. Clouds are visible on the left edge of the image (right). The unwarped image. The top of the image is north and the left of the image is west. The western coast of South America is seen as a black line and the location of the ASI is marked with a small black cross. The dotted lines are geographic latitudes and longitudes. Latitude and longitude is determined for each pixel and the image is transferred to a map projection. The gray scale shows the brightness in rayleighs. Clouds low on the horizon are now more prominent in the unwarped image. They also contain dark areas due to background subtraction.

The interference pattern is a set of concentric rings. The interference pattern is used for analysis of the neutral atmosphere. The Doppler shift of the pattern provides a measurement for the line of sight velocity and is used to determine the bulk motion of neutral atmosphere. In most cases the 3-D velocity vectors are of interest. In order to do this, the FPI points at 45° from zenith in each of the four cardinal directions and also points at zenith. With the assumption that the winds do not vary between the different measurements positions and times, a vector wind measurement can be made. A temperature measurement is made using the width of the rings.

2.1.3 Additional instruments

In addition to the radar and optical instruments there are other instruments that are important to this study. These include ionosondes and ground-based global positioning system (GPS) receivers.

Ionosondes are instruments used to measure the density of the bottom side of the ionosphere. An ionosonde is a radio wave transmitter and receiver that sweeps through frequencies typically from 1 to 15 MHz. The underlying principle of these instruments is that the refractive index of the ionosphere is dependent of the electron density. For the simple case with no collisions and no magnetic field then the refractive index is given by

$$n^2 = 1 - \frac{\omega_e^2}{\omega^2} \tag{2.5}$$

where ω is the frequency of the incident wave and ω_e^2 is the plasma frequency. ω_e^2 is given by

$$\omega_e^2 = \frac{n_e e^2}{\epsilon_0 m} \tag{2.6}$$

where n_e is the electron density, e is the charge of the electron, ϵ_0 is the permitivity of free space, and m is the mass of the ion species. When the refractive index is zero or imaginary the incident wave can no longer propagate and is reflected. This happens when the incident frequency is greater than or equal to the plasma frequency. The ionosonde can determine the altitude of constant electron densities by sweeping through the frequencies and measuring the time delay. Since the refractive index changes with altitude due to the presence of electrons some analysis must be done to get the accurate altitude from the time delay. An example of an ionosonde output, know as an ionogram, is shown in Figure 2.5.

Global Positioning system (GPS) receivers are used to measure the total electron content (TEC) between the receiver and the GPS satellite. GPS satellites broadcast

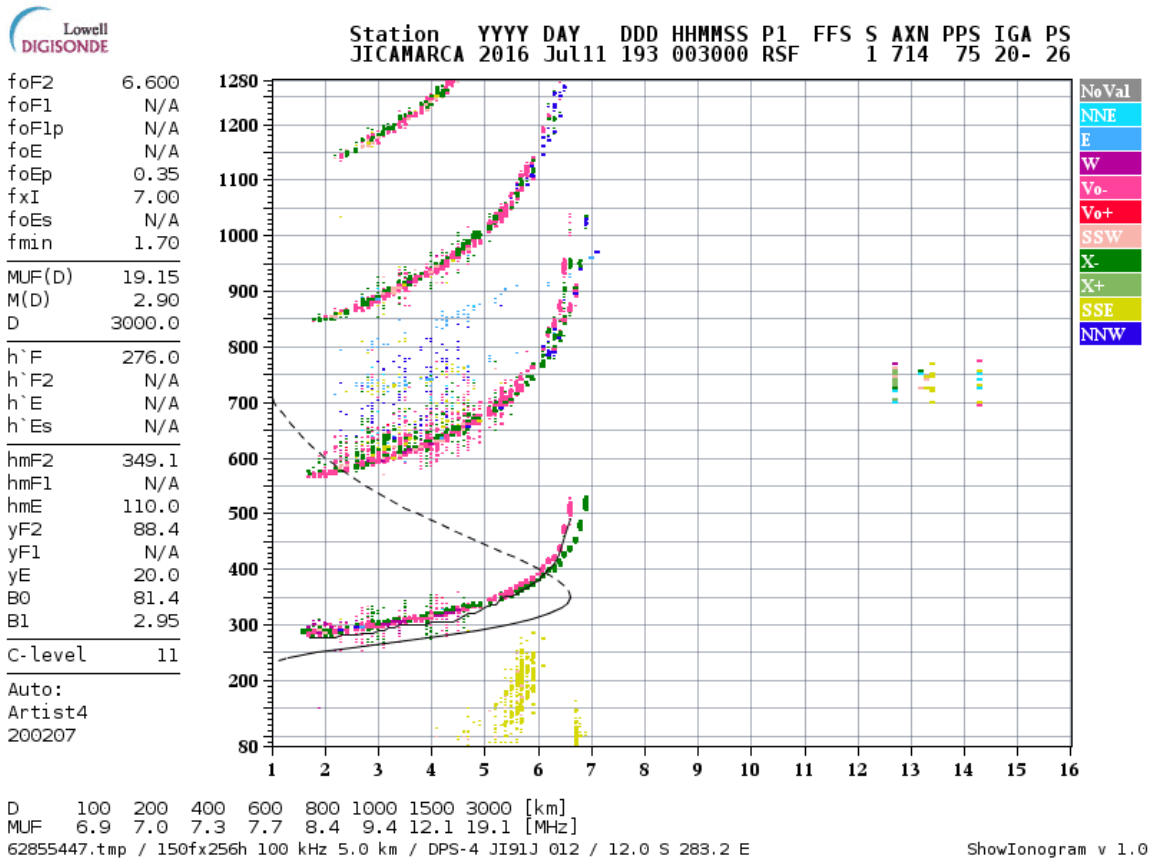

Fig. 2.5: An example of an ionogram at the Jicamarca Radio observatory. The vertical axis shows altitude in km and the horizontal axis is frequency in MHz. The different colors correspond to different directions and different wave modes. There are multiple traces due to multiple reflections from the ground and ionosphere. The black line is the fit for the actual ionosphere profile. Additionally, derived parameters are shown in the column on the left. From the Lowell Digisonde International database.

at two frequencies, 1.57542 GHz and 1.2276 GHZ. Both of these are greater than the plasma frequency of the ionosphere so they are able to pass through but since the index of diffraction is still affected by the electron content of the ionosphere there is a phase delay in the signal. GPS satellites use two frequencies to correct for this phase delay and thus we can use the two frequencies to determine the total number of electrons between the satellite and the receiver, which is known as TEC. Variations

in the phase and amplitude of the signals can also be used to identify small scale irregularities in the ionosphere.

2.2 Models

In this work various models are compared with the data and are used to provide context and otherwise unavailable information about the measurements. This section describes the models that are used.

An accurate calculation of 6300 Å airglow emission altitude requires a model that uses ionosphere and thermosphere parameters to determine the emission as a function of altitude. The emission is calculated using the BU Airglow model (*Semeter et al.*, 1996). The model uses height profiles of electron density (n_e), ion temperature, and electron temperature as ionosphere inputs. For thermosphere inputs, the model uses height profiles of neutral temperature along with density profiles of atomic oxygen (O), molecular oxygen (O_2), and molecular nitrogen (N_2). The basic equation for this model is shown below.

$$\eta_{6300} = \frac{A_{6300} f(^1D) k_O [O_2] n_e}{A_{^1D} + \text{quench}} \tag{2.7}$$

where

$$\text{quench} = (qN_2)[N_2] + (qO_2)[O_2] + (qO)[O] + (qn_e)n_e \tag{2.8}$$

A_{6300} is the Einstein transition coefficient for 6300 Å emission, $f(^1D)$ is the quantum yield of $O(^1D)$ for the dissociative recombination of O_2^+ (Equation 2.2), k_O is the ion temperature dependent reaction rate for oxygen charge exchange (Equation 2.1), $A_{^1D}$ is the Einstein transition coefficient for photon emission, and the q terms are the temperature dependent quenching coefficients. Equation 2.7 models airglow that is a result of Equations 2.1, 2.2, and 2.3. It does not model airglow that is a result of other processes such as stable auroral red arcs that are a result of thermal excitation

of atomic oxygen. Ideally, the ionosphere and thermosphere parameters would be measured locally but this often not the case, especially for the neutral parameters. As a result this model relies on other models. The Naval Research Laboratory Mass Spectrometer and Incoherent Scatter (NRL-MSISE-00) model (*Picone et al.*, 2002) is used for the thermospheric inputs. This is an empirical atmospheric model that extends from the ground to the exobase. The International Reference Ionosphere (IRI-16) model (*Bilitza et al.*, 2017) is used for ionosphere inputs. IRI-16 is an empirical ionosphere model.

In addition to these models, a few other empirical models are used in this work. The Horizontal Wind Model (HWM-14) (*Drob et al.*, 2015), an empirical thermospheric wind model, is used to inform airglow observations. The International Geomagnetic Reference Field (*Thébault et al.*, 2015) is model that describes the large-scale magnetic field of the Earth. It is a collaboration between magnetic field modelers and magnetic field data collectors. This is used when comparing conjugate magnetic airglow observations.

In addition to empirical models, a physics based model is used to compare with observations of the MTM. The model discussed in this dissertation is the Whole Atmosphere Model (WAM) (*Akmaev et al.*, 2008). This is a general circulation model based on the US National Weather Service's Global Forecast System. It has been extended upward to cover from the ground up to 600 km. The goal of this model is to understand the generation, propagation, and nonlinear interactions of atmospheric tides and planetary waves.

Chapter 3

Midnight Temperature Maximum

3.1 Introduction

The midnight temperature maximum (MTM) is an increase in neutral temperature around local midnight in the thermosphere. The MTM is a common feature that has been historically observed near the geographic equator (*Herrero and Spencer*, 1982). The goal of this chapter is to increase the knowledge of the MTM by measuring its altitude extent and variation, seasonal variation, and its latitudinal extent and morphology.

Although the MTM is a neutral phenomena, the absence of plasma production by EUV radiation during the night allows the electron and ion temperatures to relax to the neutral temperature in the thermosphere. Thus variations in the nighttime ion and electron temperatures (T_i and T_e, respectively), determined by the incoherent scatter radar (ISR) technique, should reflect variations in the neutral temperature T_n. This has been observed before using the ISR at Jicamarca (*Bamgboye and McClure*, 1982, e.g.,) and at Arecibo (*Harper*, 1973, e.g.,). The Arecibo Observatory has one of the largest ISRs in the world and has been collecting data since the 1960s. Using the Arecibo ISR, *Behnke and Harper* (1973) showed that during an MTM event nighttime neutral winds, being typically equatorward, are first seen to abate and then often turn poleward by 02:00 LT, leading to an observed drop in the height of the F layer near midnight. During a 5-day case study in March 1971, *Harper* (1973) observed a $\sim$40 K increase in T_i at 350 km near midnight. They attributed this increase to the

adiabatic heating of the neutral gas. They also inferred the meridional component of the neutral wind. Additionally, there was a strong decrease in the equatorward wind near midnight and a weak reversal near 02:00–03:00 LT. This reversal was associated with the observed ionospheric descent, the so-called midnight midnight collapse.

Even though several studies have shown the midnight collapse at Arecibo (*Nelson and Cogger*, 1971; *Crary and Forbes*, 1986; *Gong et al.*, 2012), there were no statistical studies of the MTM using ISR observations. ISR measurements of nighttime enhancements in T_i (or T_e) should fill the gap existing in the seasonal characterization of the MTM developed from FPI measurements. Besides, ISR determined T_i can indicate the range of altitudes over which the enhancement occurs. Altitude information may provide evidence on the source of the MTM. In Section 3.2 I measure the characteristics of the MTM (time and amplitude) at Arecibo and investigate the seasonal dependence of these characteristics. This work has also been summarized in *Martinis et al.* (2013).

Although it is observed regularly, the generation mechanism for the MTM is not fully understood. Some modeling efforts that attempted to reproduce the MTM were unsuccessful (*Colerico et al.*, 2006; *Meriwether et al.*, 2008) until recently, when *Akmaev et al.* (2009) was able to create a realistic MTM with the Whole Atmosphere Model (WAM). WAM has been developed under the Integrated Dynamics in the Earth's Atmosphere (IDEA) project to study and eventually forecast dynamical links between the lower atmosphere and the upper atmosphere and ionosphere. It is based on the US National Weather Service's operational Global Forecast System model, extended upward to cover the atmosphere from the ground to the exosphere at about 600 km (*Akmaev*, 2011). These modeling studies have shown that the MTM feature may be traced down to the lower thermosphere, where it is manifested primarily in the form of an upward propagating terdiurnal tidal wave, as discussed in Section 1.4.1.

In *Akmaev et al.* (2009) it is postulated that the success of WAM over other models is related to the inclusion of other tidal harmonics interacting with the terdiurnal wave, the vertical resolution, and less imposed numerical dissipation. These atmospheric waves are influenced by the solar cycle, but no connection between the MTM and solar cycle has been shown before.

In Section 3.3 I combine measurements from the Arecibo radar, the Millstone Hill radar, and an FPI to investigate the timing and location of the MTM at multiple locations. The data presented here provide new measurements of the MTM at mid-latitudes, extending the coverage presented in Section 3.2. This work was published in *Hickey et al.* (2014). There have been relatively few measurements of the MTM at mid-latitudes. At these latitudes only MTM effects determined by 630.0 nm airglow emissions at altitudes of ∼250km have been observed (*Colerico et al.*, 2006). These measurements help to constrain models reproducing the MTM and its altitude variations, something not fully explored due to the lack of reliable ground-based MTM detection at different heights and latitudes. The ionospheric measurements presented here, using the Millstone Hill ISR, represent a new application of a well-established technique to study atmospheric parameters.

In Section 3.4 I use the Jicamarca radar, an FPI, and an ASI to measure the timing and extent of the MTM. This work has been published in *Hickey et al.* (2018). The observations are from the Jicamarca observatory at the magnetic equator and an ASI in Argentina. In a previous study on the MTM at Jicamarca, *Bamgboye and McClure* (1982) measured nighttime electron temperatures at 300 km with the incoherent scatter radar. Sixty of 127 nights in 1967–1969 showed increases in T_e of 100–150 K near local midnight. A seasonal dependence of the local time of occurrence, defined as the time of peak amplitude, was also observed. The local time of the maximum T_e occurred later during June–July solstice, i.e., local winter. ASIs mea-

sure the optical signature of the MTM, known as a brightness wave (BW). *Colerico et al.* (1996) reported the first BW detection with an ASI. A pressure bulge created by the MTM results in a reversal of meridional neutral wind and this poleward wind drags the plasma with it (*Colerico et al.*, 1996; *Akmaev et al.*, 2010). Away from the magnetic equator the plasma moves downward along magnetic field lines as it is dragged by neutral species. As plasma moves down increased 6300 Å emission moving poleward in the field of view of the ASI is observed (i.e., a brightness wave). The brightness wave has been observed away from the magnetic equator at various latitudes and longitudes (e.g., *Colerico et al.*, 1996; *Fesen*, 1996; *Martinis et al.*, 2006).

The three sections in this chapter provide new observations of the MTM in order to better understand its temporal and spatial characteristics. I present new observations at various altitudes to look at its variation with altitude and investigate the seasonal variation of the MTM and measure the impact of solar activity. For the first time, I detected and measured the MTM in ion temperatures at mid-latitudes and use these measurements explore the latitudinal extent of the MTM. The measurements presented in this chapter also provide a better understanding of the spatial morphology of the MTM. All these observations contribute to a better understanding of the MTM that allows us to determine if the generation mechanism of the MTM that exists in the WAM model is accurate. Understanding this generation mechanism is key to determining one aspect of coupling between the lower atmosphere and the upper atmosphere.

3.2 The MTM at Arecibo

This section shows results obtained using ISR data from Arecibo and addresses some key issues related to MTM characterization, namely, local time of occurrence, amplitude, altitude, and solar activity dependence.

3.2.1 Data and Fitting Method

Temperature data between 1967 and 2010 were taken from the Madrigal and Arecibo databases. The total number of analyzed days was 491, of which 283 had nighttime data suitable for this work. The study originally focused on data at a height close to 300 km that, in general, is below the ionospheric peak during the post-sunset period. Most of the spectra from this location were unreliable at this height due to low electron density or the large electron density height gradient that exists below the peak. Due to this limitation in the technique, only approximately 25% of the nighttime data at 300 km were usable and the study was expanded to include heights close to 330 km and 367 km. At these heights the electron density is generally larger and has no strong altitude gradient, so the number of reliable determinations of T_i was much greater.

Figure 3.1 shows the number of cases observed by month during the entire period. At 300 km only 82 cases were included while at 367 km (and 330 km) the total number increased to 229. MTM effects were observed on 66 of 82 nights at 300 km. Figure 3.1 shows that there is no preferred month for the occurrence of MTM cases. Several nights showed the occurrence of double temperature enhancements, one close to midnight and the other much earlier (pre-MTM) or much later (post-MTM). Pre-MTM features have been observed using FPIs by *Faivre et al.* (2006) at Arequipa (161S, 71.51W) and ASIs by *Colerico et al.* (2006), at Arequipa and El Leoncito (31.81S, 69.31W), and modeled by *Akmaev et al.* (2009), who showed

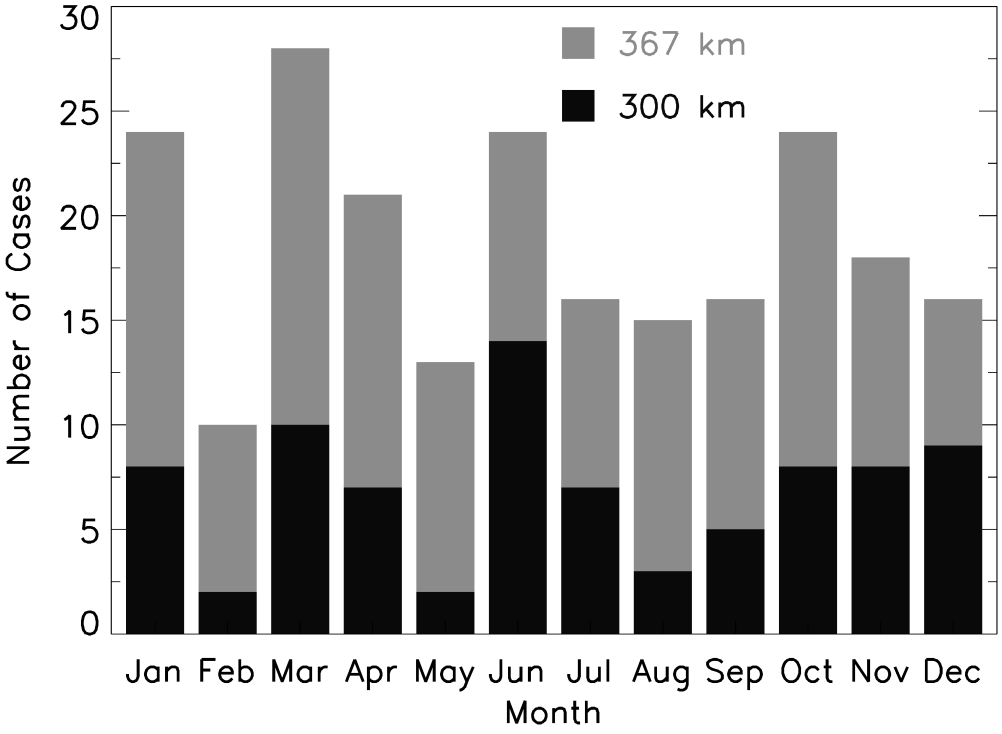

Fig. 3.1: Number of cases showing MTM effects at 300 km(black) and 367 km(gray). No clear seasonal dependence is observed. The smaller number of cases at 300 km is due to the limitations in the technique to determine temperatures when small electron density is measured and/or large height electron density gradients occur.

the presence of a secondary maximum between 2000 and 2100 LT. There was no clear seasonal trend in the occurrence of these double cases. These early-time T_i increases were not included in our MTM statistics. Some of the late or post-MTM effects occurred very close to local sunrise at these heights (∼04:30 LT in summer and ∼06:30 LT in winter) while others occurred closer in time to conjugate hemisphere sunrise, around ∼03:30 LT (*Carlson*, 1966; *Chao et al.*, 2003). These late-time T_i enhancements, occurring after ∼03:30 LT, are not related to MTM effects, and are not included in our MTM statistics.

One of the advantages of using ISR measurements to study the MTM is the capability of studying characteristics at different heights, something not possible with FPI or all-sky imaging diagnostics, which provide height-integrated values centered at ∼250 km (300 km) for low (high) solar activity. T_i enhancements were observed to occur as low as 283 km and as high as 467 km in the radar data.

To characterize the features of the MTM, we have fit each day's data with a mathematical function that includes a constant and harmonics representing different tidal modes in the upper atmosphere (the diurnal, semidiurnal, and terdiurnal waves). To account for possible differences in starting and ending temperature over a 24-h period, we have also included a slope term:

$$\begin{aligned} f_0(t) = p_1 + p_2(t-\bar{t}) + p_3 \sin\left(\frac{2\pi t}{24}\right) + p_4 \cos\left(\frac{2\pi t}{24}\right) \\ + p_5 \sin\left(\frac{2\pi t}{12}\right) + p_6 \cos\left(\frac{2\pi t}{12}\right) \\ + p_7 \sin\left(\frac{2\pi t}{8}\right) + p_8 \cos\left(\frac{2\pi t}{8}\right) \end{aligned} \tag{3.1}$$

Here p1 and p2 represent the constant and slope terms, respectively, and the remaining p's are the amplitudes of the harmonic terms used in the fitting. This fitting function represents very well the behavior of the temperature for most of a day, but it does not show an MTM feature. Our assumption is that the MTM represents an amplification of the terdiurnal component. This is included in our fitting function by multiplying the 8-h terms by a Gaussian time window of adjustable amplitude, location, and width. Thus the final function f(t) used to characterize MTM features is:

$$\begin{aligned} f_0(t) = p_1 + p_2(t-\bar{t}) + p_3 \sin\left(\frac{2\pi t}{24}\right) + p_4 \cos\left(\frac{2\pi t}{24}\right) \\ + p_5 \sin\left(\frac{2\pi t}{12}\right) + p_6 \cos\left(\frac{2\pi t}{12}\right) \\ + \left[p_7 \sin\left(\frac{2\pi t}{8}\right) + p_8 \cos\left(\frac{2\pi t}{8}\right)\right] \left[1 + p_9 e^{-(t-p_{10}/p_{11})^2}\right] \end{aligned} \tag{3.2}$$

The p9 coefficient represents the amplitude of the Gaussian and is used to quantify the amplitude of the MTM. The p10 coefficient locates the center of the Gaussian, which correlates with the local time peak of the MTM. Finally, the p11 coefficient represents the width of the fitted Gaussian, related to the duration of the MTM. The Gaussian extends over all time, but was found always to be narrow so as to affect only the 8-h wave cycle near midnight.

Equation 3.2 is non-linear and one must iterate to obtain a proper fit. The first step was to fit the data with the function described in Equation 3.1 (i.e., just constant, slope and sinusoidal terms). These eight p parameters were used as starting values in the ensuing nonlinear fit of Equation 3.2. A least squares fit of Equation 3.2 to the data was made and the entire set of 11 p parameters was determined. Adjustments were made to the fitting procedure when data availability did not cover an entire 24 h period, or significant data gaps existed during the nighttime period; specifically, if the data covered only the nighttime region of interest, a simple Gaussian and a straight line were used to fit the data, similar to the procedure applied to nighttime FPI measurements to extract MTM characteristics (*Meriwether et al.*, 2008).

Because the center of the Gaussian is not constrained to occur at the time of the peak of the nighttime 8-h sinusoid, we have chosen to characterize the MTM as illustrated in Figure 3.2 for 16–17 November, 1990 at 293 km. This figure shows data from more than 24 h, allowing us to compute all the parameters in Equation 3.1 and 3.2. Here we show T_i data averaged to 15-min resolution fitted by Equation 3.2 (blue thick curve with a bump around 0000 LT). The red thin curve is the result of fitting Equation 3.1, i.e., without the Gaussian window. The time of the peak smooth-curve temperature at night is shown by the green vertical line. The turquoise straight line connects the locations of the minima to the left and right of this peak. The amplitude

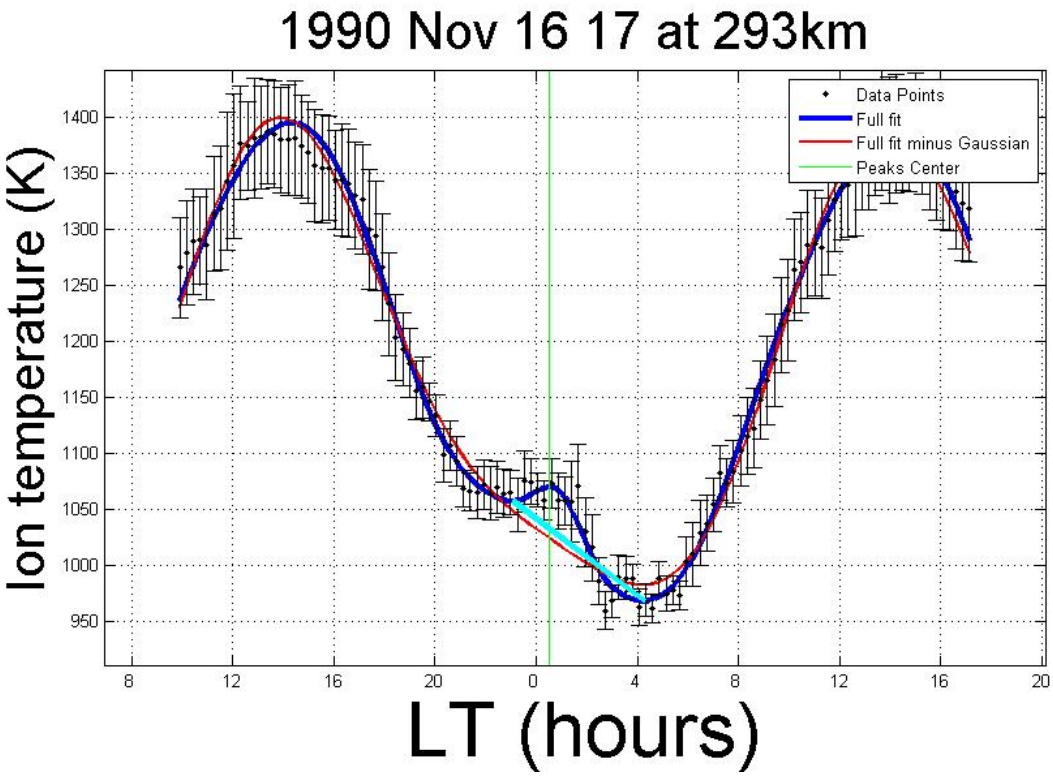

Fig. 3.2: Typical example of nighttime MTM observed in the data. The blue thick curve is the full fitted function f, and the red thin curve is the fitted function without the Gaussian amplification. The turquoise straight line is used to compute the temperature enhancement. The vertical green line around 0000LT indicates the peak center

of the MTM is defined as the distance along the green line between its intersections with the blue and turquoise lines.

3.2.2 Seasonal Variation of the MTM

We initially analyzed ISR data near 300 km altitude, a challenging task due to the low electron density and sharp gradients during the time of interest (post-sunset). The analysis began at 300 km because it is close to previous FPI observations at 250 km. The criterion to select the usable nights was to look for those cases when T_i was equal to T_e, a condition necessary to identify reliable data. Data at 330 km and 367 km were also analyzed, and the number of cases available for a proper determination

of ion temperatures increased from 82 to 229. The results, summarized in Figure 3.1, indicate that the MTM is a recurrent phenomenon and, as such, it provides evidence of the importance of coupling with the lower atmosphere. These results can be compared with the study of the 'midnight collapse' at Arecibo by *Nelson and Cogger* (1971) who found changes in hmax, the height of the peak electron density, of 50–100 km beginning near midnight in 85% of the 130 cases analyzed. Our current understanding of the midnight collapse can be directly related to the occurrence of the MTM; specifically, it is caused by poleward winds driven by the MTM pressure bulge. A study by *Gong et al.* (2012) suggests that electric field and ambipolar diffusion also might play an important role in the occurrence of the midnight collapse.

The monthly behavior of the local time of MTM occurrence, defined as the time of peak effect as indicated by the green line in Figure 3.2, at 300 km is shown in Figure 3.4. Asterisks represent monthly means. The local time of occurrence spanned a wide time range, between 22:00 and 03:00 LT. This limited sample of data shows that earlier average local time of occurrence between 00:00 and 00:30 LT is observed during the month of June, with October, November and January months also showing a relatively early local time of occurrence.

Figure 3.5 shows the MTM amplitude, ranging from ∼20 to ∼150 K, with smaller average values found during the November–March period. A peak in monthly-averaged amplitude is found during local summer months, with an average of ∼75 K. The average for the November–March period is ∼50 K. Ground-based results using FPI measurements from Arequipa have shown peak amplitudes during equinox, although southern hemisphere summer values were not available due to cloudiness at the site (*Faivre et al.*, 2006). Using an FPI at Cajazeiras (6.891°S, 38.561°W), *Meriwether et al.* (2011) showed peak MTM amplitudes during September equinox.

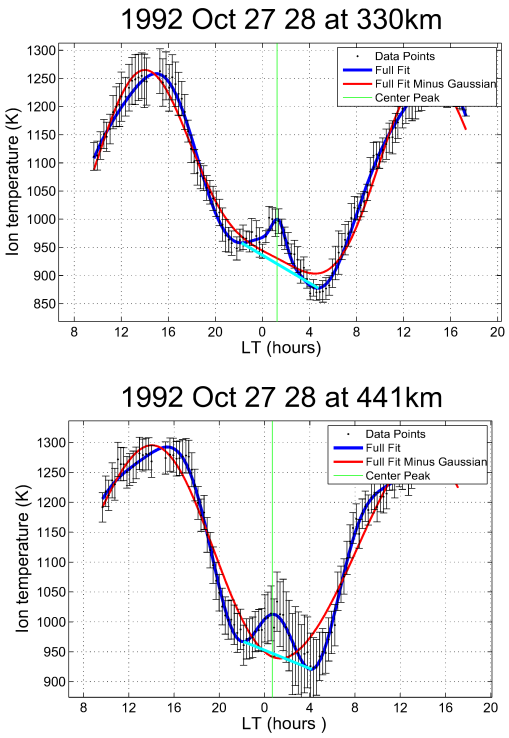

Fig. 3.3: Example of altitude variation of MTM characteristics. Data were binned in 15 min intervals. The data and fitted curves show an MTM extending up to 441 km.

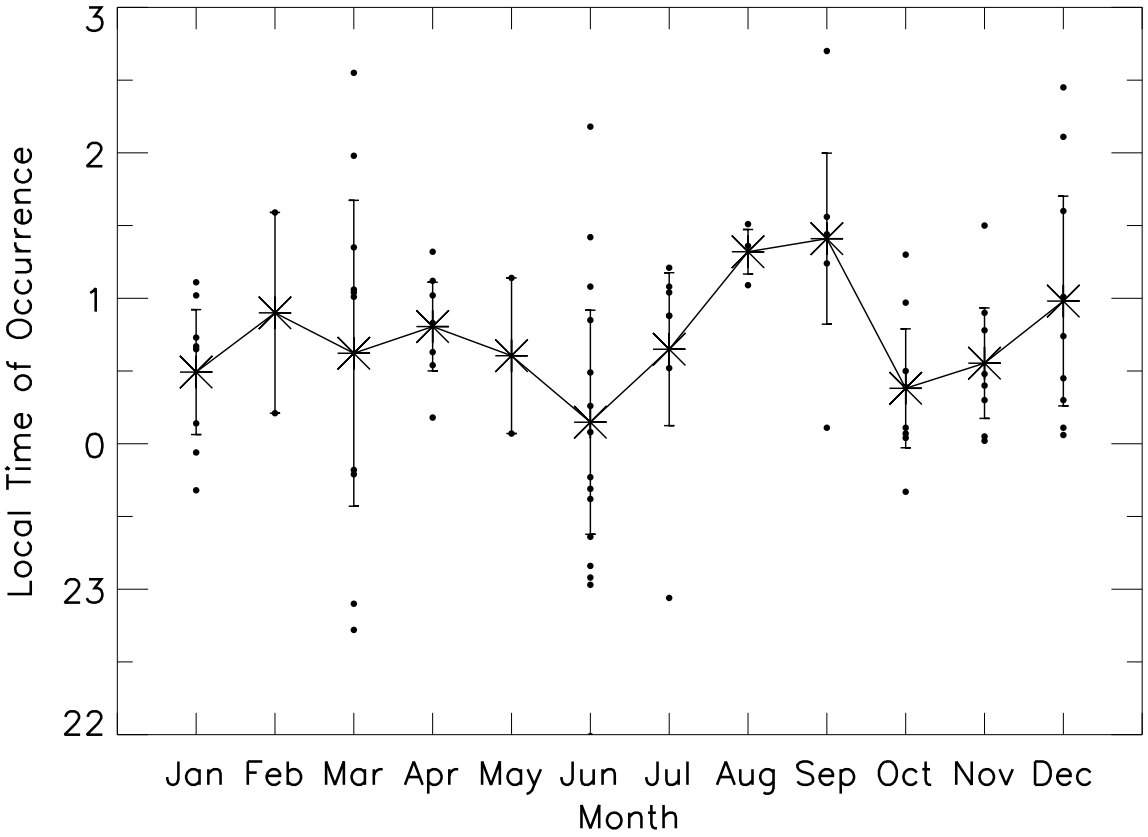

Fig. 3.4: Seasonal behavior of the local time of occurrence of the MTM at 300 km. Asterisks represent the mean of the individual data points at a given month. Error bars represent variability of the data. Some months do not have enough number of points to reach meaningful conclusions.

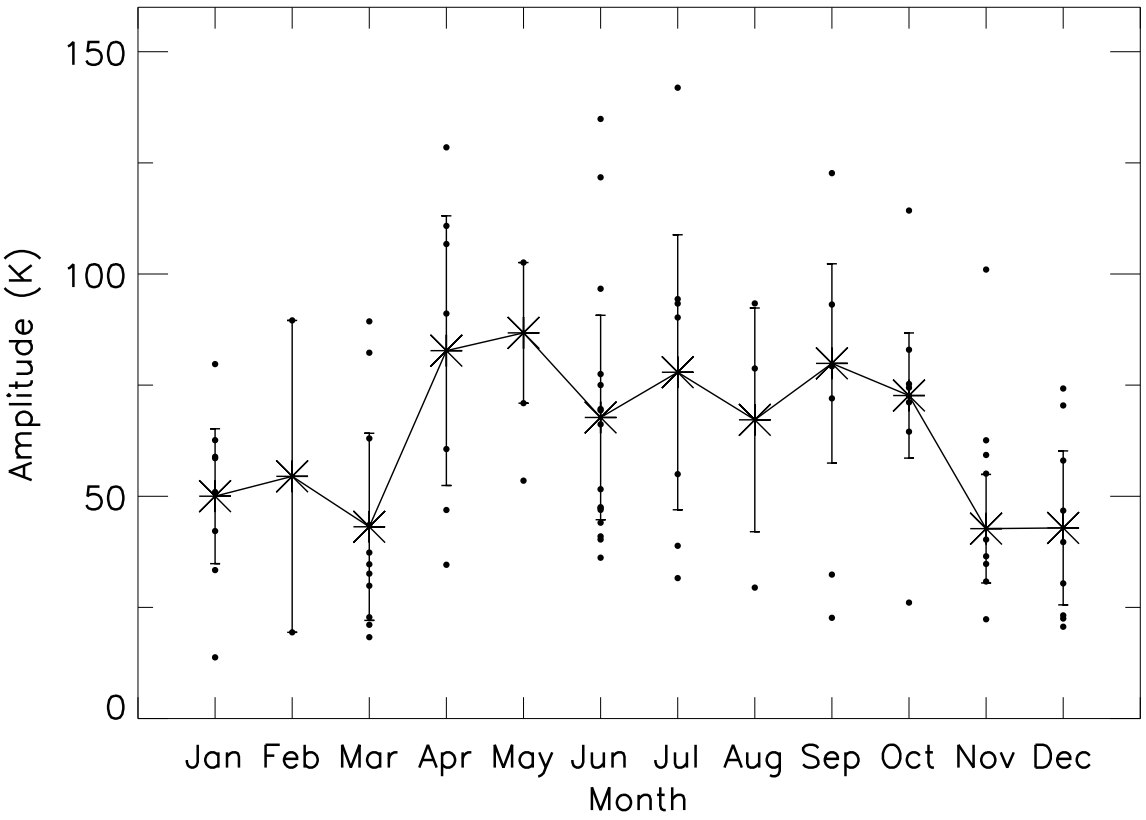

Fig. 3.5: Average monthly MTM amplitudes at 300 km show relatively smaller values during the period November-March. Asterisks represent the average of the individual data points at a given month. The MTM amplitude was defined as the difference between the peak T_i and the interpolated value obtained from the two minima surrounding the MTM.

Our analysis of the MTM was then expanded from 300 km up to higher altitudes since the ISR technique can measure multiple altitudes simultaneously. Figure 3.3 shows T_i at two different heights for 27–28 October 1992. The MTM peak occurs slightly earlier (∼30 min) at the higher altitude. The amplitude of the MTM at 441 km is still large, providing evidence of the large scale (∼100 km) vertical structure of MTM.

As discussed in Section 3.2.1, there was more high quality data available at higher altitudes. We expand our seasonal analysis of the local time of occurrence to 330 km and 367 km altitudes. Figure 3.6 shows the local time of occurrence of the

MTM observed at 330 km (left panel) and at 367 km (right panel), with data shown in the same format as Figure 3.4. The results indicate that the MTM occurs earlier on average during local summer.

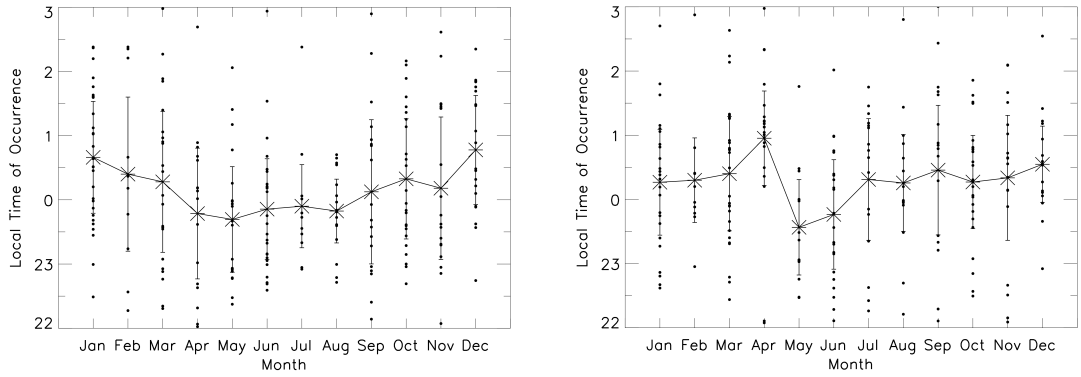

Fig. 3.6: Similar to Figure 3.4 but now at 330 km (left) and 367 (right). Asterisks represent mean values and error bars indicate variability. Although not evident due to the scatter in the data earlier occurrence time seems to be observed in the period April–August at 330 km and May–October at 367 km.

3.2.3 Solar Activity effects on MTM amplitude

The data shown so far cover a wide range of solar activity that could impact the results. Previous studies have not been able to provide evidence on the influence of solar activity on MTM amplitude. Current interpretation of the lack of solar activity dependence involves competing mechanisms that imply a transition from tidal forcing at solar minimum to increased ion-drag at solar maximum (*Meriwether et al.*, 2008). F10.7, the solar radio flux at 10.7 cm, is used as a proxy for solar activity. Figure 3.7 shows a scatter plot of F10.7 versus MTM amplitude at 300 km (red diamonds) and at 367 km (black dots). The result at 300 km, showing only a slight decrease for large F10.7 values, is remarkably similar to the one obtained by *Faivre et al.* (2006), using FPI data at Arequipa, who attributed this apparent decrease to the lack of sufficient measurements at high solar activity. The FPI-determined MTM amplitude also has a large variability, with individual data points showing significant scatter.

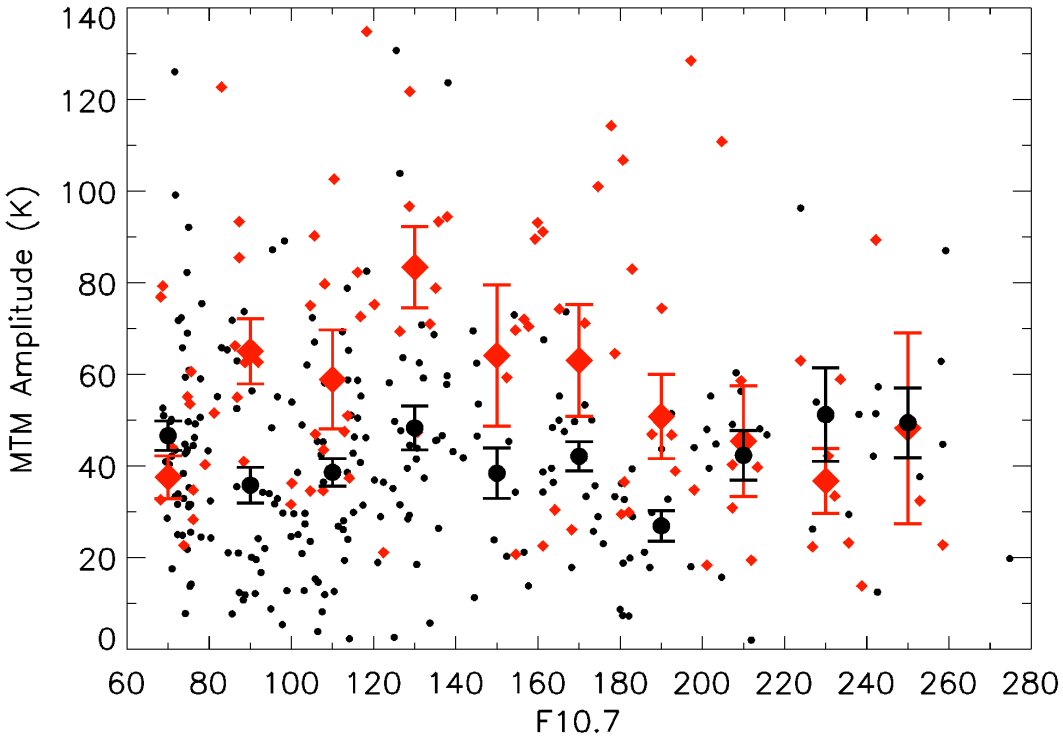

Fig. 3.7: MTM amplitudes at 300 km (red diamonds) and 367 km (black points) plotted as a function of F10.7. Binned data in 20 F10.7 units are also shown as large black circles for 300 km and large red diamonds 367 km. 1 sigma error bars, representing variability in the binned-data points are also indicated.

We have also bin-averaged the data into 20-unit F10.7 bins and plotted the averages and their uncertainties as large symbols with error bars in Figure 3.7 To determine if MTM amplitude has solar activity dependence, a linear fit to the data shown in Figure 3.7 was performed, separately for 300 and 367 km altitude:

$$MTM_{amp} = t_4 + t_5(F10.7 - 150) \tag{3.3}$$

and the results for t4 and t5 are shown in Table 3.1. At 367 km, the uncertainty in t_5 of 0.029 K/(F10.7 unit) means that the limit of detectability with this data set is 2.9 K over an F10.7 range of 100 units, and we detect no trend at that level. At

Table 3.1: Coefficients for MTM amplitude dependence on solar activity

Fit coefficient	Altitude (km)	MTM amplitude
t_4 (K)	300	56.3 ± 3.6
t_5 (K/s.f.u.)	300	-0.087 ± 0.065
t_4 (K)	367	41.2± 1.6
t_5 (K/s.f.u.)	367	-0.01± 0.029
t_4 (K)	300+367	44.4 ± 1.5
t_5 (K/s.f.u.)	300+367	-0.003 ± 0.027

300 km t_5 is slightly larger than the error but the lack of sufficient data points for large F10.7 values means we do not consider it to be a statistically significant result. The combined results for 300 km and 367 km do not have a dependence on F10.7. The observations at Arecibo do not indicate that MTM amplitude is dependent of F10.7.

3.2.4 Model Comparisons

As described in Section 3.1, WAM was the first global model to realistically reproduce the MTM (*Akmaev et al.*, 2009, 2010). Figure 3.8 shows the seasonal variation of the local time of occurrence of the MTM from 250 km to 400 km produced by WAM. The model was run for an entire year, and the hourly outputs were inspected to identify a maximum temperature between 20:00 and 04:00 LT. The vertical bars represent one standard deviation, reflecting a significant day-to-day variability of the MTM (Figure 3.9), also observed in the radar data (Figure 3.6).

In WAM the MTM occurs at earlier local time during local summer, around midnight for 300 km and at ∼23:00 LT for 400 km. The model results do not reproduced month by month the Arecibo data, but the overall trend is in agreement with the radar observations that show, on average, earlier local time of occurrence during summer months. WAM outputs do not exclude pre-MTM or post-MTM effects as the ISR data do. The model shows an earlier local time of occurrence in

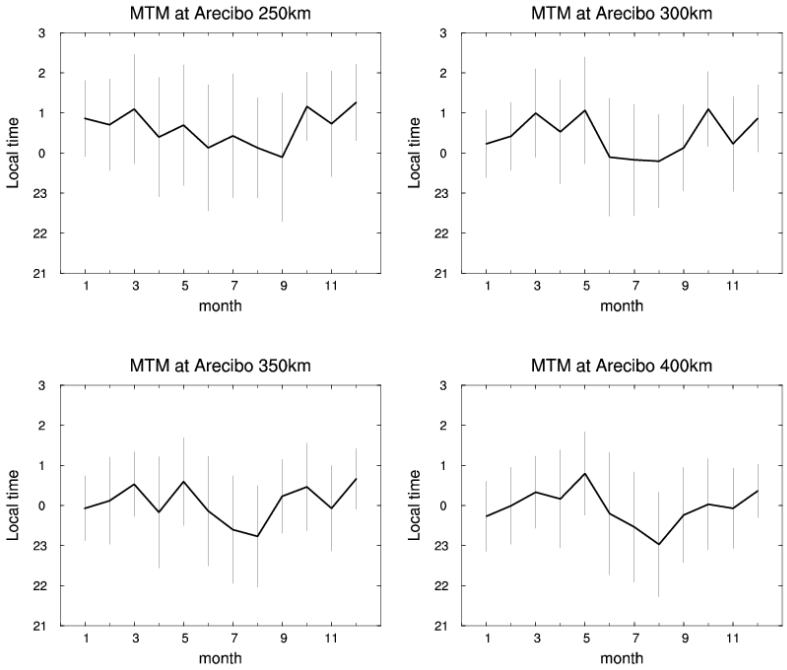

Fig. 3.8: WAM outputs showing the local time of occurrence of the modeled MTM from 250 km to 400 km. Notice the large scatter bars, similar to variability levels observed in the radar data.

summer at 400 km than it does at 300 km, something not observed in the ISR data at 330 km and 367 km. The small difference in altitude between 330 km and 367 km may not be large enough to measure a difference in the time of occurrence. This may indicate that the scale size of the waves that contribute to the MTM is greater than 37 km.

Figure 3.9 shows all available March ISR data for 300 km (left panel) and the model results for the temperature deviation from the zonal mean at 285 km (right panel) adapted from *Akmaev et al.* (2009). The red curve in the left panel represents the average of the data. The average MTM is detected, with an amplitude of ∼45 K and an average local time of occurrence between 00:30 and 01:00 LT. Although there is large amplitude variability in the daily curves of the T_i values due to changes in solar activity, the amplitude of the MTM is does not show the same variability. The

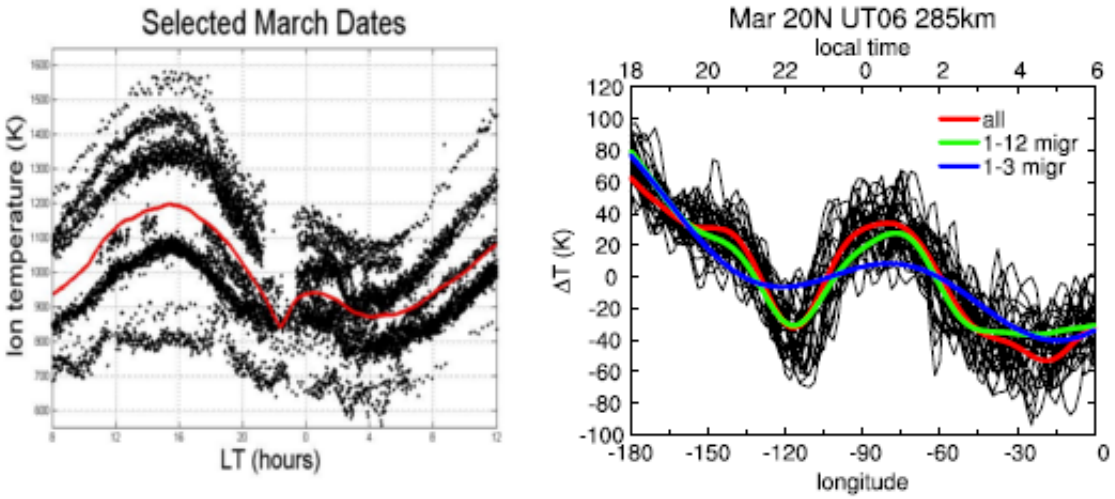

Fig. 3.9: (Left): Ion temperature data for all the March days at 300 km. Notice the variability in the absolute T_i values due to different solar activity conditions. The red curve is the average and a clear MTM is observed between 00:00 and 01:00 LT. The average amplitude is 45 K. (Right): WAM outputs showing the MTM for March at 20o N (adapted from *Akmaev et al.* (2009)). A peak temperature variation of ∼50 K occurs at -75°(∼01:00LT), close to Arecibo's longitude. The general shape of the average curve from the left plot in the time interval 1800LT-0600LT is almost identical to the modeled output at the right.

WAM model output (right panel) shows each day of the month of March (thin black lines). The colored lines recreate the MTM based on the contributions of certain waves int the model. The green line is a monthly mean reconstruction of the signal from the first 12 migrating tides and is responsible for the bulk of the MTM feature. The blue line is a monthly mean reconstruction of the signal from the first three migrating tides and does not reproduce the amplitude in the full model. The red line is a monthly mean reconstruction of the signal from all migrating and non-migrating waves up to zonal wavenumber 12 and frequency 12 day^{-1} (period 2 hours) and is the best representation of the monthly mean of the model output. The model results gives a peak enhancement of ∼50 K at 01:00 LT in good agreement with the ISR data. The blue line does not reproduce the magnitude of the MTM, giving strength to the hypothesis of the need of an amplification of a terdiurnal wave. The model output

from 1800 to 0600 LT shows behavior remarkably similar to the observations, which further supports that the model has accurately captured the generation mechanism of the MTM.

3.2.5 Arecibo MTM Summary

Arecibo ISR ion temperature data collected between 1967 and 2010 were analyzed. For the first time, a fitting method involving a Gaussian amplification of the terdiurnal tidal wave was used to determine MTM characteristics. The seasonal dependence in the time of occurrence and amplitude of radar-determined MTM was also studied for the first time. Due to limitations in the technique to determine T_i at altitudes below the ionospheric peak and/or when large height gradients in Ne exist, only 82 cases were available for study at 300 km, but these results were consistent with those at higher altitudes. At 330 and 367 km the number of nights available increased to 229. MTM signatures were seen as high as 467 km and this is the first time the variation of the MTM with altitude was measured. The MTM tended to occur earlier and to have larger amplitude during local summer months. The similarity of the seasonal behavior of amplitude and local time of occurrence at the different heights provided confidence that the smaller sample of data collected at 300 km can be used to characterize MTM features. No conclusive statistical evidence for earlier local time of occurrence at higher altitudes was found. State-of-the-art model simulations of MTM behavior showed relatively good statistical agreement with the ISR results.

3.3 MTM at Millstone Hill

3.3.1 Data and method

The Arecibo study in the previous section provided new insight into the MTM but in that study we did not explore the spatial extent, in latitude, of the MTM. In order to explore the latitudinal extent of the MTM, observations from previous Millstone Hill (MH) experiments have been analyzed to look for the MTM. In addition, in 2013, we proposed a new experiment with a series of south pointing low-elevation scan measurements using the Millstone Hill ISR (42.6°N latitude, 288.5°E longitude) were conducted. Although the radar is located at mid-latitude, the wide field coverage of its 46 m steerable antenna allows us to determine ionospheric parameters at latitudes as low as 25°N, as shown previously by *Oliver* (1984) in a study focused on exospheric temperatures. This is a new application of this low-elevation technique.

Data were obtained at Millstone Hill using ISR (*Evans*, 1969) at 440 MHz. It has been in its current location at the Massachusetts Institute of Technology Haystack Observatory since 1960, with a wide field capability added in 1978 providing good spatial statistical coverage of the midauroral to subauroral ionosphere. In this study, the ratio of ion temperature to electron temperature is used as a data quality filter such that data are discarded only when the analyzed electron temperature is less than the ion temperature. This occurred most often before midnight at lower altitudes. At mid-latitudes, it is normal for electron temperature to sometimes be slightly greater than ion temperature due to, for example, incoming photoelectrons from the conjugate hemisphere (*Evans and Gastman*, 1970).

The method for processing Millstone Hill observations to obtain data appropriate for MTM studies is described in detail in the following paragraphs due to the complicated geometries that are involved. The low elevation scan capability of the system's 46 m fully steerable antenna was used to probe latitudes as low as 25° N

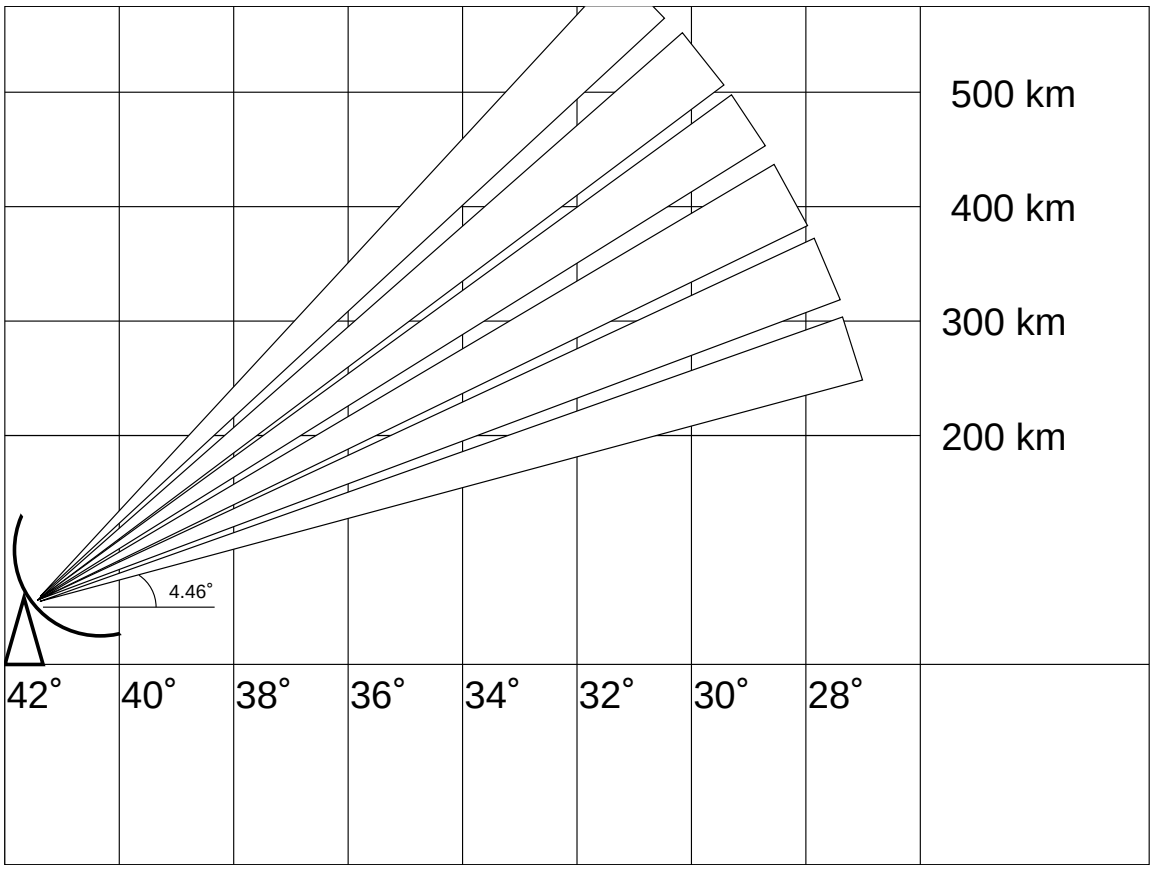

Fig. 3.10: A diagram showing how the Millstone Hill steerable antenna samples various volumes of the ionosphere. Each beam is from a set elevation angle. The ISR returns information at various ranges along the beam, which results in samples from various latitudes and altitudes for a given angle.

over an altitude range of about 200 to 500 km. As the antenna scans in elevation, it collects data across a range of altitudes and latitudes. The scan is executed as a series of fixed elevation positions, with each position providing slant range data over a specific range of altitudes and latitudes. For a zenith pointing antenna, every pulse is directed straight up and thus data at every altitude are from the same geodetic latitude. However, steerable antenna measurements at elevation angles well away from zenith produce data where each altitude is associated with a slightly different latitude. A schematic of this is shown in Figure 3.10. Given the distance to the ionosphere and the angle of the antenna, a straightforward coordinate transformation

gives the altitude and latitude for each data point. The altitude information, and the latitude information, is therefore not separated evenly because of the changing elevation angle of the antenna. To get a time series that is more suitable for this analysis, the latitude range was split into 2° increments and all the data were binned into these discrete values. Then the altitudes are further split into 15 km increments.

The data binning decisions are based on the Arecibo MTM study discussed in Section 3.2. The analysis of the MTM using Arecibo observations showed that it can vary significantly in the 30 km scale range. The small 15 km altitude range chosen to analyze the Millstone Hill data avoids this variation. Another factor involves the radar waveform choice, which determines the spatial resolution of the data. Shorter pulse lengths allow the ionosphere to be probed at a finer spatial resolution, but signal-to-noise ratio is directly proportional to the illuminated volume, so the signal is weaker and harder to detect. The pulse length used in this study is between 640 μs for the highest elevation angle and 2000 μs for the lowest elevation angles during the nights the MTM was observed. The spatial (range) resolution determined by the pulse is along the line of sight, while the vertical and horizontal resolutions are determined by the azimuth and elevation angle of the antenna. The longest pulse length (2000 μs) gives a spatial along-beam resolution of 300 km. At small elevation angles an along-beam resolution of 300 km results in vertical resolution of $\sim$24 km, and the horizontal resolution is slightly less than 300 km (2° of latitude at an altitude of 300km is about 233 km).

We present two nights of data from past experiments with the Millstone Hill ISR and one night from a new proposed experiment, each showing the MTM. The data are displayed in local time, calculated using the longitudes of the measurement volume center. Two representative observations, using Millstone hill data from 1978 to 1990, were selected for good coverage at $\sim$300 km altitudes and because concurrent

observations from the lower latitude Arecibo ISR were available. A third night of data was obtained from observations during our campaign in August 2013. The data binning procedure described earlier yields a time series of temperature measurements at 280 and 310 km. Figure 3.11a shows data from 6 March 1989 at these two altitudes, along with 340 km, at geographic latitude 32°N. Figure 3.11b shows data from the same night at 340 km for three different latitudes, 30°N, 32°N, and 34°N. On this night there is one temperature measurement about every ∼45 min due to the cycle time of the elevation scan. The MTM is persistent enough temporally that this sampling rate still yields several points during both the increase and decrease in temperature, allowing clear detection of the MTM. All three altitudes in Figure 3.11a show an MTM signature, as a local maximum in ion temperature during the night. The center of the maximum is located between 0200 and 0300 LT for each altitude with an MTM amplitude between 100 and 150 K. No significant height dependence in the time of occurrence or amplitude at this latitude is observed.

In Figure 3.11b, the MTM peak occurs between 0200 and 0300 LT with amplitude between 100 and 150 K. No evidence of altitude or latitude variation in the two characteristics of the MTM is observed. Figures 3.11a and 3.11b in combination show that there is a clearly visible MTM in data from Millstone Hill ISR low-elevation scan measurements over a range of latitudes and altitudes.

Another night, 12 July 1988, is shown in Figure 3.12 and a clear MTM can also be seen occurring at ∼0200 LT with amplitude of ∼ 100 K. Here the data are taken from 34°N at 370 km altitude. This result further confirms the radar's ability to observe the MTM relatively far from the equator and also at higher altitudes than were shown for 6 March 1989.

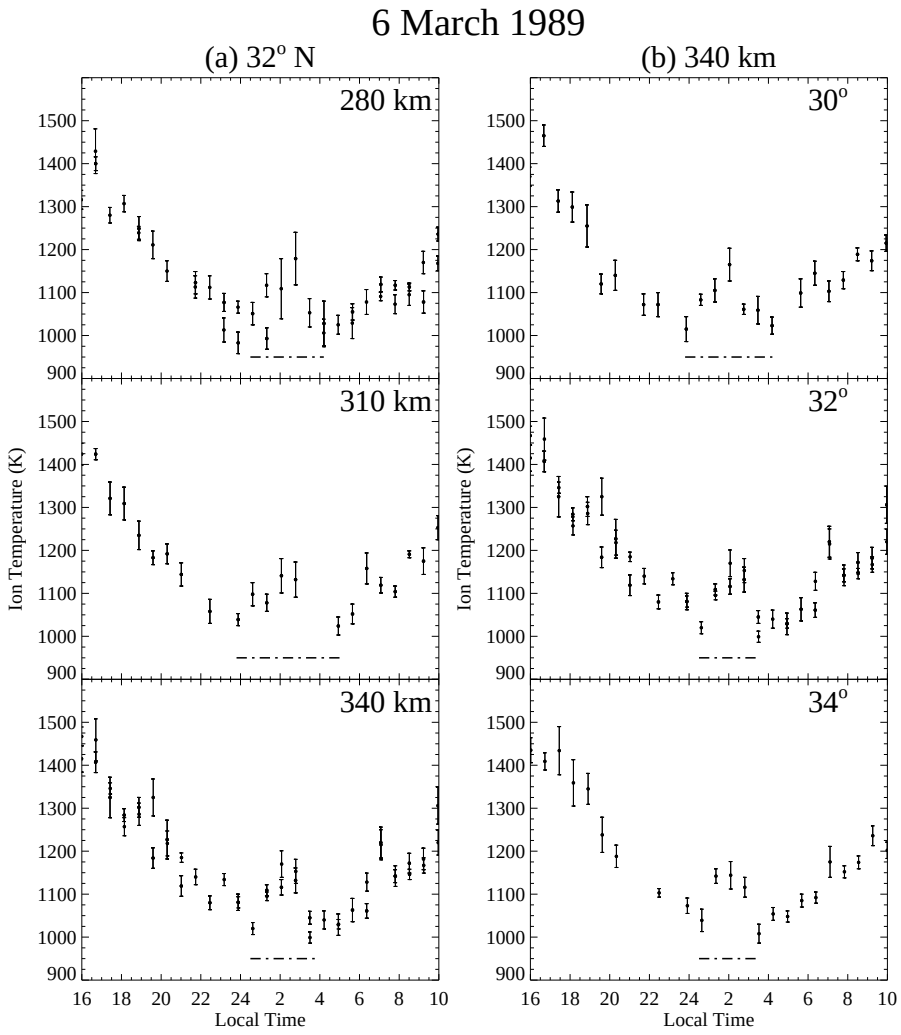

Fig. 3.11: (a) Ion temperatures on 6 March 1989 from the Millstone Hill ISR at 32° N. Altitudes of 280, 310, and 340 km are shown. The dashed line below the data indicates the MTM. The MTM extends from around midnight to 4 LT with the peak occurring after 2 LT. (b) Ion temperatures on 6 March 1989 from the Millstone Hill ISR at 340 km. Latitudes of 30° N, 32° N, and 34° N are shown. The dashed line below the data indicates the MTM. The MTM extends from around midnight to 4 LT with the peak occurring after 2 LT.

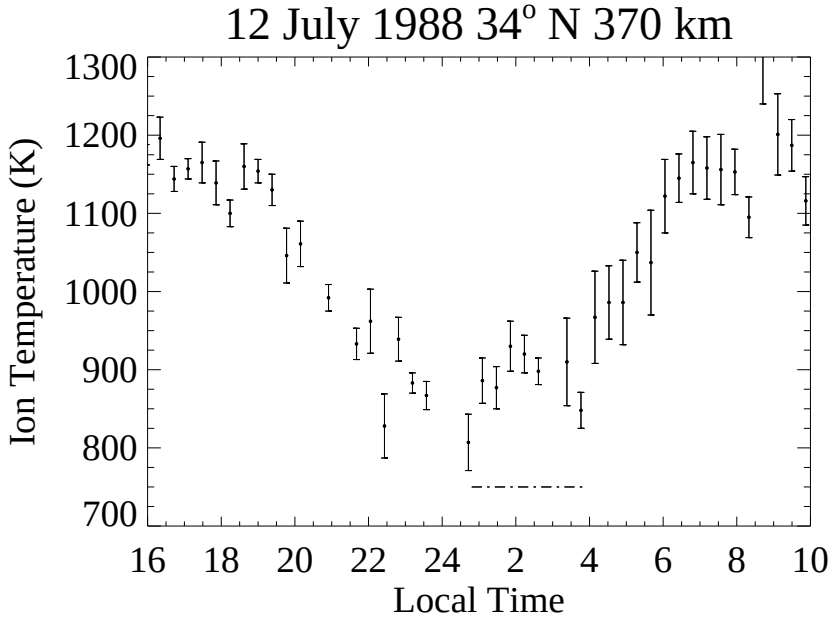

Fig. 3.12: Ion temperatures on 12 July 1988 from the Millstone Hill ISR at 370 km and 34° N. The MTM is indicated by the dashed line below the data. The MTM extends from around 1 LT to 4 LT with a peak shortly after 2 LT.

3.3.2 Comparison with Arecibo

Concurrent observations from Arecibo on these dates further confirm the presence of the MTM. Presented in Figure 3.13a are data from Arecibo ISR (18.3°N) on 6 March 1989 at 293 km and 330 km. These data were fitted by a curve that gives more accurate values of time of occurrence and amplitude. For 293 km the amplitude is about 30 K, and the center occurs before 0200 LT. At 330 km the amplitude is just over 20 K, and the center occurs just before 0200 LT as well. On this date at the higher latitudes observed by the Millstone Hill radar, the amplitude is significantly greater for all altitudes and the time of occurrence is later at all altitudes.

Figure 3.13b shows a very clear MTM observed at Arecibo on the same night as the second example from MH, 12 July 1988 at 330 and 367 km (Figure 3.12). At 367 km it has an amplitude of about 40 K with the time of occurrence just before 01:00 LT. At 330 km the amplitude is similar, but the time of occurrence is closer to midnight. On this night the amplitude is much greater, and the time of occurrence is over an hour later for the higher latitudes, i.e., for MH radar observations.

3.3.3 August 2013 Campaign

The MTM results in the previous section demonstrate the clear detectability of MTM signatures in Millstone Hill low-elevation scan experiments. Based on these findings, a focused experiment designed to look for the MTM at multiple latitudes was conducted on the nights of 13, 14, and 15 August 2013. Four radar observing directions were chosen so that data were acquired at 250 km altitude at 34.2°N, 35.5°N, 36.90°N, and 38.25°N. The results show the presence of a clear MTM at multiple latitudes (approximately 34°N, 35°N, and 36°N) on 13 August 2013. On this night the electron density below 300 km was low for the chosen integration time given Millstone Hill's power and aperture radar parameters. This resulted in low

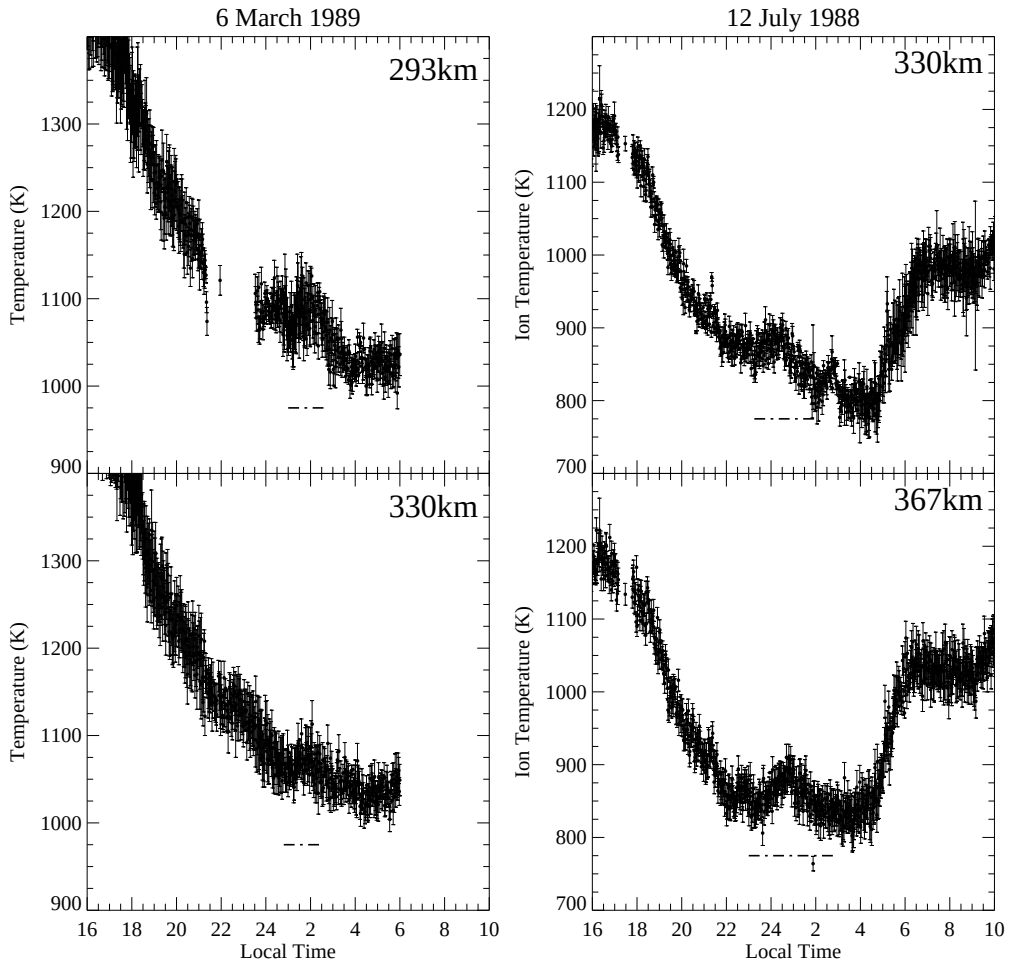

Fig. 3.13: (a) Ion temperatures on 6 March 1989 from the Arecibo ISR at 18.3° N. Altitudes of 293 and 330 km are shown The MTM is indicated by the dashed line below the data. It extends from around 01:00 LT to around 03:00 LT with the peak occurring before 02:00 LT. (b) Ion temperatures on 12 July 1988 from the Arecibo ISR at 18.3° N and an altitude of 367 km. The dashed line below the data indicates the MTM. The MTM extends from around 23:00 LT to 03:00 LT with the peak around 01:00 LT.

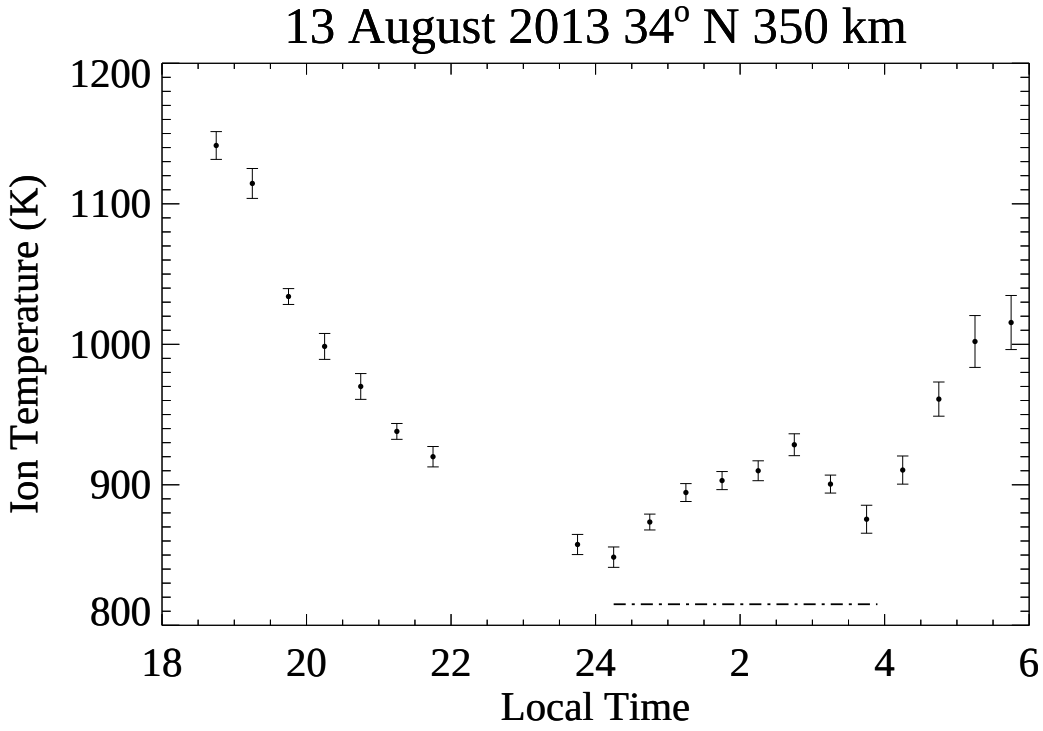

Fig. 3.14: Ion temperatures on 13 Aug 2013 from the Millstone Hill ISR at 34.2° N at 352 km altitude. This data has been binned every half hour to improve MTM detectability. The dashed line below the data indicates the MTM, extending from around midnight to 4 LT with a peak around 3 LT. There is data missing before the MTM because the values during that time are unreliable due to extra instrumental noise during the passage of Cygnus A (a strong UHF radio noise source), leading to analyzed temperature bias. In general, without the Cygnus effect, we expect ion temperatures between 22-24 LT to continue their post-sunset descent seen before 22 LT.

signal to noise, and the variance of the time sequence of measurements is accordingly increased. In general, this decreases the reliability of the data, especially when trying to identify perturbations on the order of 50-100 K. Figure 3.14 shows data from 34°N and 352 km altitude. Radar data points are the result of binning every half hour to increase detectability of the MTM. The MTM is present with a peak occurring around 02:30 LT and an amplitude of ∼90 K.

3.3.4 Discussion

FPI, radar, and all-sky imaging results have suggested a large latitudinal MTM extent, but this is not precisely quantified due to limited measurements above 20°N. We have presented here three nights showing the MTM at latitudes 30°N and higher using MH radar data. During two of these nights there are also concurrent observations with the Arecibo ISR. The July 1988 and March 1989 midlatitude observations show the MTM occurring later at higher latitudes, 30°N and higher, than at Arecibo. In particular, these two cases show a delay of around 1 h for the time of the local maximum between the two locations. This latitudinal time delay has been observed at low latitudes (*Herrero and Spencer*, 1982) and modeled for all latitudes (*Akmaev et al.*, 2009). It is observed as a V-shape distribution of the time of occurrence of the MTM in satellite data. It is named as such because the MTM occurs earliest at the equator and later at both northern and southern latitudes, creating a two-dimensional pattern, in time-latitude space, that resembles a V with the apex on the equator. The delay observed here is consistent with these previous results since the MTM occurs earlier at latitudes closer to the equator. In addition to the time delay there also is an amplitude difference at different latitudes. Where the MTM occurs later, at 30°N and higher, it also has a greater amplitude when compared to Arecibo. The two sites have approximately the same background ion temperature profile, and it is only the temperature change during the MTM that differs significantly.

Recent modeling efforts have been successful in reproducing MTM signatures at latitudes not previously observed. *Akmaev et al.* (2009) have shown, in a run simulating December conditions, that the MTM is expected to extend from around 40°S to around 40°N. Specific examples of the simulated MTM at 30°S and 30°N in December are also presented by *Akmaev et al.* (2009, 2010). Measurements presented here confirm that the MTM can occur at latitudes as high as 34°N. In addition, the

feature is observed as high as 450 km, a result that deserves additional studies in the context of ion-neutral coupling and propagation efficiency. The model results indicate that the MTM is a consequence of an upward propagating terdiurnal wave from the lower atmosphere with no propagation effects from lower latitudes. The model reproduces the time delay that is observed. More detailed observations of variations in the characteristics of the observed MTM at various altitudes and latitudes can be used to infer coupling conditions between the lower and upper atmosphere.

For the recent experiment on 13 August 2013, an FPI, located at the Pisgah Astronomical Research Institute (PARI), was running and taking measurements at the location of one of the ISR scans ($\sim$37°N), assuming that the 6300 Å emission is at 250 km. The PARI FPI (35.2°N, 82.8°W) belongs to North American Thermosphere Ionosphere Observing Network (NATION) (*Makela et al.*, 2012). Along with PARI, FPIs at Eastern Kentucky University and Virginia Tech University allow tristatic observations of neutral winds and temperature. Figure 3.15 (top) shows a comparison between the PARI FPI measurements and nearby radar measurements (36.1°N and 300 km altitude). FPI data points (black circles) are every 5-15 min. ISR measurements (red triangles) are every 15 min. Nighttime ion and neutral temperatures are very similar and an MTM can be seen in both data sets between 01:00 and 04:00 LT. The lines on the figure show the result of smoothing each of the data sets with a three data point window to remove some data scatter. It is a running average that removes some of the scatter in the data. The MTM is more easily seen in the smoothed curve. Figure 3.15 (bottom) shows the same FPI measurements compared with radar measurements at 36.8°N and 255 km altitude. As discussed earlier, the density is low at this altitude, leading to larger observational variability, but despite this fact the FPI and ISR agree very well and the MTM is visible in the smoothed data. The MTM appears to have a smaller amplitude in both the FPI and

ISR data at these altitudes, although it is hard to quantify due to the scatter. The FPI data help to confirm the presence of the MTM and again show the benefit of concurrent observations.

3.3.5 Millstone Hill MTM Summary

Presented here are observations of midlatitude MTM effects with repeatable patterns between 30°N and 34°N using the Millstone Hill ISR in a low-elevation scan mode. These are the first observations at these latitudes using ISR that show unambiguous signatures of the MTM. The two cases from the 1980s have an average MTM amplitude ∼100 K and a peak time of occurrence at ∼03:00 LT. The more recent observation from 2013 shows an MTM amplitude ∼100 K at 350 km, but at lower altitudes it appears to be small. Although the ISR data at lower altitudes are less reliable, concurrent FPI measurements confirm that there is an MTM. The presence of the MTM and the amplitude are consistent with WAM predictions at these latitudes. Simultaneous observations from Arecibo ISR during two of the MTM observations indicate that the MTM also occurred during the same time period at lower latitudes (18° N). This points to large-scale effects generated by coupling from below that produce similar results. Larger amplitude and later occurrence time are found at higher latitudes during these concurrent observations, which are also consistent with the WAM results and in-situ satellite data. This agreement is significant because measurements of the MTM at these latitudes are scarce. No measurements of the MTM at multiple altitudes at these latitudes have been made before.

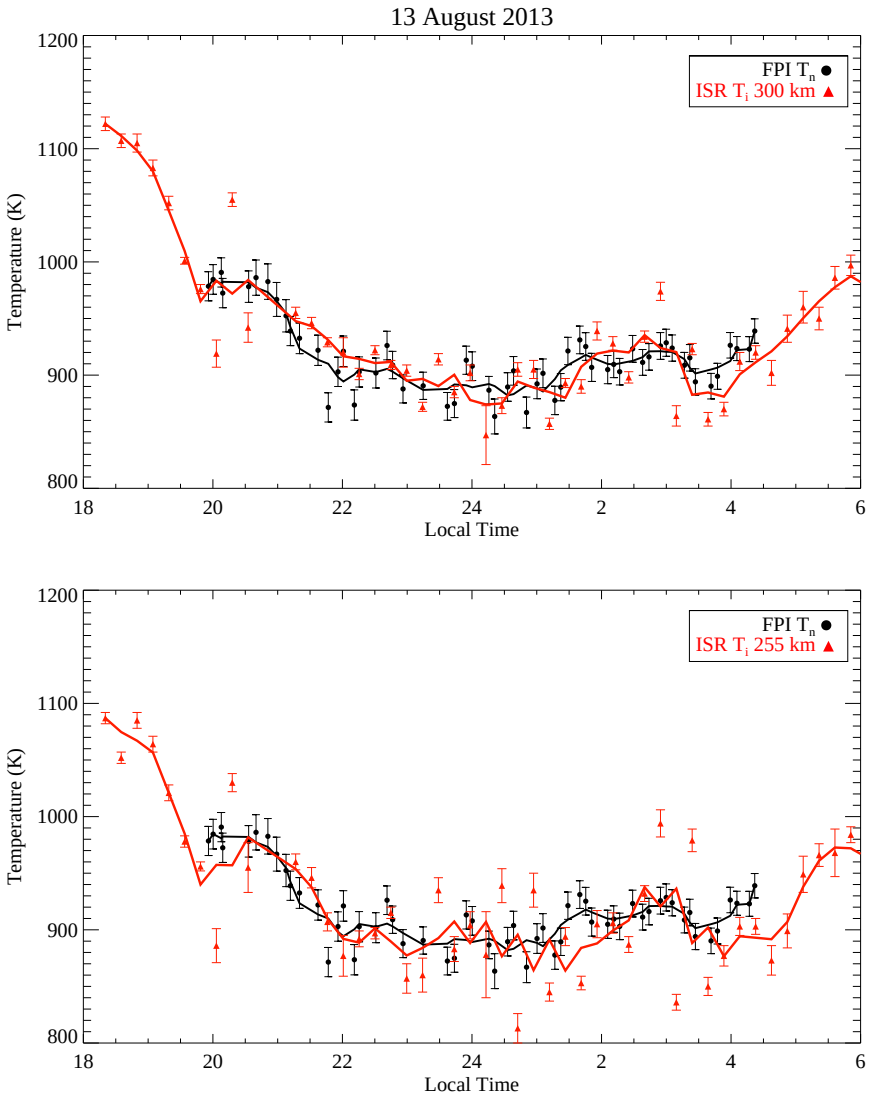

Fig. 3.15: Ion temperatures measured during low elevation scans from the MH ISR and neutral temperatures from the PARI FPI. These instruments are pointed at a common volume at ∼37° N. (a) ISR, red triangles, and FPI measurements, black circles, from 13 August 2013. The ISR data is from an altitude of ∼300km and the FPI is assumed to be at an altitude of ∼250 km. The red line is the result of smoothing the ISR data with a three data point width and the black line is the same for the FPI. The MTM is visible in both the un-smoothed and smoothed data with a peak around 0230 LT. (b) ISR, red triangles, and FPI measurements, black circles, from 13 August 2013. The ISR data is from an altitude of ∼255km and the FPI data is the same as 6a. The smoothed data is also presented. The MTM is harder to detect in the un-smoothed ISR data but is visible in the smoothed data, again with a peak around 0230-0300 LT.

3.4 MTM at Jicamarca

In addition to detecting the MTM with the Millstone Hill and Arecibo ISRs, we also use the main radar in its ISR mode at the Jicamarca Radio Observatory (11.95° S, 76.87° W,0.3° S magnetic latitude). This radar is not steerable and only measures the ionosphere above it. Additionally, at night, the fitting procedure for the Jicamarca ISR spectrum sets the ion temperature equal to the electron temperature, unlike the other two ISR systems presented here. There is also an FPI colocated with the ISR that we use to measure the neutral temperature. To the southwest of Jicamarca is the El Leoncito ASI in Argentina (31.8° S, 69.3° W, 19.7° S magnetic latitude). The El Leoncito ASI is well suited for observations of an optical signature of the MTM, the brightness wave (BW). This allows for comparisons between observations done on the same night. This combination of temperature measurements and airglow measurements from multi-site observations allows for greater coverage of the MTM to better understand its extent morphology. I present here measurements of the MTM using the Jicamarca ISR and a case study of the MTM using the Jicamarca ISR, Jicamarca FPI, and El Leoncito ASI.

3.4.1 ISR and FPI measurements

For this study we use the Jicamarca ISR ion temperatures to determine the temperature increase. Figure 3.16 shows an example of the MTM measured in ion temperature at Jicamarca. The peak of the MTM occurs around 04:00 UT on this night. In a method similar to that in Section 3.2.1 we measured the timing of the MTM using all available ISR data from 1996 to 2013. The ISR does not run every frequently so data is limited. Figure 3.17 shows timing of the MTM at 250 km and 300 km at Jicamarca. At 250 km a total of 39 nights with the MTM were included. At 300 km the total number of nights with the MTM was 50. There is no clear seasonal

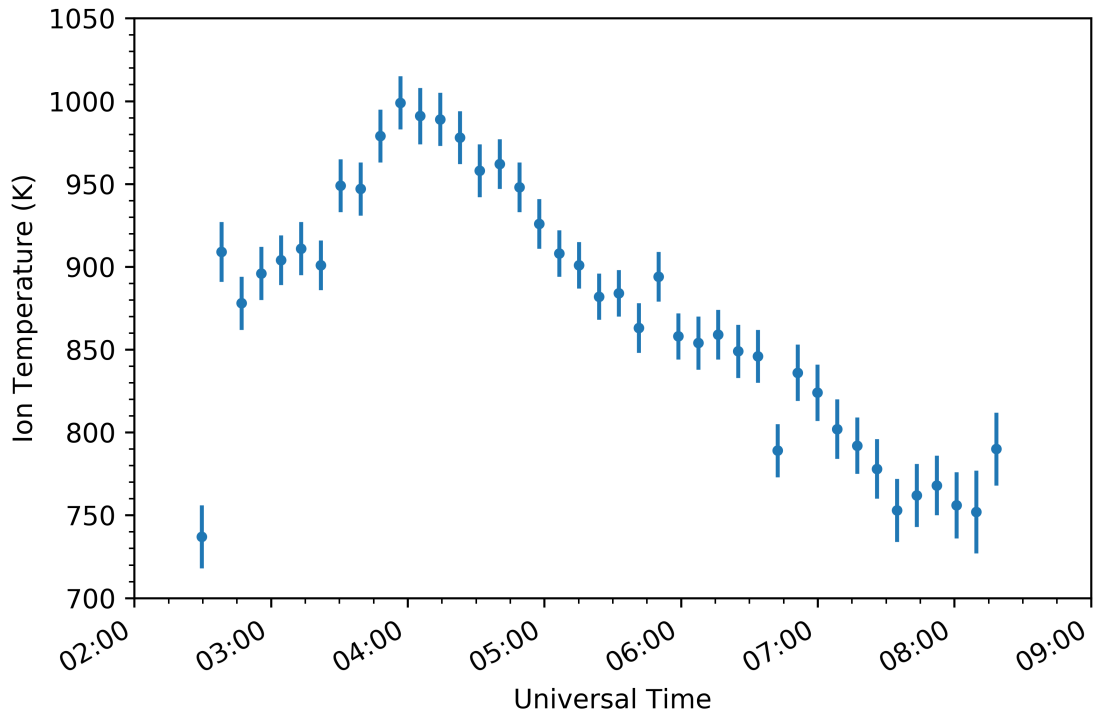

Fig. 3.16: An MTM observed on 11 March 2011. Blue dots show the ion temperatures as measured by the ISR. The peak of the MTM occurs around 04:00 UT (23:00 LT).

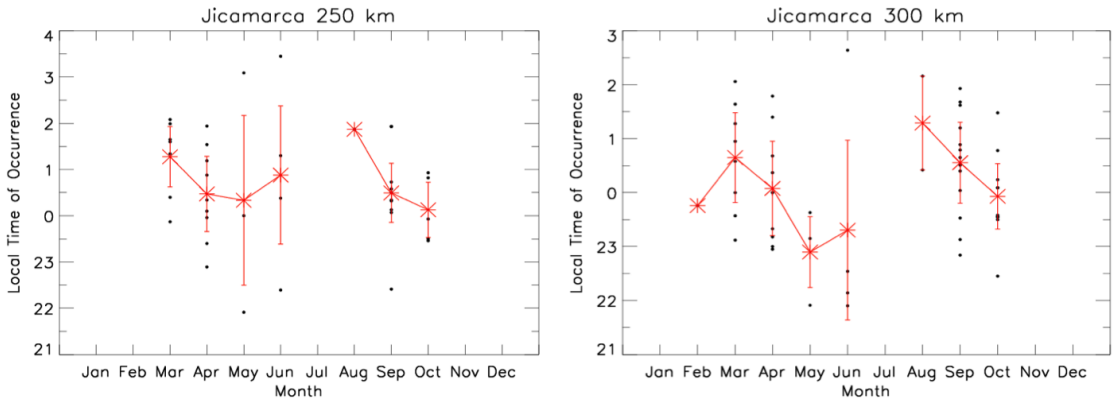

Fig. 3.17: (Left) Local time of occurrence of the MTM at Jicamarca from 1996 to 2013 at 250 km. (Right) Same as left but at 300 km.

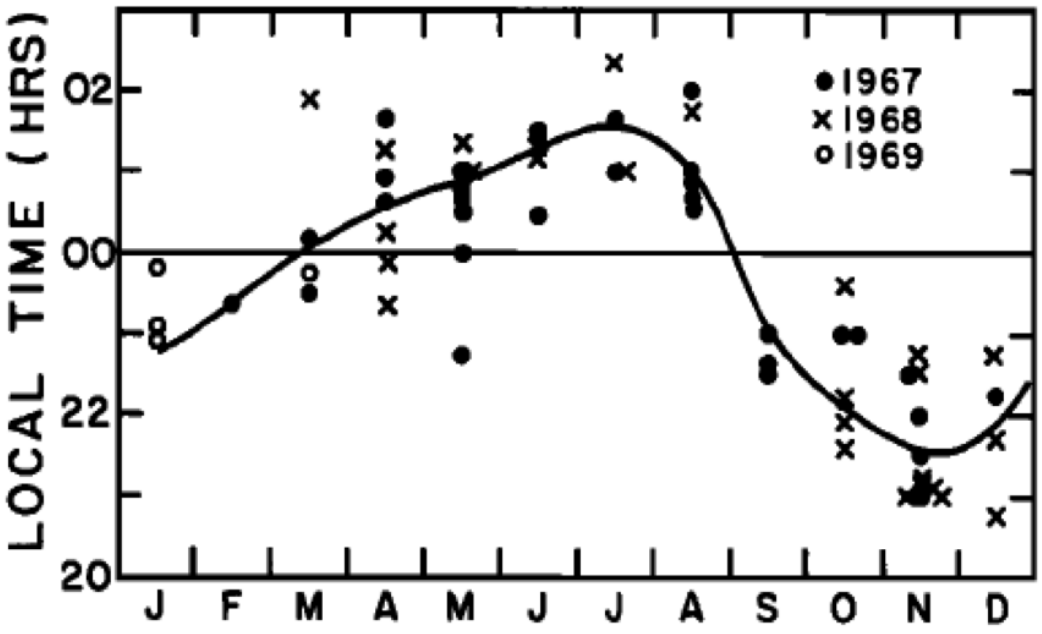

Fig. 3.18: Time of occurence of the MTM from *Bamgboye and McClure* (1982) for each month of the year.

dependence of the MTM from this data set. Previous results using measurements from the 1960s showed a strong seasonal dependence of the MTM (*Bamgboye and McClure*, 1982). Figure 3.18 shows the seasonal dependence of the MTM from this study. This figure indicates that the MTM occurs around 01:00 LT around June solstice and 22:00 LT around December solstice. Although our results do not show a strong seasonal trend, they are not consistent with this previous study.

We now present a case study from 4 April 2014. Figure 3.19 shows ion temperature from the Jicamarca ISR in blue measured about every 10 minutes at an altitude of 250 km on 4 April 2014. This figure also shows measurements of the FPI-determined neutral temperature also at 250 km. This night shows an MTM measured by both instruments. Although we only present one altitude from the ISR measurements, the MTM occurs at multiple altitudes (*Martinis et al.*, 2013; *Hickey et al.*, 2014). The temperature increase begins just before 05:00 UT (00:00 LT) and

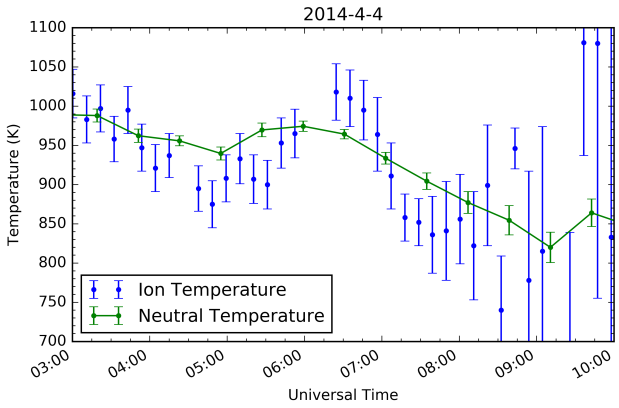

Fig. 3.19: An MTM observed on 4 April 2014. Blue dots show the ion temperatures as measured by the ISR at 250 km. Green points are the neutral temperatures measured by the FPI, also at around 250 km. The peak of the MTM occurs between 06:00 and 6:30 UT (01:00 and 01:30 LT).

the peak of the temperature increase is just after 06:00 UT (01:00 LT). There is very good agreement between the two measurements meaning that the ion temperature is equal to the neutral temperature, as previously shown by *Hickey et al.* (2014). The magnitude of the ion and neutral temperature increases are between 50 and 100 K. Next, we combine these measurements with ASI observations of the BW to extend to higher latitudes and to constrain the morphology of the MTM.

3.4.2 MTM effects at higher latitudes: the brightness wave

Now that we have shown the MTM on this night in ion and neutral temperature measurements we use an ASI to detect the BW associated with the MTM. The BW is a signature of the MTM that can be observed with an ASI at low-latitudes and mid-latitudes due to the dip angle of the magnetic field. In the field of view of the Jicamarca ASI, there was no BW associated with the MTM. The magnetic field lines are mostly horizontal throughout the entire field of view of the ASI so the winds associated with the MTM would not move the plasma downward enough to increase the airglow emission.

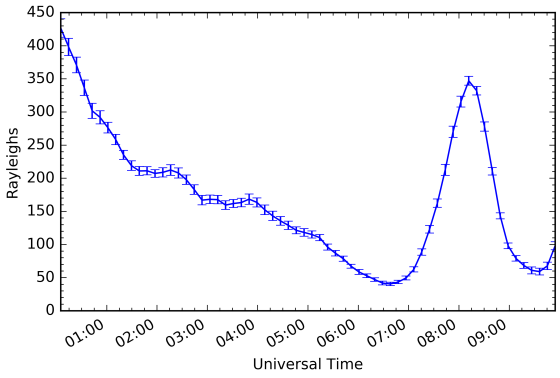

Fig. 3.20: Measurement of brightness in rayleighs measured at zenith with the El Leoncito ASI throughout the night on 4 April 2014. Earlier in the night, in contrast to Jicamarca ASI observations, there is the typical decrease in brightness as the ionosphere decays. The increase in brightness later in the night, with a peak at 8 UT, is a brightness wave.

During this night we observed a BW with the ASI at El Leoncito. Figure 3.20 shows the intensity calculated from a 16x16 pixel box at zenith. At El Leoncito the emission is greater early in the night and decreases throughout the night. This is partially due to the fact that the rising of the F-layer early in the night at Jicamarca, the source of the equatorial fountain effect, moves the plasma toward El Leoncito, increasing the airglow emission. Additionally, since the F layer does not rise in altitude during this time at El Leoncito, the lower altitude of the plasma creates greater emission. As the night goes on, recombination leads to a decrease in the ionosphere and a decrease in the emission at El Leoncito. At around 06:30 UT the brightness begins to increase until it reaches a peak just after 08:00 UT. This increase in brightness is what we define as a BW and associate with the MTM. The BW has an apparent propagation from the north-east to the south-west in the ASI images, as observed by *Colerico et al.* (2006) and the sequence of images (not shown) from this night.

If we assume that the MTM propagates from Jicamarca to El Leoncito, then we can determine the propagation speed. The time delay between the peak of the MTM and the peak of the brightness wave is approximately two hours and this would result in a speed of about 330 m/s. This is consistent with the result of a phase velocity of the BW of 200-400 m/s from *Colerico et al.* (2006) but the Jicamarca ASI is located almost 8° to the west of El Leoncito so if the source of the brightness wave was the MTM at Jicamarca, it would not propagate from the north-east to the south-west as is observed. The MTM occurs over a wide range of longitudes (*Herrero and Spencer*, 1982) and no dependence on longitude has been observed (*Spencer et al.*, 1979), i.e., the MTM occurs near local midnight at all longitudes and thus follows the apparent motion of the Sun (*Meriwether et al.*, 2013; *Colerico et al.*, 1996). From this we expect that at an earlier UT an MTM should occur to the east of Jicamarca. We use the velocity of the brightness wave to determine where the source MTM should be located. The apparent meridional velocity of the brightness waves is 280 m/s. At this speed it would take about 2 hours to travel from Jicamarca's latitude (11.95° S) to El Leoncito's latitude (31.8° S) along a constant longitude. The Earth is rotating beneath the MTM so during this time the MTM will be traveling to the west with the speed of the Earth's rotation. With this speed, we find that it would have originated from 38.1° W at about 06:00 UT. This is the same time that the MTM is observed at Jicamarca. Given that the MTM follows the apparent motion of the Sun, at approximately the anti-solar point, we do not expect that it should occur at the same UT at two locations separated by 38.8° of longitude. The timing of the MTM at Jicamarca leads us to expect an MTM at around 03:40 UT at 38.1° W, over two hours earlier than is expected from the brightness wave observations. Our observations are not consistent with an MTM propagating south from a lower latitude.

We present another explanation for the time delay between the observation of the MTM at Jicamarca and the BW occurrence at El Leoncito, based on global model results of the MTM. *Akmaev et al.* (2009) used a whole atmosphere model (WAM) the reproduce the MTM that shows an apparent poleward motion due to its morphology. The simulated MTM occurs over a range of latitudes and longitudes such that it makes a sideways V-shape in longitude-latitude space. The vertex of the V is located close to the equator and and is oriented so that the two points of the V are to the east. This model is also consistent with satellite measurements from *Herrero and Spencer* (1982) that showed a horizontal V-shape structure in time and latitude in the temperature enhancement near 285 km, with earlier occurrence time near the equator and later times near the northern and southern tropics. In WAM, the whole structure migrates westward following the apparent motion of the sun. As a result the MTM occurs earliest at the vertex of the V, near the equator, and occurs later at higher latitudes. WAM outputs are consistent with our result that the MTM occurs first at Jicamarca and that the BW at El Leoncito appears to propagate to the southwest.

3.4.3 MTM at Jicamarca Summary

We have presented here observations of the MTM at the magnetic equator and a related brightness wave at a higher latitude. Our results on the seasonal time of occurrence of the MTM at Jicamarca is not consistent with past studies. At Jicamarca, observations of the MTM were made with both the FPI and ISR, showing the temperature increase in neutrals and ions. The brightness wave occurs later in the night in the ASI images from El Leoncito. The timing of the two events is not consistent with an MTM propagating south from a lower latitude and instead supports the explanation that the MTM occurs over a range of latitudes and longitudes (in a sideways V-shape) and follows the apparent motion of the Sun.

3.5 MTM Summary

The three studies presented in this chapter provide new measurements of the MTM. At Arecibo we were able to detect the MTM at multiple altitudes up to 467 km, occurring earlier and with a larger amplitude during local summer months. In the second study we detected the MTM above 30° N with the Millstone Hill ISR, the first time this was achieved using low-elevation scans. Simultaneous observations with the Arecibo ISR during two of the MTM observations indicate that the MTM also occurred during the same time period at lower latitudes (18° N). Larger amplitude and later occurrence time are found at higher latitudes. Our results on the seasonal dependence of the time of occurrence of the MTM at Jicamarca were inconclusive but they were not consistent with a previous study on the seasonal dependence of the MTM from *Bamgboye and McClure* (1982). We compared the timing of a BW with the timing of the MTM at Jicamarca and find that our observations are not consistent with an MTM propagating south from a lower latitude, as has been suggested in previous studies. Our interpretation is that the MTM occurs over a range of latitudes and longitudes, making a sideways V-shape, and that the whole structure migrates westward following the apparent motion of the sun. The observations from the Arecibo and Millstone Hill studies also support this hypothesis. This is the same interpretation that was presented in *Akmaev et al.* (2009). The model results from WAM are consistent with all the observations presented here. The concurrent observations of the MTM at multiple latitudes and altitudes support idea that the MTM is generated by an interaction of atmospheric tides that can be traced to the lower atmosphere (*Akmaev et al.*, 2009) and that the MTM does not propagate from low-latitudes to higher latitudes but instead occurs over a span of latitudes and that the entire structure moves westward.

Chapter 4

Understanding the development and evolution of ESF through ASI observations

4.1 Introduction

Equatorial spread F (ESF) is the name commonly given to plasma irregularities that typically occur after sunset in the equatorial and low latitude F region. They are attributed to plasma bubbles, depletions in the background plasma that begin to form due to the generalized Rayleigh-Taylor instability (*Hysell*, 2000). These plasma bubbles contain structures that cover many different scale sizes. Radar systems pointed perpendicular to the magnetic field are able to look at coherent backscatter from field aligned irregularities with scale sizes that are equal to half the wavelength of the radar. These systems have been used extensively for ESF observations and are some of the most well known. Observations of ESF with radar are generally categorized into three distinct types of features: bottom-type, bottomside, and topside (*Woodman and La Hoz*, 1976). Their names refer to where they appear relative to the F-layer. Bottom-type layers are narrow layers of irregularities that do not show much vertical development and occur below the F peak. Bottomside irregularities are also limited to a small layer but are more structured and developed and occur around the F peak. Topside irregularities are plumes that reach up to the topside of the ionosphere, above the F peak. At Jicamarca, Peru, an incoherent scatter radar (ISR) operating at 50 MHz has been widely used to observe ESF irregularities at

3 m scale size (*Woodman and La Hoz*, 1976; *Fejer et al.*, 1999). In addition handful of radars at different longitudes exist to study ESF: the ALTAIR radar (9°N, 167°E, 155.5 MHz and 415 MHz) (*Tsunoda*, 1980) and the Christmas Island radar (2°N, 202.6°E, 50 MHz) in the Pacific Ocean (*Miller et al.*, 2010); the São Luís radar (2.59°S, 44.21°W, 30 MHz) in Brazil (*Rodrigues et al.*, 2008) and the Equatorial Atmosphere Radar (EAR) (0.2°S, 100.32°E, 47.0 MHz) in Indonesia (*Otsuka et al.*, 2004). These radars detect irregularities with scale sizes from 0.36 m to 5 m.

One way to probe much larger scale sizes, 10's -1000's km, is to use an all-sky imager (ASI). This has previously been done away from the magnetic equator, where the features map to higher altitudes at the magnetic equator (*Martinis and Mendillo*, 2007; *Mendillo et al.*, 2005; *Makela and Kelley*, 2003). The Jicamarca, Villa de Leyva, and El Leoncito ASIs, described in Section 2.1.2, are used for observations of the large-scale structure of ESF in this chapter. The Villa de Leyva and El Leoncito ASIs are located such that they are at approximately magnetic conjugate points. Figure 4.1 shows the fields of view of the three ASIs for an 80° zenith angle at 250 km. These ASIs measure the large scale structures of ESF. These are regions of lower electron density and appear as darker regions in the images. This is discussed in more detail in Section 4.2. The information provided by ASIs is enhanced when combined with other instruments. Throughout this chapter the observations from ASIs are combined with other instruments to provide a more comprehensive view of ESF. I use radar systems and an FPI measurements for this comparison.

Prior to the publication of the papers that are the focus of this chapter (*Hickey et al.*, 2015, 2018) the comparison between simultaneous observations of ESF using radars and ASIs had yet to be done at Jicamarca. The Equatorial Atmosphere Radar (EAR) was used with an ASI to study from one night in April, 2003 when there were field aligned irregularities occurring within the airglow depletions. The area with

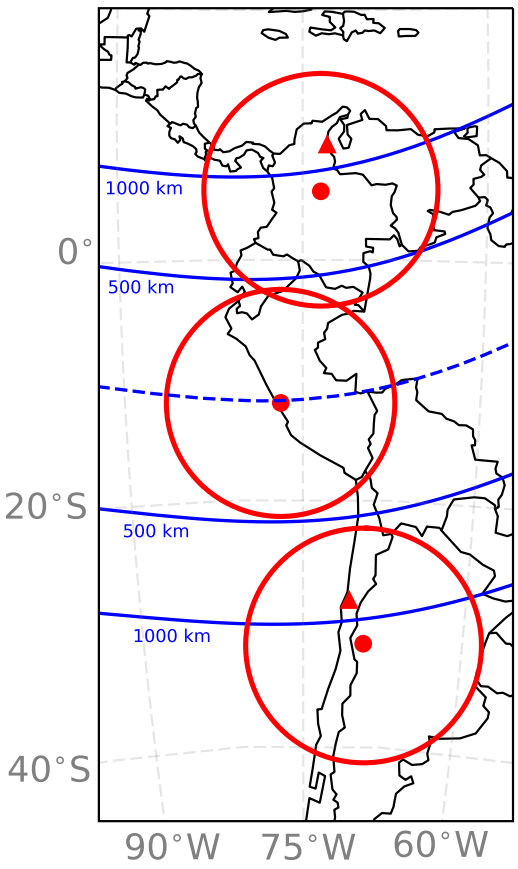

Fig. 4.1: A map of western South America showing the location of the Villa de Leyva (top), Jicamarca (middle), and El Leoncito (bottom) ASIs as red dots. The red circles around the dots are the fields of view for an airglow layer at 250 km and a zenith angle of 80°. The red triangle in the Villa de Leyva field of view is the conjugate location of the El Leoncito ASI. The red triangle in the El Leoncito field of view is the conjugate location of the Villa de Leyva ASI. The blue dotted line is the magnetic equator and the solid blue lines are lines of constant magnetic apex altitude.

the most intense backscatter was found to be in the center of the depletion (*Otsuka et al.*, 2004). *Mendillo et al.* (2005) showed the process of mapping airglow depletions along magnetic field lines and showed a case study of simultaneous radar backscatter and optical data. *Miller et al.* (2010) conducted a similar study using an ASI in Hawaii looking south and the Christmas Island radar, which, like Jicamarca, also

observes 3 m irregularities. They also found that the backscatter at high altitudes comes from the center of the depletions. Since none of these studies were done at the magnetic equator, in order to compare the data from both instruments, they had to project the radar data onto the ASI images. This projection is done assuming that the irregularities will map perfectly along the field lines. The detected echoes were from high altitude plumes (h$>$ 400 km).

In this chapter I compare observations from ASIs with other instruments to better understand the development and evolution of ESF and the background ionosphere that it exists in. The ASIs allow for investigations of the large scale morphology and radar systems allow for investigations of the small-scale irregularities. Using ASIs, I observe how ESF evolves and look for patterns in its morphology. A combination of ASIs and radar systems are used to understand the connection between the large-scale and small-scale aspects of ESF. Additionally, I use the Jicamarca ASI as a way to measure the background motion of the ionosphere. These multi-instrument observations provide a more complete picture of the formation, evolution, and morphology of ESF.

4.2 Observing ESF with ASIs and Radar

The ASIs operated by the Boston University Imaging Science Team operate every night except for a few nights around full moon, from sunset to sunrise. The ASIs are used to study a variety of science objectives. We are interested in the observations of signatures of ESF. The work in this section has been published in *Hickey et al.* (2018). For the observation of ESF features we use the 6300 Å and 7774 Å filters. Large scale ESF structures (10-500 km) can be observed as airglow depletions within the field of view ASIs (*Weber et al.*, 1978). These structures are regions that have less plasma and thus are darker than the background. Depletions can be associated

with three types of ESF: bottom-type, bottomside, and topside (*Woodman and La Hoz*, 1976). The large scale structures of topside ESF are often referred to as plumes or plasma bubbles. At the magnetic equator we observe bottomside ESF and these structures appear as dark bands oriented along magnetic field lines.

4.2.1 ESF observations at Jicamarca

The ASI at Jicamarca has the advantage of being located at magnetic equator along with a variety of other instruments. This provides a unique opportunity for measuring features associated with ESF. We are able to compare the large scale ESF features with the small scale irregularities during concurrent observations with the ASI and JULIA mode. At other times, when the ISR is running we are able to measure the ionospheric parameters to remove ambiguities in the ASI observations.

Figure 4.2 shows an example of raw (left) and unwarped (right) all-sky images taken at the Jicamarca Radio Observatory on 3 April 2014. To unwarp the image we assume an emission height of 250 km and use zenith angles between 0° to 80° to determine the longitude and latitude of each pixel. We then overlay a geographical map with grid lines. We subtract the background image from the 6300 Å image, divide by the exposure time, and multiply by a constant factor to determine the emission in rayleighs (*Baumgardner et al.*, 2008). We remove the stars from the images using an algorithm that replaces brighter pixels with the median of the surrounding pixels. The plasma depletions in the raw images are curved and extend from north to south, covering the entire field of view. In the unwarped images they are visible as mostly straight bands that are aligned in the N-S direction.

On some nights, such as the night presented in Fig. 4.2, we can use the ISR mode of the Jicamarca main array to measure electron density, ion temperature and electron temperature at multiple altitudes concurrently. These measurements are used to compare with and add context to the ASI observations. This radar mode uses

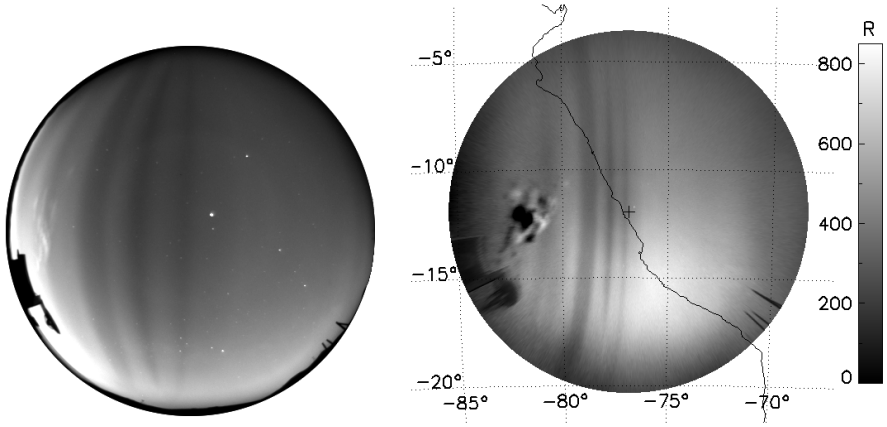

Fig. 4.2: (left) A raw image at 05:18 UT on 3 Apr 2014 from the Jicamarca ASI. The exposure time is 120 s and the image was obtained using a 6300 Å filter. Clouds are visible on the left edge of the image. (right) The unwarped image. The top of the image is north and the left of the image is west. The western coast of South America is seen as a black line and the location of the ASI is marked with a small black cross. The dotted lines are geographic latitudes and longitudes. Latitude and longitude is determined for each pixel and the image is transferred to a map projection. The gray scale shows the brightness in rayleighs. Clouds low on the horizon are now more prominent in the unwarped image. They also contain dark areas due to background subtraction.

much more power than the JULIA mode and thus is not run as frequently. Figure 4.3 shows a range-time-intensity (RTI) plot from the ISR, where intensity depicts electron density, on 3 April 2014, a night when many depletions were observed with the Jicamarca ASI, as seen in Fig 4.2.The region near the peak of the ionosphere of the ionosphere is visible as the blue region. The peak of the F region is over 500 km at the beginning of the night and then moves down to 300 km. The brightness of ASI images are mostly determined by the height and density of the F region, measured by the ISR, so early in the night we expect weak airglow.

On a different night we also have concurrent measurements of ESF at Jicamarca with the ASI and the JULIA mode of the main array. Typically, the coherent and incoherent radar modes do not operate at the same time so we can only compare with one on a given night. On 29 October 2014 both the JULIA mode and the ASI

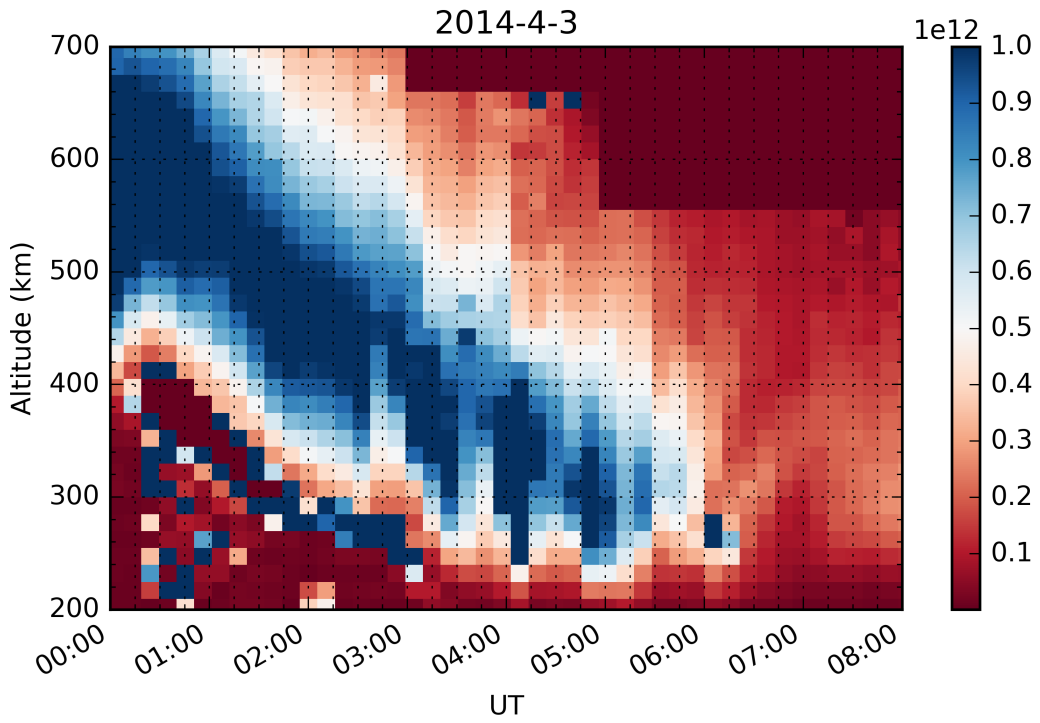

Fig. 4.3: A range-time-intensity (RTI) plot from 3 April 2014 showing electron density as a function of altitude and Universal Time. The highest density region that moves down through the night is the F-layer. Regions of low density associated with depletions are seen beginning just before 3 UT.

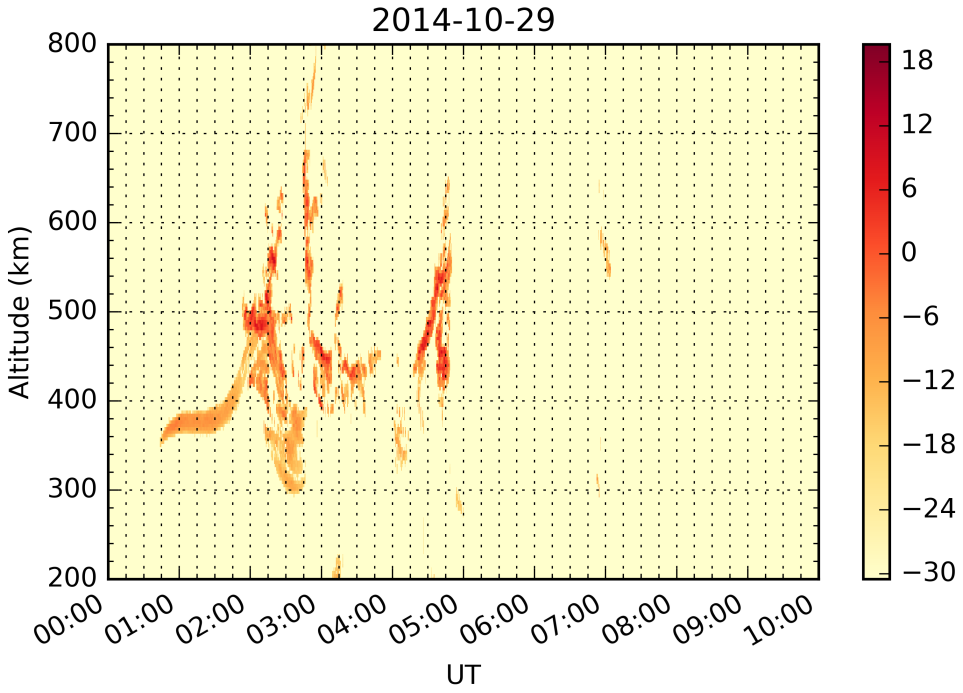

Fig. 4.4: A range-time-intensity plot from 29 October 2014 showing signal-to-noise in dB as a function of altitude and Universal Time. On this night bottom-type, bottomside, and topside ESF irregularities are visible.

detected features associated with ESF. Figure 4.4 shows a RTI plot from the JULIA mode. Here, the intensity shows the signal to noise ratio of backscatter from 3 m irregularities as they pass over the radar. Figure 4.4 should not be interpreted as a two-dimensional spatial representation of ESF. These features evolve as they drift past the radar (*Hysell and Burcham*, 2002). Figure 4.4 is useful for determining when and where irregularities occur above the radar. From around 01:00 to 02:00 UT there are bottom-type radar echoes and after that bottomside and topside echoes appear. The topside irregularities reach almost 800 km. After about 05:00 UT no strong irregularities are observed.

Having determined the determined the presence of small scale irregularities, we next turn to structures measured by the ASI. Figure 4.5 shows three ASI difference

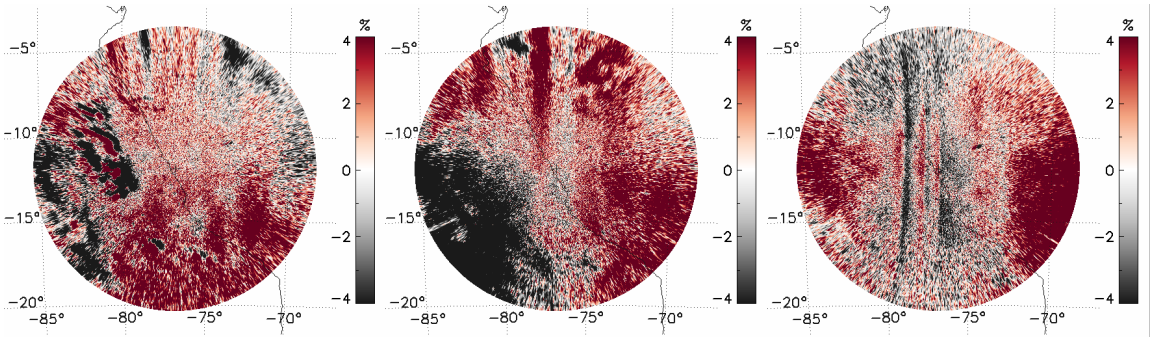

Fig. 4.5: Three unwarped difference images from 29 October 2014. These images show the difference between two consecutive images by subtracting the earlier image from the later image. These images are then scaled to their average value in order to show percent increase and decrease. Red is positive, black is negative, and white shows no difference and the color scale shows the difference values in percent. This technique brings out details that may not be as clear in images like Fig. 4.2. Airglow depletions in these images are visible as alternating red and black regions. Coordinates show geographic latitude and longitude. The plus sign in the middle is the location of the ASI. The black line shows the western coast of Peru. (left) Unwarped image 03:36 UT (LT=UT-5). Clouds are responsible for the black patches to the west of -80°. Depletions are visible at the northern edge of the image. (middle) Unwarped image at 04:31 UT. The red band around-77° and adjacent regions show the presence of a depletion extending from the north down past zenith. (right) Unwarped image at 9:08 UT. Three depletions are visible between -80° and -75° longitude.

images from this same night. The difference images are created using two consecutive images and subtracting the earlier image from the later image. This makes faint features easier to detect. The difference image in the left panel is from 03:36 UT, about 3 hours after sunset (LT=UT-5), and faint depletions are visible only at the top of the image due to weak emission at zenith. The middle of Fig. 4.5 shows a difference image at 04:31 UT. A depletion is visible through more of the image as the overall 6300 Å emission increases. The right side of Fig. 4.5 is an image from 09:08 UT and now the emission is greater and three depletions extending from north to south are visible.

4.2.2 Airglow Modeling

To further analyze the observations at Jicamarca, we perform a detailed analysis of airglow brightness at the magnetic equator. The airglow emission at a given wavelength is a measure of the number of photons emitted by a particular reaction in the upper atmosphere. In this section we focus on 6300 Å emission. An absolute calibration of this allows for a more detailed analysis of the images because the brightness can be directly related to the atmospheric parameters. Although operating an ASI at Jicamarca has the advantage of being colocated with many instruments, magnetic field orientation at the magnetic equator that supports the creation of ESF also complicates ASI observations. The intensity of the airglow emission depends on the plasma density and its altitude distribution. If the peak of electron density occurs at a high altitude then the airglow emission at 6300 Å is weak. Just after sunset at the magnetic equator there is a large upward $\mathbf{E} \times \mathbf{B}$ drift due to an enhancement in the zonal electric field known as the pre-reversal enhancement (*Fesen et al.*, 2000). This upward drift raises the F-layer early in the night (See Figure 4.3, and during this time it is difficult to observe with the ASI due to very low airglow signal (see Figure 4.5. We show in Fig. 4.6 (top) the measurement of brightness (in rayleighs) at zenith from the ASI throughout the night of 3 April 2014. The values are an average from a 16 x 16 pixel (corresponding to a spatial area of about 70 x 70 km) box centered at zenith in the unwarped images. The error bars are the standard deviation in this measurement. Additionally, by testing the imagers that we operate we have determined that there is a calibration uncertainty of about 20%. No data is available between 00:00 and 01:00 UT due to cloudy conditions. Missing data later in the night are also due to clouds.

From 00:00 to 02:00 UT the brightness is low but then increases to reach a peak around 05:00 UT. After this time the brightness decreases until the end of the night.

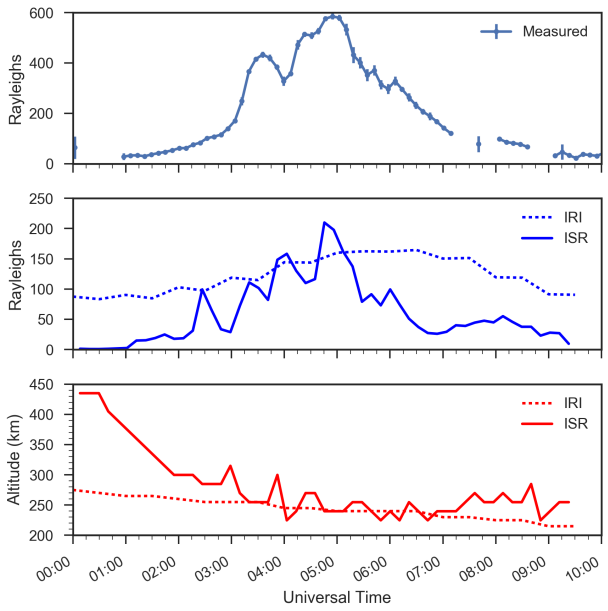

Fig. 4.6: (Top) 6300 Å emission at zenith on 3 April 2014 as a function of Universal Time. Brightness values are in rayleighs. Episodic decreases in brightness at 4 UT and later are due to depletions passing through the field of view. (Middle) A model output from the BU airglow model showing brightness in rayleighs as a function of Universal Time. The dotted line uses IRI for values of electron density and plasma temperature and the solid line uses data measured by the ISR at the Jicamarca Radio Observatory. The vertical axis is a different scale for the top and middle. (Bottom) Altitude of peak emission as a function Universal Time also from the BU airglow model. The solid line uses data measured by the ISR at the Jicamarca Radio Observatory. The dotted line uses IRI for values of electron density and plasma temperature.

The shorter timescale decreases in brightness, at 04:00 UT for example, are due to ESF depletions passing through zenith.

An airglow model developed at BU is used to obtain the absolute emission in rayleighs and height of the 6300 Å emission (*Semeter et al.*, 1996). The model uses electron density, electron temperature, ion temperature, O_2 density, N_2 density, O density, and neutral temperature profiles as inputs. The neutral inputs come from the NRLMSISE-00 Atmosphere Model (*Picone et al.*, 2002). The ionospheric inputs come from IRI-2012 (*Bilitza*, 2015) or from ISR data when available. For the night

of 3 April 2014, presented in Fig. 4.6, the ISR was running so we are able to run the model using radar data. Results from this model are shown in the middle panel of Fig. 4.6. The blue solid line is obtained when using ISR. We also show outputs using IRI-2012 (blue dashed line) to see how they compare. The bottom plot in Fig. 4.6 shows peak emission altitudes. The red dotted line indicates model results using inputs from IRI and the red solid line is the result using data from ISR. The ISR electron densities used in the model were shown in Fig. 4.3.

Early in the night, both model outputs show a trend that is similar to the measured brightness, although the IRI version has a greater emission. During this same time the IRI altitude of emission is lower than the ISR altitude of emission. The IRI model emission stays high later in the night while the measured and ISR version decrease. It is not surprising that the results using IRI-2012 are not as accurate as the ones using ISR because it is an empirical climatological model.

The overall trend of the modeled airglow using ISR data is very similar to the measured airglow emission, which means that it is mostly the variation in electron density that drives the changes in airglow emission. Additionally, the model using ISR data reproduces certain features such as the local maxima around 05:00 UT and the large depletion at 04:00 UT. There are some increases in brightness from the model result that are not seen in the measured airglow, such as the peak at 02:30 UT. From Figure 4.3 we see that this occurs in a region where there is a sharp gradient in electron density. The lower density region that is causing this gradient is a plasma depletion. Sharp gradients produced by ESF depletions can impact the ISR measurements and are an extra source of error during these times.

We use ISR density measurements to determine what is causing the airglow emission to vary. Early in the night the F-layer is very high in altitude with the peak density being higher than 500 km (Fig. 4.3),which causes weak 6300 Å emission. As

the night progresses the layer moves down and the brightness increases. The peak emission during the night occurs when the F-layer has moved down to low altitude but still has a similar peak density. After this the electron density decreases and the emission in the images and the models both decrease. Thus, it is clear that the electron density and its height is the major driver of airglow variation.

The measured airglow is much greater than the modeled airglow, even when accounting for up to 20% error in calibration. We use measured electron density from the ISR as an input so it is unlikely that electron density is the reason for the discrepancy. Since the BU airglow model also uses neutral density, it relies on the accuracy of NRLMSISE-00. One way to match the model to the observations is to increase O_2 by a factor of 3. While the neutral density may play some role in the discrepancy, we do not believe it is the main factor. We believe that scattered light from the surrounding area, Lima, is creating the excess airglow. We examined other cases and found that when fog and low clouds block the light from Lima, the measured results are closer to the modeled results. We did this same analysis using images from El Leoncito where there is minimal contamination from city lights and found that the model results were typically within the calibration error of 20% of the measured values. Although the measured airglow at Jicamarca may not be accurate in its absolute intensity, we identified depletions and measured their movement and morphology. The airglow model allows us to better determine the altitude of emission when measuring these characteristics.

4.2.3 Coherent scatter radar and ASI comparison

In addition to using the ISR for comparison of airglow brightness, we use the JULIA mode of the radar to compare the features visible in Fig. 4.4 with those in Fig. 4.5. In Fig. 4.5, the large scale, 10s of km, depletions associated with bottomside ESF are visible and the JULIA mode detects irregularities at scale sizes

of 3 m in any part of ESF that they occur. For this night we can directly observe that there are concurrent airglow depletions and small scale irregularities but recently *Rodrigues et al.* (2018) showed that airglow signatures can occur before post-midnight irregularities. In the ASI images from this night, depletions in the entire field of view are only visible after 04:00 UT (LT=UT-5) yet there are large plumes of irregularities visible in the RTI plots earlier. Although low emission early in the night leads to difficult observing conditions at zenith in the ASI images, sometimes features can be seen near the edge of the images away from the magnetic equator. The rising of the F-layer is most prominent at the center of the image, which is at the magnetic equator. At the edges of the image, the layer may not move up much. Additionally, the fountain effect that creates the crests of equatorial ionization anomaly (EIA) may be redistributing some of the plasma from the magnetic equator to the edge of the images. Both of these factors can lead to features being visible on the edge of the images early in the night when nothing is visible at the center. On this night, edge features are visible as early as 03:36 UT, as seen in Fig. 4.5, but the RTI shows irregularities starting prior to 01:00 UT. The airglow emission is too faint to observe the large-scale structures associated with the irregularities visible early in the night.

The rising of the F-layer that decreases airglow plays an important role in the generation of ESF. The formation of ESF is due to the generalized Rayleigh Taylor instability and the instability growth rate is shown in Equation 1.1. As the F-layer rises the growth rate of the generalized Rayleigh Taylor instability increases, mainly due to three terms in the growth rate equation. First, an upward plasma drift increases the growth rate. The other two terms are related to a decrease in background neutral density at higher altitudes. This lowers both the collision frequency and the recombination rate. A larger growth rate means that bottomside ESF is more likely to form. As a result, most ESF at Jicamarca occurs during post-sunset hours. Al-

though it is challenging to observe depletions associated with ESF early in the night with the ASI, irregularities associated with ESF are easily observed with coherent scatter radar using the JULIA mode. Using this mode the irregularities associated with ESF are observed before they are visible in the ASI.

4.3 The connection between large scale and small scale irregularities in ESF

4.3.1 Data and Methods

In this section I expand the comparison between coherent scatter radar and ASIs to investigate the connection between large-scale depletions and small-scale irregularities associated with ESF. I present observations of ESF over Jicamarca on the night of 20-21 August 2014 with the two radars and the ASI. We are able to observe ESF with irregularities at 0.3 m and 3 m scale sizes, using the radars, and at larger scale sizes by measuring airglow depletions. The work in this section was published in *Hickey et al.* (2015).

Conventional radar observations used to observe ESF have limitations since they only provide spatial information in range (or altitude). As the irregularities pass over the radar line-of-sight they are evolving, so it limits what can be determined and one must be careful of the slit-camera effect (*Hysell*, 1996). JULIA is a particular radar configuration used to detect coherent backscatter from plasma irregularities. One of its modes, the imaging mode, uses radar interferometry to resolve structures within the radar beam (*Hysell*, 1996; *Hysell and Chau*, 2006). This mode can help resolve some of the spatial and temporal ambiguity but it is limited to a small area on the sky of about 6°. The imaging mode data have been compared with plasma density data from the Communications Navigation Outage Forecast System (C/NOFS) and

the echoes seem to be correlated with depletions on the order of about 1 km (*Hysell et al.*, 2009).

Studies of ESF irregularities at sub-meter scale size are very scarce. *Tsunoda* (1980) used the ALTAIR radar operating in the 415 MHz mode, and TRADEX (1320 MHz), concurrently on 17 July 1979. The ALTAIR radar operated in continuous E-W scans and when irregularities were detected, the TRADEX radar was turned on. They found 11 cm irregularities at the same time as the 36 cm irregularities. The 11 cm irregularities are approaching the electron gyroradius and both irregularity scale sizes are below the oxygen gyroradius. *Tsunoda* (1980) claimed that these irregularities would most likely only exist in steep gradients in low-density plasma as discussed by *Huba and Ossakow* (1981b). At scales sizes less than 1 m, the lower-hybrid-drift instability may be responsible for the irregularities which is different from the process that creates irregularities at the meter scale and larger (*Huba and Ossakow*, 1981b). The gradient drift instability, where the plasma drift and plasma density gradients are antiparallel, has been proposed as the source of 3 m scale size irregularities on the western wall of large-scale depletions and in the center of the depletion (*Miller et al.*, 2010).

In 2014 an Advanced Modular Incoherent Scatter Radar (AMISR) was installed at the Jicamarca Radio Observatory. This system has only 14 panels (a full AMISR system has 128 panels). The smaller number of panels means that the system has less power and a smaller antenna aperture and cannot be used for incoherent scatter radar observations. The half power beam width of the AMISR-14 system is 8° in the E-W direction and 2° in the N-S direction. This system can be used for coherent backscatter from field-aligned plasma irregularities associated with ESF. AMISR-14 has an operating frequency of 445 MHz so the backscatter that is detected is from irregularities with scale sizes of 0.34 m, about an order of magnitude smaller than

those detected with the Jicamarca radar. One of the major advantages of an AMISR system is that it has an electronically steerable beam. This allows measurements at multiple positions on the sky almost simultaneously. This feature is useful for observing larger portions of the sky at once.

Rodrigues et al. (2015) presented the first results of ESF detection with AMISR-14 at Jicamarca. They were able to use the multiple beams of AMISR-14 to observe bottomside irregularities moving in the eastward direction with an average velocity of about 113 m/s, and covering over 200 km in zonal distance at times. The variation and decay of the echoes can be observed as they pass through the beams. During the same nights that the campaign was being run, the Jicamarca radar was also running in the JULIA mode. They concluded that both radars observed irregularities near the same time and altitudes, although some differences were detected and attributed to differences in the observational modes and hardware (e.g. antenna beam width, power, etc.).

4.3.2 Radar and Optical Diagnostics

Data from the JULIA imaging mode has been used to study ESF for many years now (*Hysell*, 2000) while the AMISR-14 system is relatively new and ESF has been reported only once (*Rodrigues et al.*, 2015). We start by looking at the data from the JULIA imaging mode on the night of 20-21 August, 2014. The right panel in Figure 4.7 shows the range-time-Doppler-intensity (RTDI) map of the JULIA observations made during pre-midnight hours of 20 August. The brightness of the backscatter shows the relative intensity of the observed echoes and the color represents the Doppler velocity of the irregularities producing the echoes. Red represents Doppler velocities away from the radar, blue represents velocities towards the radar, and green represents near zero velocities. Other colors represent a mixture of Doppler velocities. The left panel shows an example of the distribution of the irregularities

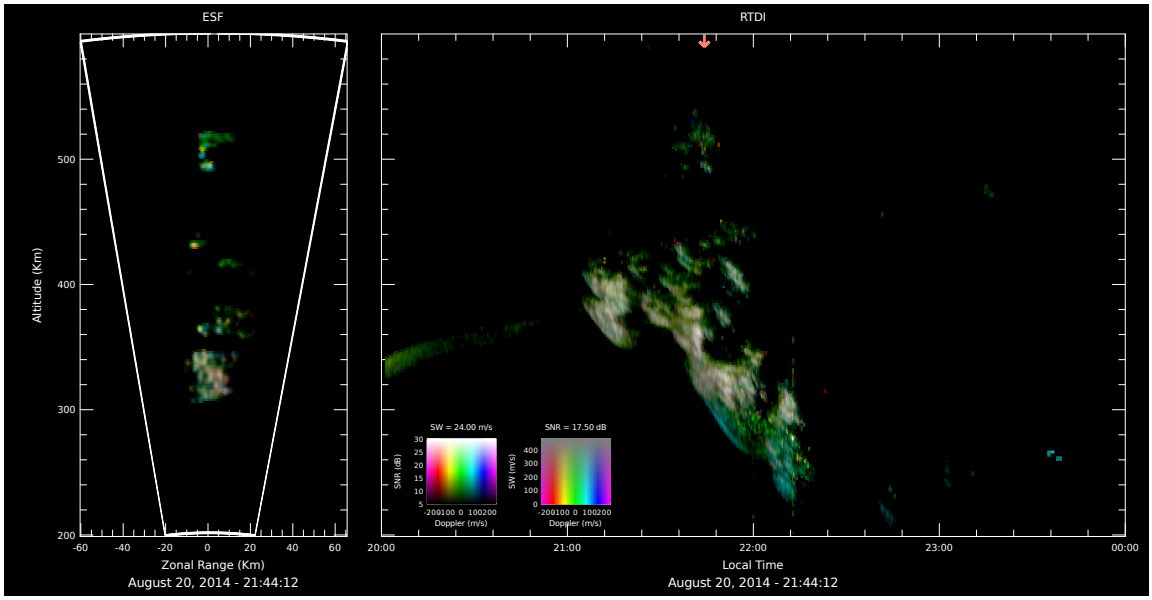

Fig. 4.7: A range-time-Doppler-intensity plot (right) from the Jicamarca radar in the JULIA imaging mode from the night of 20-21 August 2014. The brighter regions are higher signal to noise of the echoes. The brightness of the backscatter shows the relative intensity of the observed echoes and the color represents the Doppler velocity of the irregularities producing the echoes. Red represents Doppler velocities away from the radar, blue represents velocities towards the radar, and green represents near zero velocities. Other colors represent a mixture of Doppler velocities. The plot is a combination of the individual times, an example of which is shown on the left. The time on the left is 21:44 LT.

causing echoes within the radar beam obtained using interferometric imaging. This particular image corresponds to measurements made around 21:44 LT (local time is UT-5). While the JULIA imaging mode provides high angular resolution images of the irregularities, it can only provide information for a field of view of a few degrees off zenith. AMISR-14 complements and expands the interferometric imaging measurements by looking at different directions farther from the zenith. We determine where in the ASI images the AMISR-14 radar beams are located and then determine which part of the depletion the radar echoes are located. We discuss this technique further in the following paragraphs in the context of the AMISR-14 comparison.

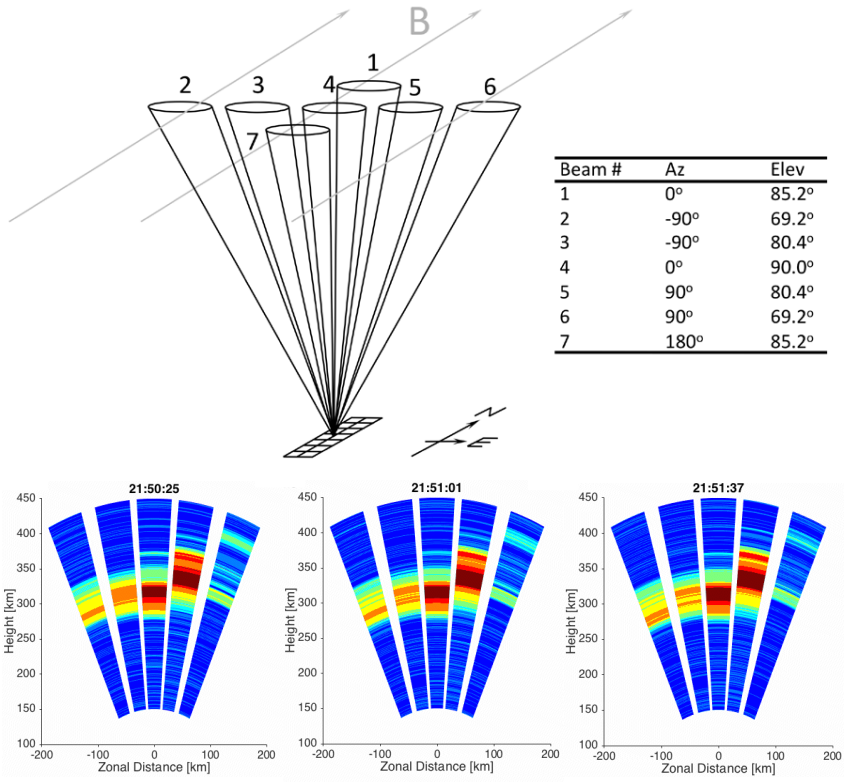

Fig. 4.8: The top diagram illustrates the beam directions used in the AMISR-14 experiment used in this study. The bottom panels show three AMISR-14 scans obtained with the multi-beam experiment. The colors represent the intensity of the echoes in dB. The color bar to the right indicates the signal to noise ratio of the echoes in dB. This is approximately the amount of data taken during one ASI image. There is not much variation between the three times.

The advantage of the AMISR-14 system is that it is electronically steerable so that it can look at multiple locations on the sky with the capability of switching pointing directions from pulse to pulse. With this technique we can compare the radar data with multiple places in the ASI images and observe how the small-scale irregularities change as they move from beam to beam. This experiment used seven different look directions, five of which were perpendicular to the magnetic field in order to observe the field-aligned irregularities. The beam configuration is shown in the top panel in Figure 4.8. Beams 2 through 6 are the beams that are perpendicular

to the magnetic field and are the only ones used in this study. This experiment used 28-bit coded pulses with a baud length of 10 μs and an inter-pulse period of 4 ms. 128 pulses were transmitted in each pointing direction before switching and 1280 pulses, in each direction, were integrated to obtain an AMISR-14 image. This means that we have an integration time of 36 seconds for the seven beams.

We use the AMISR-14 and ASI to compare backscatter from small-scale structures to the large-scale depletions. We determine where in the large-scale structures the small-scale irregularities are appearing. The 6300 Å images are taken about every eight minutes with an exposure time of 120 seconds and since the AMISR-14 integration time is about 36 seconds there are about four radar measurements during one image. To compare between the two datasets, we choose the AMISR-14 data that is closest to the center of the exposure time from the imager. The backscatter from irregularities in the AMISR-14 data barely changes in the exposure time of the image. Three consecutive time steps are shown in at the bottom of Figure 4.8. There are some cases where irregularities are only present in one beam. As the irregularities pass over the radar and through the beams, they tend to occupy one beam for about five minutes. Figure 4.9 shows the entire night of data from the zenith beam in the same format as Figure 4.7. Two types of ESF structures are observed in the measurements presented in Figure 4.7 and Figure 4.9. The first type, observed before 21:00 LT, is bottom-type ESF and is seen very often in radar preceding the detection of large-scale ESF events; it is not associated with Rayleigh-Taylor density perturbations. It is, instead, the result of interchange of plasma instabilities (wind-driven gradient drift) occurring on horizontal electron density gradients occurring around sunset. The echoes are caused by weak plasma turbulence associated with small background density perturbations. GHz scintillation, for instance, would be negligible during that type of ESF.

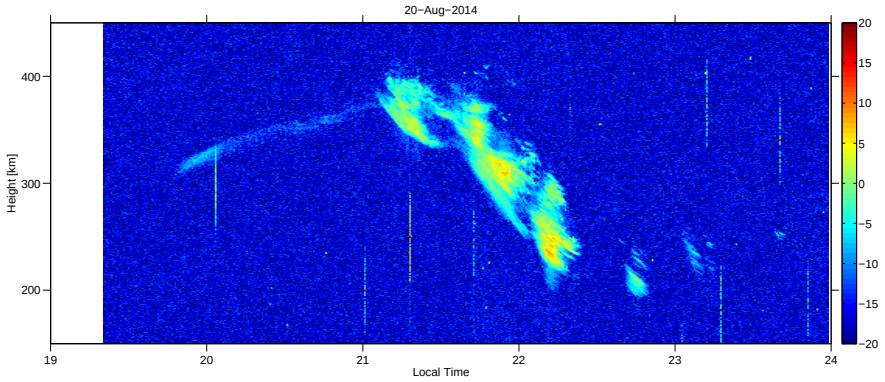

Fig. 4.9: A range-time-intensity (RTI) map for the beam 4 (zenith) observations made by AMISR-14 on the night of 20-21 August 2014. The color bar to the right indicates the signal to noise ratio (SNR) of the echoes in dB. The vertical streaks seen throughout the night are from satellite echoes and are not related to the properties of the atmosphere.

After 21:00 LT, we observe the passing of a bottomside ESF structure, which are irregularities associated with an under-developed plume/depletion, which was presumably created by the Rayleigh-Taylor instability process. The irregularities are in a more turbulent state and cause stronger radar echoes. The detection of bottom-type, bottomside and topside ESF radar structures with AMISR-14 are discussed in *Rodrigues et al.* (2015). A description, in more depth, of these structures is given by *Woodman and La Hoz* (1976) and *Hysell and Burcham* (2002). We still seek a better understanding of the conditions and plasma instabilities causing these ESF structures, but recent improvements have been made (*Aveiro and Hysell*, 2010).

Overall, similar behavior of the irregularities in the two radars is observed although there are a few differences. At some altitudes, features persist for longer in the AMISR-14 data than they persist in the JULIA data. For example, between 21:00 and 21:30 LT, we see echoes for a longer time in the AMISR-14 data compared with the JULIA data. We attribute this to differences in the sensitivity of the two systems. While AMISR-14 can still observe 0.3 m irregularities, the power-aperture of the JULIA mode was not enough to detect, clearly, echoes from the 3 m irregu-

larities. At other times the JULIA mode detects features that are not detected by AMISR-14. This can be seen when looking at altitudes higher than 400 km. The JULIA data shows echoes above 400 km but none are seen in the AMISR-14.

We next show an ASI image from this night at 23:00 LT in Figure 4.10 (left). We assume an emission height of 250 km. It is possible to resolve depletions as small as about 10 km but most are around 100 km in width. Small-scale structures have been observed to occur at the same time as the large-scale structures (*Miller et al.*, 2010; *Otsuka et al.*, 2004) but the connection is not fully understood.

The contrast in the images can make it difficult to see the depletions so we take a zonal cut through the center of the image and plot pixel value as a function of distance from the center of the image. Seven pixels in the meridional direction are averaged to create the cut. There are 136 pixels for each degree of latitude. Figure 4.11 shows ten zonal cuts from 21:49 LT to 23:00 LT, which are the times that we are focused on in this study. We start at 21:49 because the airglow is too dim early in the night due to the F peak being too high in altitude. At 23:00 LT, six depletions are clearly visible, compared to earlier in the night when only one or two are visible. A depletion has been marked as depletion "A" and can be tracked all the way back to 21:57 LT. The depletions are moving at approximately 100 m/s, consistent with the movement of the irregularities from *Rodrigues et al.* (2015). The Milky Way can be seen in Figure 4.11 as an increase in brightness that is much smaller in zonal width than the depletions. At 21:49 it is at a zonal distance of about -70 km and moves west as the night goes on ending up at about -250 km.

4.3.3 Comparing AMISR with the ASI

Once unwarped images are produced the radar data can be compared with the ASI data. We present data from 22:13 LT on 20 August 2014 in Figure 4.12 to demonstrate how we perform the comparison. Figure 4.12a shows an unwarped all-

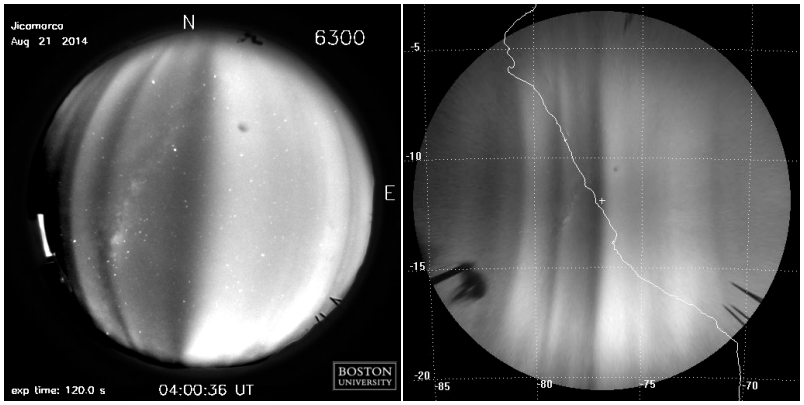

Fig. 4.10: A raw image at 23:00 LT (4:00 UT) from the Jicamarca ASI on the left. The exposure time is 120 seconds and the image was obtained using a 6300 Å filter. On the right is the result of unwarping the image. The western coast of South America is seen as a white line and the location of the ASI is a small white cross.

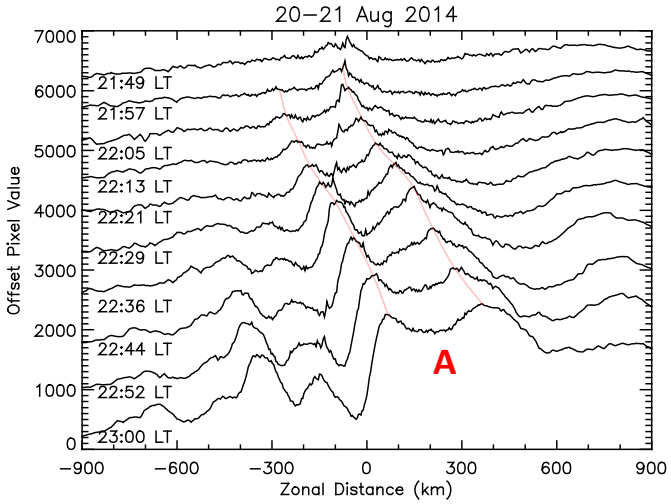

Fig. 4.11: Pixel value for zonal cuts for all the images from 21:49 LT to 23:00 LT. The pixel value is arbitrary as each time is offset from the others to make it easier to see. The cuts are 7 pixel meridional averages and corresponds to the meridional beam width. The movement of the depletions across the field can easily be seen. The depletion marked as A, between ∼100-300 km east at 23:00 LT, is the one we mostly focus on. The red lines follow the west and east edges of the depletion.

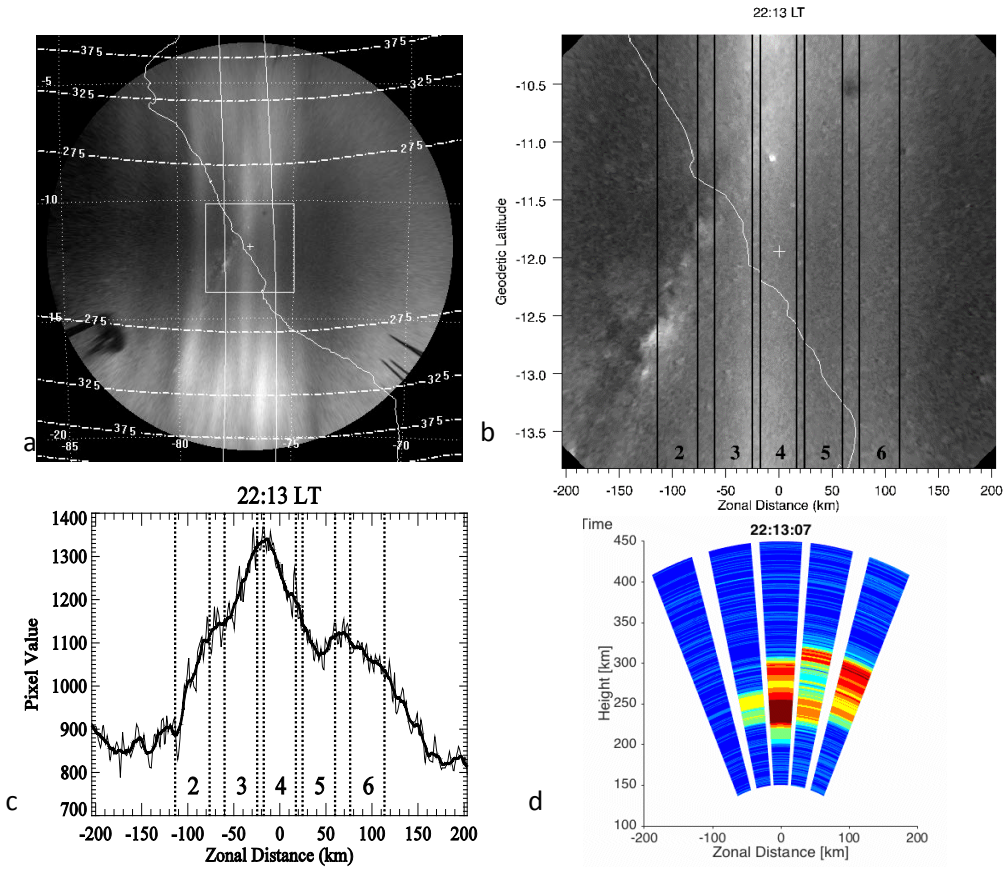

Fig. 4.12: (a) An unwarped image at 22:13 LT. Dashed lines showing the apex altitude of the magnetic field. Magnetic longitudes correspond to the edge of the field of view of AMISR-14 are shown as vertical white lines. (b) The area within the box in (a) with zonal distance away from the ASI as the x-axis and geographic latitude as the y-axis. The positions of the AMISR-14 beams are shown, although in reality they do not cover the full N-S extent shown. (c) A zonal cut through the center showing pixel value as a function of distance. The AMISR-14 beams are also marked here. The lighter line is a 7 pixel meridional average and the darker line is a 15 pixel running average. Beam 2 is on the eastern wall of depletion "A". (d) Data from AMISR-14 with the color showing SNR in dB.

sky image with a box in the middle representing the area of the zoomed-in region that is visible in Figure 4.12b. The western coast of South America is seen as a white line. The white cross in the center shows the position of the ASI and radar, which is located at -0.1°geomagnetic latitude. The two N-S white lines indicate the coverage of the 5 perpendicular to B AMISR-14 beams. They extend North and South to show how

they map along magnetic field lines. Airglow structures occurring away from zenith, to the north or south, can be mapped to apex heights (i.e., height above the magnetic equator) higher than 250 km. The dashed lines indicate 275, 325, and 375 km apex heights for field lines reaching 250 km off the equator. An apex altitude of 275 km is at a magnetic latitude of $\pm 3.5°$and an apex height of 375 km is at a magnetic latitude of $\pm 7.8°$. The relatively bright airglow regions represent background plasma density and the darker regions are depleted regions or airglow depletions where there is less plasma. The transition between dark and bright regions, where the plasma density changes, is what we call the walls of the depletions. The western wall of the depletion is, moving east, the transition from high plasma density to low plasma density and the eastern wall is the transition from low to high density. Different regions of the image are placed into one of four categories: the western wall, the center of the depletion, the eastern wall, and the bright background. If the beam includes parts of both walls it is categorized as either the center of the depletion or the bright background, even if one wall is more represented with the beam width. The depletions are N-S aligned and in general cover the entire field of view.

In Figure 4.12b we show the zoomed-in box from Figure 4.12a that covers a zenith angle of 50°. The locations of the AMISR-14 beams are shown in the image. This can be compared directly with the AMISR-14 data shown in Figure 4.12d. In the N-S direction the beam only covers 2°(8.75 km, 7 pixels). The cross in the center shows the location of the Jicamarca radar. Geodetic latitude is marked as is the W-E zonal distance. The image size was chosen to match the radar data. In this image we can see a bright area near the center and the darker depletions are on either side. The Milky Way can also be seen in the image and is distinguished from the depletions by its orientation, size, and the direction of movement.

In order to make the comparison between the imager and the radar we have to make sure that our image is unwarped at an accurate altitude. The emission mostly comes from a region that is about 50 km in altitude extent and is typically centered around 250 km. The height of emission does vary through the night. We have looked at how different altitudes could change the results and varying them by ∼50 km (a typical height variation in nighttime 6300 Å airglow) does not significantly affect the result. The dark and bright zones are still in the same beams.

As was done with Figure 4.11, we take a zonal cut at zenith, averaging over 7 pixels north and south. This is plotted as pixel value versus zonal distance in Figure 4.12c. We also do a running average in the zonal direction of 15 pixels to help see the larger features better. The running average is the smoother curve plotted over the noisier curve.

4.3.4 Results

We compare data from AMISR-14 with images from the ASI to determine where in the large-scale depletions the small-scale echoes are occurring. We refer to Figure 4.12 to demonstrate what the comparison looks like. In this example, at 22:13 LT, we see that beam 2 shows no echoes and the region corresponds to the eastern wall of the airglow depletion marked as "A" in Figure 4.11. In beam 3 AMISR-14 detects irregularities, still on the eastern wall. Beam 4 is on the western wall of a different depletion and echoes from AMISR-14 are also present. Beam 5 encompasses a small depletion that includes both western and eastern wall gradients and we see echoes in AMISR-14. Beam 6 is on the western wall of yet another depletion and again strong echoes are seen with AMISR-14.

Figure 4.13 shows the comparison for a later time, now at 22:29 LT. Here we can see that depletion "A," that was to west of beam 2, has now moved into beam 3. This depletion is approximately 200 km in width, showing the size of these large-scale

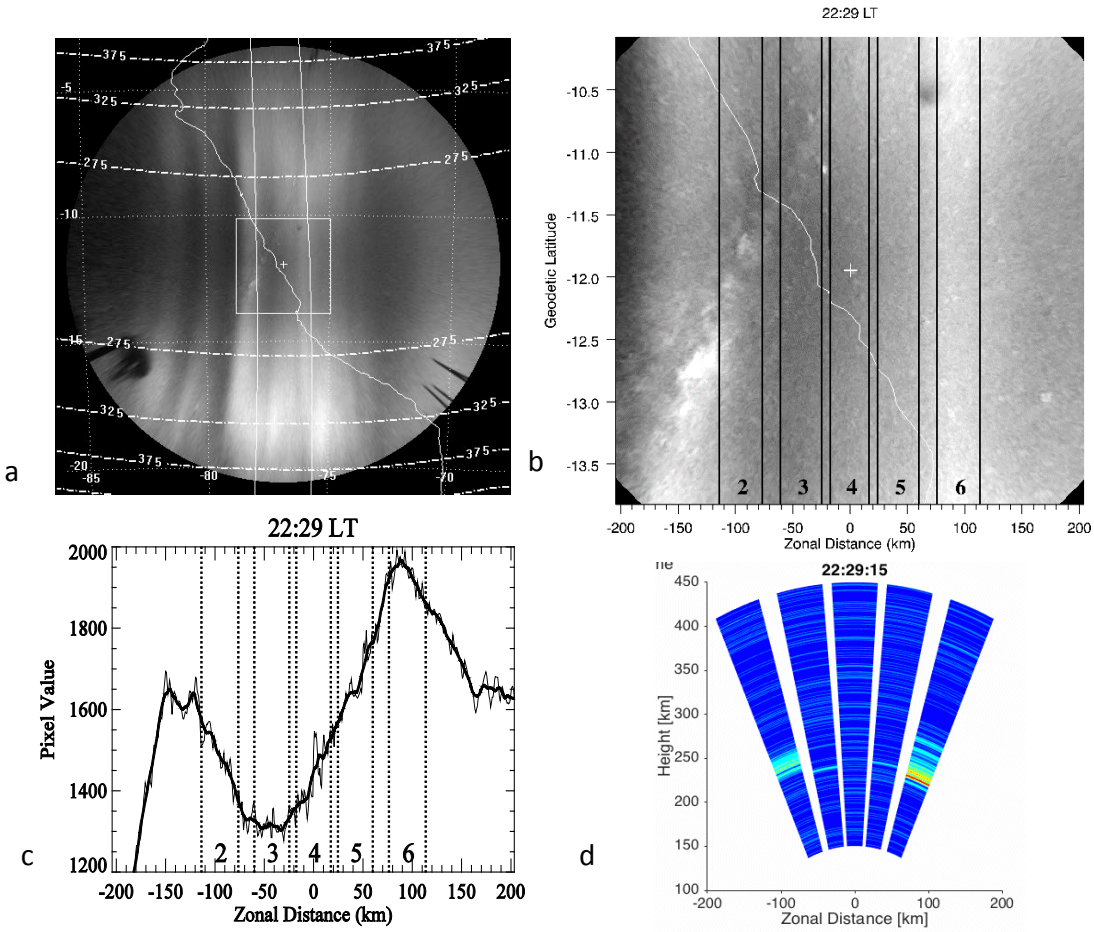

Fig. 4.13: Same as Figure 4.12 but for a later time. Beam 3 is sampling the center of depletion "A".

structures. Beams 2 and 6 are the only ones that detect significant echoes. Beam 2 is on the western wall of depletion "A" and beam 6 encompasses a part of the bright background and a western wall and is categorized as the bright background. The center of the depleted region and the eastern wall does not show any significant echoes.

We counted all the times where we do and do not see echoes at zenith from 21:49 UT to 22:52 LT that corresponds to the times when AMISR-14 detected echoes in the 225-275 km range. We choose a 50 km range because that is approximately

Table 4.1: Cases at 250km Where Radar Echoes Were Found in Each Part of the Depletion

Echoes 250 km	Western Wall	Eastern Wall	Background	Depletion Center
Yes	13	5	4	5
No	0	11	0	2

the altitude extent of the airglow layer. If there are echoes higher up, they are not considered and are analyzed later. Table 4.1 shows these results. If there are echoes that have an SNR greater than -5 dB, this situation is marked as yes. If there are no echoes in the beam this is marked as a no. For each image we look at whether the beam encompasses an eastern wall, a western wall, the background plasma or the depletion center.

We see scatter in 13 beams that correspond to the western wall, such that about 48% of cases occur here. There are no instances when we observe the western wall and do not see scatter. We see scatter in 5 beams that corresponds to the eastern wall, which is about 19%. We found that 11 beams show no scatter on an eastern wall. We also see scatter in 4 cases where there is a bright peak, which represents the background plasma. As can be seen in the zonal cuts, the background plasma peak is smaller in width than the AMISR-14 beam so these areas contain gradients as well. There are no instances when we observe a bright peak and no scatter. We see scatter in 5 cases where the beam is in the depletion center, which also often contains gradients, and 2 cases where there is no scatter and the beam is in the depletion center.

Another way of analyzing this data is to determine how frequently each section of a depletion has radar scatter relative to the amount of times that part of the depletion is in a beam. This is found by taking the number of times radar scatter is observed for a certain part of the depletion and dividing it by the number of times that section is in a radar beam. Scatter is detected in the western wall 100% of

the time and in the eastern wall it is about 31%. Scatter is detected on the bright background 100% of the time and in the depletion center it is about 71%. The bright background and depletion center always contain parts of both walls which must be taken into account when interpreting the results. From this information we can conclude that scatter comes from all regions of the depletion but it is more likely to occur in the western wall. The scatter from the western wall is most likely due to the gradient drift instability (*Sekar et al.*, 2007; *Miller et al.*, 2010) because the density gradient and drift direction are antiparallel on this wall. In contrast, the scatter that is found on the eastern wall seems to be due to a different process since the gradient and drift direction are not antiparallel which is also supported by the difference in the occurrence rates.

Large-scale depletions observed by the ASI allow us to compare them with echoes that are observed from altitudes $>$ 250 km. Structures north and south of zenith tell us information about radar echoes at the apex heights marked in Figures 4.12 and 4.13.

We did a similar analysis for cases when echoes were observed between 275 and 325 km (corresponding to magnetic latitudes of $\sim$3.5-6°in the ASI FOV) and between 325 and 375 km (corresponding to magnetic latitudes of $\sim$6-8°). 50 km ranges were chosen because the airglow layer is approximately 50 km in altitude extent. The airglow structures seem to show a slight N-S asymmetry with respect to the magnetic longitudes so we separate these two results. As mentioned before, in the analysis between 225 and 275 km, if echoes were present above 275 km, they were not included. Now these results, as well as those with echoes from 325-375 km, are included in this analysis.

In Table 4.2 we show the combined results from 275-325 km and 325-375 km. Results from the north and south show the same general trend that more echoes

Table 4.2: Radar Echoes Detected in Each Part of the Depletion for Altitudes Above 250km

	Echoes	Western Wall	Eastern Wall	Background	Depletion Center
South	Yes	37	24	6	8
	No	6	10	7	3
North	Yes	31	23	11	9
	No	6	12	4	4

come from the western wall than from anywhere else. If we combine the north and south results we find that about 46% of the scatter is on the western wall and about 32% of the scatter is on the eastern wall. The background and depletion centers do not represent 'flat' structures but still include gradients from both the western and eastern wall and about 23% of the scatter is seen in those as well.

We also compute the percentage of how frequently each region of the depletion has radar scatter for this two altitude ranges, as we did for 225-275 km. We find that radar scatter occurs on the western wall about 85% of the time and occurs on the eastern wall about 68% of the time. The bright background has scatter about 61% of the time and the depletion center has radar scatter about 71% of the time.

The percentages for total number of occurrences are very similar to the results from 225-275 km. The percentages for chance of occurrence vary a bit when compared with the lower altitudes. The western wall still shows a high frequency of occurrence even though it is no longer 100%. The eastern wall now shows a much higher frequency. The depletion center shows about the same frequency as the lower altitudes and the bright background is still high even though it is no longer 100%. The differences between the higher altitudes and lower altitude could be attributed to the fact that we are dealing with small numbers at 225-275 km so it does not take much to vary the percentage.

We have to assume that the features map perfectly along field lines to do this analysis and this assumption also introduces some error as well. If the depletions

mapped perfectly along the magnetic field lines then the magnetic field line with a foot point in the center of a depletion in the southern half of the image would have another foot point in the center of the depletion in the northern half. When we compare the location of these foot points to the north and to the south we find that the depletions to the south are often located to the west of the foot point that maps to the center of the depletion to the north. An inverted "C" structure is expected of these depletions due to the wind shear in the plasma flow that peaks near the F peak (*Kelley et al.*, 2003) but the "C" should be symmetric about the magnetic equator. The asymmetry could be due altitude and latitude gradients in the background winds. Even though the features north of zenith do not map to the exact same location at the magnetic equator as the ones south of zenith we still find the same result that echoes come from everywhere in the depletion but the western wall is favored. Overall, the results from Table 4.1 and Table 4.2 show that the most echo detections occur on the western wall.

The same comparison is done with the JULIA imaging mode but this radar is only able to point in one direction so we are only able to look at one part of the ASI image instead of five. This decreases the amount of comparisons that can be done. Early in the night the ESF echoes occur between 300 and 400 km, which is higher than the 6300 Å emission at 250 km, and the echoes do not last very long after they appear at this altitude. From the images during this time we find three cases when echoes appear on the western wall of the depletion. We do not find any cases where the echoes occur in the center of the depletion, the eastern wall, or the background. We do not compare the higher altitude JULIA imaging data with the parts of the ASI images that map to higher altitudes because the beam width is much smaller with this mode than with AMISR-14 so any errors in the mapping along field lines would be amplified. Although results are not conclusive due to the limited number

of observations we see the same preference for echoes to occur at the western wall, like the AMISR-14 comparison.

In addition to the comparisons shown above we can also track irregularities across the beams very accurately to see how their evolution relates to the motion of the airglow depletions. We show in Figure 4.14 an example of this from 22:29 LT to 22:44 LT. Arrows indicate the echoes and the parts of the image they correspond to. We can clearly see that in all three images the echoes are on the western wall of depletion "A" as it moves through the field of view. The earliest time in Figure 4.14 also shows that the western wall of another depletion to the east also contains irregularities. The motion of the western wall is correlated with the motion of the irregularities. The most intense echoes are on the western wall, weak echoes sometimes appear in the center of the depletion, and no echoes are on the eastern wall. We are not able to track echoes on the eastern wall in the same way at different times because when echoes appear on the eastern wall they tend to also be occurring in all of the beams.

Our results show that more echoes are found on the western wall of the large-scale airglow depletions. On the western wall of the depletion the plasma density gradient is anti-parallel to the nighttime neutral wind which is the condition for the gradient drift instability, discussed in further detail in Section 1.4.2. This instability has been proposed as the source of irregularities on the western wall (*Miller et al.*, 2010). *Otsuka et al.* (2004) proposed that the low-frequency drift instability is responsible for the small-scale echoes they observed since the most intense echoes observed in their study occurred in the center of the depletions. *Miller et al.* (2010) discussed that the echoes in the center may be driven by or propagating from the echoes that occur on the western wall due to the gradient drift instability. They also

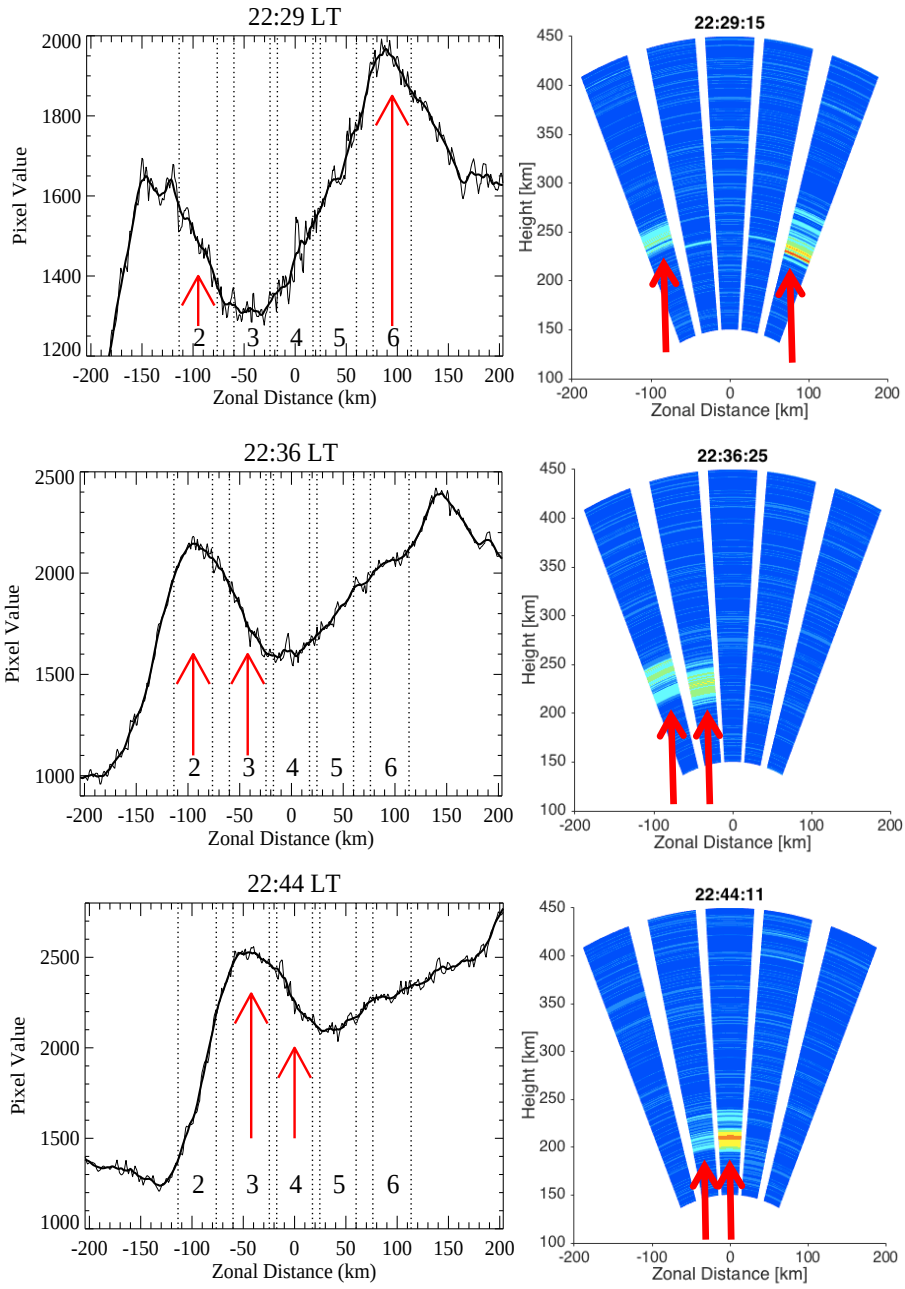

Fig. 4.14: On the left are zonal cuts, as described in previous figures, for three consecutive images from 22:29 LT to 22:44 LT. Red arrows indicate where the echoes are occurring. The echoes in this example are only coming from the western wall of depletion "A".

observed that only the high altitude echoes (h > ∼400 km) were mainly coming from the central part of the depletions.

The AMISR-14 irregularities are sub-meter in size, which means that it is likely that the lower-hybrid-drift instability, discussed in Section 1.4.2, in is involved as well and is contributing to the echoes. There are certain conditions for this instability to exist as outlined in *Huba and Ossakow* (1981b). Specifically, this can occur at 0.34 m with gradient scale lengths smaller than ∼50 m, for a neutral density of 10^{15} m^{-3}, and electron density of 10^{10} m^{-3}. Results from the ionosonde at Jicamarca show that the background electron density is about 10^{10} m^{-3}. Using NRLMSISE-00 (*Picone et al.*, 2002) we find that the neutral density should be around 10^{14}-10^{15} m^{-3}. This means that with relatively sharp density gradients, which we expect to exist in these depletions, the lower-hybrid-drift instability is likely to be occurring.

The results presented here do not seem to agree with results from *Otsuka et al.* (2004) and partially agree with those from *Miller et al.* (2010). In these previous studies, ASIs and radars were not located at the magnetic equator. Thus they were sampling depletions at higher altitudes, most likely associated with topside plumes, whereas we are observing only bottomside ESF. The different conditions present for topside plumes compared with bottomside ESF could explain the difference in the location of the echoes. AMISR-14 is probing sub-meter scale sizes and the previous studies were looking at ∼3 m scale sizes. The lower-hybrid-drift instability cannot produce 3 m scale irregularities (*Huba and Ossakow*, 1979), which can explain why our results are different.

4.3.5 Summary

We have compared ASI observations with AMISR-14 measurements in an attempt to better understand the relative localization of large-scale (10-100s km) equatorial spread F depletions and small-scale irregularities. Overall we find that echoes

occur preferentially on the western wall of the depletion over all other parts. This is supported by the comparisons between the 250 km AMISR-14 data and zenith of the ASI, between higher altitude AMISR-14 data and off zenith ASI depletions, and between JULIA imaging data and zenith of the ASI.

We find that when comparing the zenith measurements of the ASI with 250 km echoes from AMISR-14, approximately 48% of the echoes occur in the western wall of depletions, 19% on the eastern wall, and the other 33% occurs in the background and depletion center. Looking at how often echoes were detected in each part of the depletion we find that 100% of the time echoes are detected on the western wall and 31% of the time they are detected on the eastern wall. We extend this comparison to look at the airglow north and south of zenith that correspond to apex heights at the magnetic equator of 300 km and 350 km. We combined the data from the north with zenith and south with zenith and found these similar results: 46% of scatter is on the western wall, 32% on the eastern wall, and 23% in the bright and dark regions. We find that 85% of the time echoes are detected on the western wall and 68% of the time on the eastern wall.

We have found that there is a higher occurrence of echoes coming from regions identified as the western wall of large-scale depletions in comparison with echoes coming from other regions of the depletion. Our results suggest that the gradient drift instability is responsible for the echoes on the western wall at 0.34 m and 3 m and that the lower-hybrid drift instability is responsible for the echoes on the eastern wall at 0.34 m and may also contribute to the echoes on the western wall. The lower-hybrid-drift instability is not capable of producing instabilities at 3 m. Our results only include observations of bottomside ESF and do not show the same trends observed in previous studies of topside ESF using ASI and radar data. The previous studies analyzed 3 m scale size irregularities. We only find a difference between

our results from AMISR-14 and previous studies. Our JULIA results are consistent with previous results. We attribute the differences to the fact that we are observing sub-meter scale irregularities produced by the lower-hybrid-drift instability.

We have also shown that during one part of the night we are able to track the echoes occurring on a western wall as they pass through multiple beams and during this time it is only the western wall that is producing echoes.

4.4 Large Scale Wave Influence on ESF

Like the connection between large-scale and small scale ESF structures, the seeding mechanism for ESF is another active area of study. One way to investigate this is measure characteristics of large-scale bottomside ESF structures. ASI images that contain multiple airglow depletions associated with ESF can be analyzed to characterize their spatial morphology. We measure the distance between depletions and between groups of depletions to investigate the presence of large scale wave structures (LSWS). This work has been published in *Hickey et al.* (2018). A study by *Tsunoda and White* (1981) showed that a 400 km large scale wave structure (LSWS) modulated the production of ESF. They used coherent radar scans and found that ESF plumes formed at the crests of a LSWS. Since then, other studies have also found a connection between LSWS and the formation of ESF (*Huang and Kelley*, 1996; *Narayanan et al.*, 2012; *Patra et al.*, 2013; *Joshi*, 2016). Additionally, the distance between plasma depletions associated with ESF has been measured during solar minimum using imagers in Chile (*Makela et al.*, 2010), Christmas Island, and Brazil (*Chapagain et al.*, 2011). They both measured the spacing between adjacent plasma depletions and found that the structures were typically separated by 100-300 km. The observations from *Makela et al.* (2010) were interpreted as being the result of gravity waves but they do not discuss the role of a LSWS.

ESF depletions are visible at Jicamarca during most of the clear nights. Out of 517 nights of observations, 387 nights were too cloudy to make a conclusion about the presence of ESF. Out of the remaining 130 clear nights, depletions were observed in 120. Only 10 nights did not show structures at Jicamarca. The identification of airglow depletions associated with ESF is relatively straightforward as they are bands of lower intensity that extend from north to south. It is possible that undulations in the bottomside could create similar airglow structuring but in general we are able distinguish between ESF related structures and other perturbations. Depletions associated with ESF tend to travel eastward and have a well defined band structure that curves to the west away from zenith at Jicamarca. We do not expect other undulations to move in the same way and have the same extent and shape in the field of view. Precursors to post-midnight ESF as described in *Rodrigues et al.* (2018) show airglow structures that are not associated with ESF and are likely due to LSWS. ESF structures tend to move with regular motion eastward and the precursors in *Rodrigues et al.* (2018) had very little motion, often staying in the same location for multiple images. In the analysis here the structures are observed over multiple images and we wait until the structures are fully formed to measure their properties so we do not think that ESF precursors are impacting our analysis. From our observations, depletions occur just after sunset and in some cases just before sunrise. In almost all cases the depletions tend to come in groups. We measured the smaller distance between the depletions within the groups and measured the distance between the groups. The distance between depletions was taken to be the distance from the center of one depletion to another. To determine the distance between groups, we locate the center of a group and measure the distance to the next group. The center of the group is the midpoint between the outer most depletions. An example of the grouping is shown in Fig.4.15. In this example, there are two groups of depletions

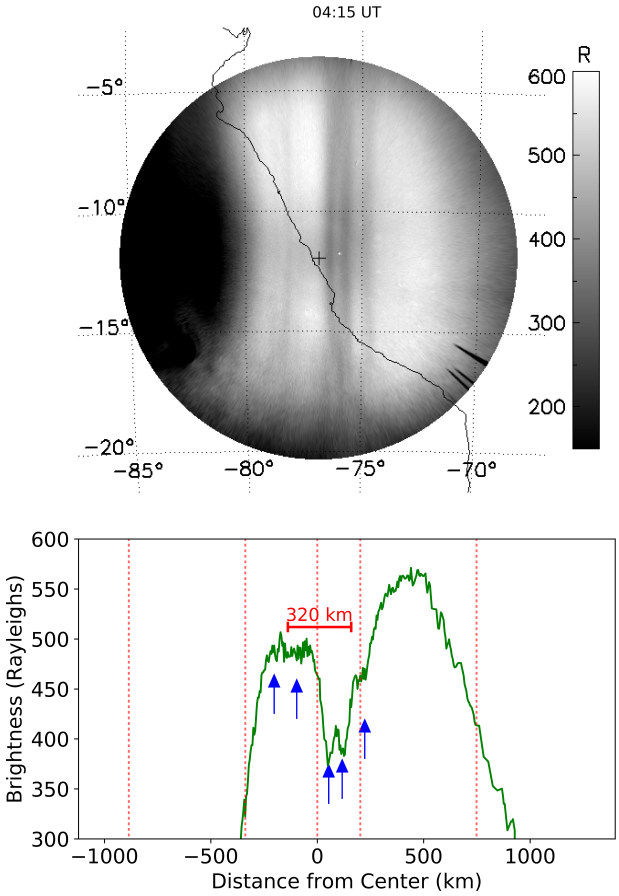

Fig. 4.15: An example from 3 April 2014 of how depletion separation is measured. On top is an unwarped ASI image with two groups of depletions visible. On bottom is a cut through the image at zenith. The red dotted lines show the four lines of longitude from the image and the center of the image where the ASI is located. The blue arrows show the locations of the depletions. The distance between the depletion groups is shown in red at the top of the image.

with a group to group separation of 320 km. The distance between the depletions, marked by blue arrows, in this example ranges from 50 to 110 km. Analysis of all the nights in our sample showed that typically there were multiple depleted structures in close groups of 2 to 4 separated by 50-100 km. The group to group separation was typically between 400 and 500 km. Consecutive depletions that were closer than 300 km were considered to be in the same group. We found no seasonal variation in the separation distance, number of depletions in the groups, or grouping distance.

Previous studies using ASIs that measured the distance between depletions did not measure nor discuss any group distances. They found that the structures were typically separated by 100-300 km. Therefore, our analysis of the Jicamarca ASI images is the first of its kind. Another difference between these results and the previous studies is that our observations are during solar maximum (F10.7 $\approx$ 100-150) while the other studies were done during two different solar minimums. The observations in *Makela et al.* (2010) were taken from 2006 to 2009 (F10.7 $\approx$ 70) and the *Chapagain et al.* (2011) observations were done in 1995 (F10.7 $\approx$ 80) .

The separation of the groupings in our observations indicates that a LSWS on the order of 400-500 km may be modulating the formation of ESF depletions, causing them to appear in groups. This is consistent with the study from *Tsunoda and White* (1981) where it was noted that ESF plumes were forming at the crest of LSWS where the F-layer had moved up. The rising of the F-layer around sunset, due to the pre-reversal enhancement, is understood to play an important role in the formation of ESF. It has also been shown that even a small rise later in the night can increase the likelihood of ESF (*Ajith et al.*, 2016). A LSWS could provide the small rise, creating the groups of depletions.

Occasionally separations much larger than 500 km (e.g. 1000 km or more) were observed. For these cases it seems more likely that something other than an LSWS is causing this modulation. It is possible that other dynamics are causing the F-layer to rise or there is some other variation affecting the growth rate. It is interesting to note that we are only observing bottomside structures in this study and for most case we are not able to determine if they are forming topside plumes. *Tsunoda and White* (1981) looked at the modulation of plumes that formed from bottomside ESF. Our results indicate that these waves not only modulate the creation of topside plumes but also modulate the bottomside structures that do not form plumes.

4.5 Using ESF observations and FPI measurements to compare neutral winds and plasma drifts

In addition to using airglow depletions to study ESF, they can also be used to measure characteristics of the background ionosphere. The zonal motion of the depletions across the field of view of the ASI are used to investigate the zonal plasma drifts at the magnetic equator. This work has been published in *Hickey et al.* (2018). At night the zonal plasma drifts are driven mostly by the neutral winds through the F-region dynamo (*Rishbeth*, 1971). Equation 4.1 (*Martinis et al.*, 2003) shows the different quantities that determine the zonal drift velocity.

$$V_\phi = U_\phi^P - \frac{\Sigma_H}{\Sigma_P} V_L - \frac{J_L}{\Sigma_P} \tag{4.1}$$

V_ϕ and V_L are the zonal and vertical plasma drifts, U_ϕ^P is the Pedersen-weighted neutral zonal wind, J_L is the integrated vertical current density, and Σ_P and Σ_H are the field-line integrated Pedersen and Hall conductivities. The plasma drift, V_ϕ, is typically equal to U_ϕ^P meaning that the F-region dynamo drives the plasma motion. The other terms make minor adjustments to V_ϕ.

We measure the neutral winds with an FPI and the plasma drifts inferred from the depletion motion to make a comparison. There are various ways to determine plasma motion from ASI images (*Chapagain et al.*, 2013; *Makela and Kelley*, 2003) but here we track a depletion through a series of images and from that we determine a zonal drift. We present a case study from 3 April 2014 where we have about three hours of concurrent measurements from the FPI and ASI at the Jicamarca Radio Observatory. We determine the location of the minimum of the depletion and track it as it moves through the field of view. Figure 4.16 shows the comparison between the zonal plasma drifts derived from the ASI and the zonal winds measured by the FPI.

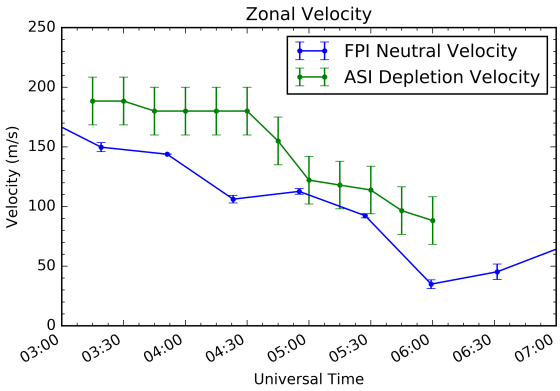

Fig. 4.16: Zonal neutral winds (blue) and zonal plasma drifts (green) on 3 April 2014 at Jicamarca. Zonal wind speeds are determined by an FPI and plasma drifts are determined from ASI depletion velocities. The ASI images were all unwarped at an 250 km altitude

The plasma drifts show a similar trend as the FPI neutral winds with an overall reduction in magnitude after 03:00 UT. The velocity of the depletions is higher than the velocity of the neutrals, meaning that the F-region dynamo is not fully operating. We consider potential errors in the determination of the depletion velocities that could affect the absolute magnitude of the drifts. Images were unwarped assuming an altitude of 250 km. A 50 km difference would modify the zonal drift calculation by ~15 %. From Fig. 4.6 the calculated height is greater than 250 km from 03:00 to 04:00 UT, so the drifts would be larger than the ones shown in Fig. 4.16. At 04:00 UT the modeled altitude of emission is most likely lower than reality because of a depletion that causes the electron density in the ISR data to be lower than the background. After 04:00 UT the height is closer to 250 km, but is slightly lower. Thus, we may be underestimating the zonal plasma velocity early in the night and over estimating it later in the night. In addition to error from the uncertainty in altitude there is also associated error with determining the center of the depletion and with the fact that depletions tend to evolve as they pass through the field of view. These errors have been accounted for in the error bars in Fig. 4.16.

Chapagain et al. (2013) did a comprehensive study in Brazil comparing depletion velocities to neutral winds from FPIs. They found that during most nights the velocities matched but there were some cases where they did not. During some nights the depletion velocities were slower than the neutral winds and during other nights the depletions velocities were faster. If the plasma depletions match the neutral winds then the F region dynamo is fully active. In order to understand these results we refer to Equation 4.1. A fully operating F-region dynamo means that the plasma drifts are equal to the first term on the right hand side. If the depletions are moving slower than the neutral velocity then upward vertical plasma drifts or vertical current density may cause this difference. If the depletion velocity is faster than the neutral winds then one of the terms on the right side of Equation 4.1 may be responsible for this. The depletion velocity measurements made by *Chapagain et al.* (2013) were not at the magnetic equator so the depletion velocities were associated with higher altitudes than where the FPI measurements are made, which were not colocated and were closer to the magnetic equator. Neutral winds may be greater at these higher altitudes and could explain why they measured faster plasma drifts. The ASI and FPI that we use are colocated so there is no difference in altitude in our measurements. The vertical plasma drift term on the right side of Equation 4.1 can increase the zonal drift velocity if there is a downward plasma motion. The ISR measurements in Fig. 4.3 show that there is a downward motion of the plasma during the times when zonal plasma drifts are faster than the neutral winds. This is a likely explanation for the difference in velocities earlier in the night.

4.6 ESF at higher latitudes

In addition to using the Jicamarca ASI to observe bottomside depletions, we use the El Leoncito and Villa de Leyva ASIs to observe topside depletions. Observations

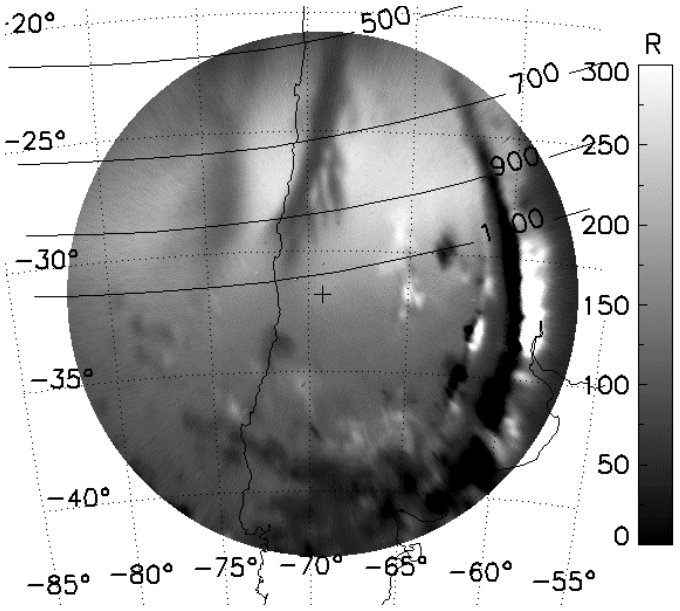

Fig. 4.17: An example of topside ESF observed at El Leoncito. The dark bifurcated structure extend from the top of the image toward the bottom is the ESF depletion. Dotted lines mark longitude and latitude. Black solid lines are lines of constant magnetic apex altitude. The gray scale shows the brightness in Rayleighs.

away from the magnetic equator measure topside ESF and are visible as bifurcated structures extending away from the magnetic equator. ESF processes are flux tube integrated (*Sultan*, 1996; *Weber et al.*, 1996; *Keskinen et al.*, 1998) so the topside structures at the magnetic equator map down to their magnetic foot points at higher latitudes (*Mendillo and Baumgardner*, 1982). These ASIs observe the footpoints of magnetic field lines that map to apex altitudes that are higher than the ASI observations at the magnetic equator (250 km). Figure 4.17 shows an example of ESF structures observed at El Leoncito. Two depletions are visible extending from the northern edge of the image to about zenith. Bifurcations of the depletions are visible. Clouds are visible to the south and to the east. The tips of these depletions map to about 1100 km at the magnetic equator.

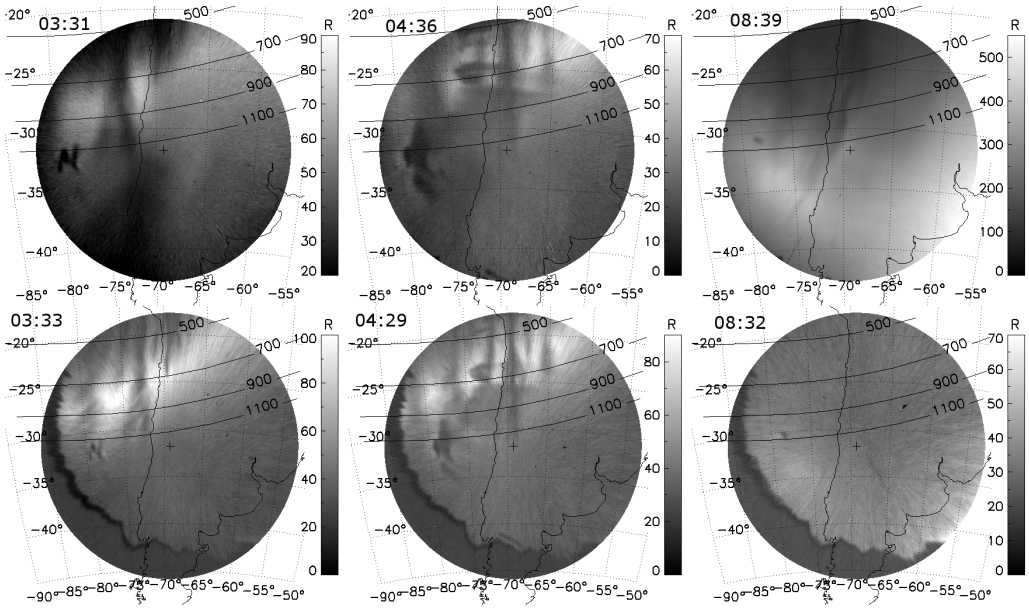

Fig. 4.18: Unwarped images from the El Leoncito ASI on 29 October 2014. The top row shows 6300 Å images and the bottom row shows corresponding 7774 Å images. The plus sign in the middle is the location of the ASI. The map shows the coasts of South America. Lines of constant magnetic apex altitude are shown from 500 to 1100 km. Depletions are visible extending from the north to zenith. The bright band visible in the north in the earlier images is the crest of the equatorial ionization anomaly. At 08:39 UT the 6300 Å emission is much greater due to the presence of a BW.

ASI depletions observed at higher latitudes latitudes can be related to ESF structures observed at the magnetic equator. On 29 October 2014, the night with data shown in Fig. 4.4 and Fig. 4.5, the El Leoncito and Villa de Leyva ASIs also detected airglow depletions. Images from El Leoncito on this night are shown in Fig 4.18. At 03:31 UT there is a large depletion at around -75° longitude that extends from the top to the middle of the image. Due to its higher latitude, these depletions are topside plumes that have apex altitudes above 1100 km. This same depletion is located in the center of the images taken around 04:30 UT.

Figure 4.19 shows images from the Villa de Leyva, Jicamarca, and El Leoncito ASIs from the same night as Figure 4.18 at 04:52 UT. At Villa de Leyva there were

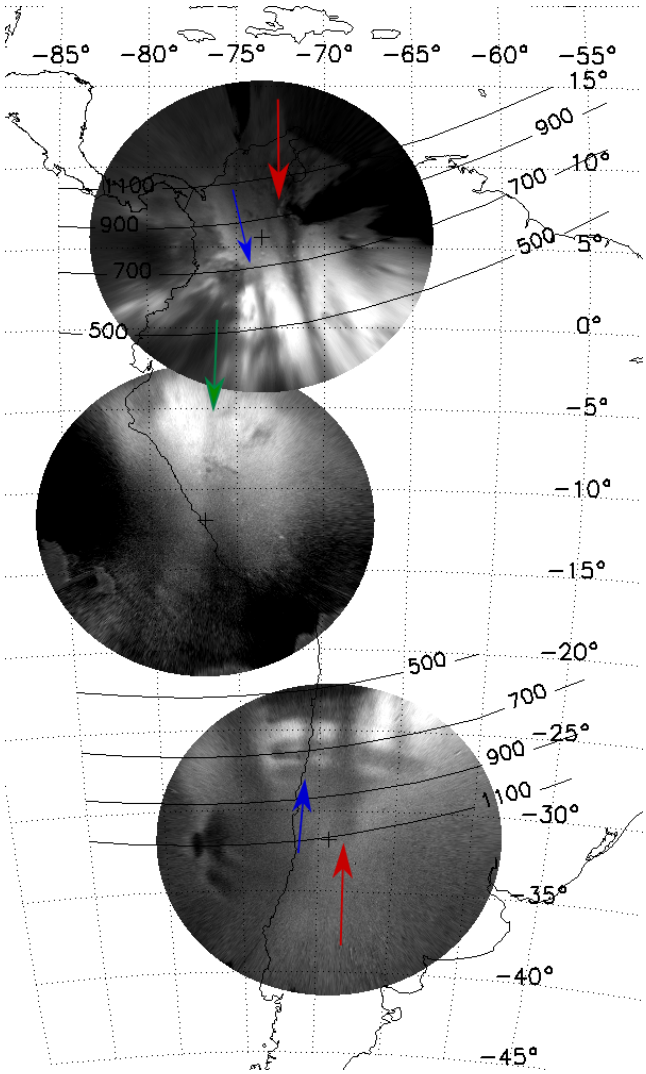

Fig. 4.19: Three unwarped images from the Villa de Leyva (top), Jicamarca (middle), and El Leoncito (bottom) ASIs on 29 October 2014 at 4:52 UT. Lines of constant magnetic apex altitude are shown from 500 to 1100 km. Clouds cover a lot of the Villa de Leyva image but two depletions are visible between -75° and -70° longitude, extending to 700 km and 1100 km magnetic apex altitude. One is marked a blue arrow and one with a red arrow. These depletions are also visible in the El Leoncito image but clouds are also in the field of view. The blue arrow at El Leoncito marks the depletion associated with the blue arrow at Villa de Leyva. The red arrow at El Leoncito marks the depletion associated with the red arrow at Villa de Leyva. At Jicamarca there is one depletion that is barely visible near zenith, marked with a green arrow.

clouds during most of the night, some of which are present in this image, but we are still able to determine the presence of airglow depletions. Two depletions are visible between -75° and -70° longitude, extending from the bottom of the image to 700 km and 900 km magnetic apex altitude. They are marked by red and blue arrows. At the same time these structures have conjugate depletions at El Leoncito. At Villa de Leyva the depletions extend from the southern edge of the image to the north while those at El Leoncito extend from the northern edge of the image to the south because they are flux tube aligned with vertical structures at the magnetic equator. There are also clouds in the field of view of the El Leoncito image (creating the dark horizontal bands around 700 km magnetic apex) but a depletion is visible at about -68° longitude, marked by a red arrow, that is the conjugate depletion of the one at Villa de Leyva around -70° longitude, also marked by a red arrow. Another depletion is just barely visible at El Leoncito around -71°, marked by a blue arrow, that is conjugate to the depletion around -74°, marked by a blue arrow. Low emission at Jicamarca makes it difficult to observe but there is a depletion near zenith, marked by a green arrow.

Although early in the night at Jicamarca we only see depletions at the edge of the ASI images, we can see a large-scale depletion at 03:33 UT with the El Leoncito ASI (Fig. 4.18). This depletion is about 3° to the east of the Jicamarca radar. We determine that this depletion is associated with the largest irregularity plume observed with the JULIA mode of the radar (Fig. 4.4). This irregularity plume occurs just before 03:00 UT and irregularities are visible up to 800 km in altitude. The depletion has an apex altitude greater than 1100 km, which is beyond the maximum altitude of the JULIA mode but from 700 to 800 km only relatively weak echoes are observed. At 04:30 UT depletions are just starting to appear in the field of view of the El Leoncito ASI (Fig. 4.18). At 04:52 UT there are depletions visible at Villa

de Leyva and El Leoncito (Fig. 4.19) when the airglow is still weak at Jicamarca and depletions are still only faintly visible. These depletions are associated with a plume of irregularities visible just before 05:00 UT (Fig. 4.4). In Fig. 4.19 the plumes extend to 1100 km in apex altitude but irregularities are only observed up to 650 km with the JULIA mode. Similar to the comparison at an earlier time, strong irregularities are not observed throughout the entire depletion.

The El Leoncito ASI also provides information about the EIA that redistributes low-latitude plasma, decreasing the 6300 Å emission at the magnetic equator. In Fig. 4.18 the 7774 Å images show the location of the southern crest of the anomaly early in the night. The crest of the anomaly is identified as the bright band at the top of the images around 25° S at 03:33 UT and 04:29 UT. From 03:33 to 04:29 the crest moves toward the equator and the emission in 7774 Å and 6300 Å decreases. This indicates that the plasma is moving back to the magnetic equator. The strong EIA crest early explains why the emission is weak at the magnetic equator and as it diminishes, the emission at the magnetic equator increases. At the end of the night, the EIA crest is no longer visible at El Leoncito because the plasma that formed the crest has moved back to the magnetic equator.

Later in the night we can detect depletions with the Jicamarca and El Leoncito ASIs that are not observed with the JULIA radar. These are "fossilized" depletions that were not formed over the radar and enter the field of view fully formed so the small-scale irregularities have dissipated. Figure 4.5 shows depletions at 09:08 UT on 29 October 2014 observed with the Jicamarca ASI and Fig. 4.18 shows depletions at 08:39 UT on the same night observed with the El Leoncito ASI. Figure 4.4 shows that no small-scale irregularities are observed after 08:00 UT. In addition to comparisons when features are visible with both instruments, these two instruments complement each other by providing information when one system does not detect ESF features.

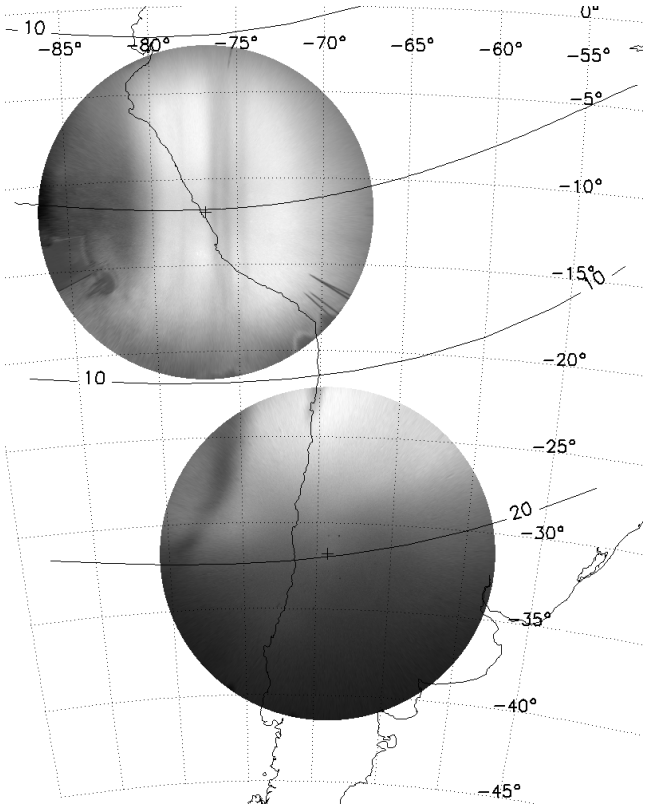

Fig. 4.20: Unwarped images from Jicamarca and El Leoncito on 3 Apr 2014. The Jicamarca image is at 04:15 UT and the El Leoncito image is at 04:18 UT. At Jicamarca bottomside depletions are visible and at El Leoncito topside plumes are visible. The magnetic equator is shown passing through the Jicamarca ASI field of view and lines of magnetic latitude at 10° and 20° are shown as well. The two images do not have the same color scale in order to make the features more clearly visible.

In RTI plots there is often a disruption in bottomside irregularities when topside plumes are visible (e.g., *Hysell and Burcham*, 2002). In Fig. 4.4 this can be seen at 03:00 UT as the bottomside irregularities are no longer visible and a large plume has risen to the topside. To complement this we compare observations of bottomside airglow depletions at Jicamarca with topside airglow depletions at El Leoncito. Figure 4.20 shows concurrent images from 3 Apr 2014 where bottomside depletions are visible at Jicamarca and topside depletions are visible at El Leoncito. We see that although there is a group of depletions visible at Jicamarca, we only observe

one topside plume. We are unable to determine which bottomside depletion becomes a topside plume or if the bottomside features merged to form one plume since the topside plume is as wide as the group of depletions. ESF plumes are not expected to have the same width at all altitudes and can be wider at higher altitudes (e.g., *Retterer*, 2010). We have looked at other cases and have found that we only observe one topside plume associated with a group of bottomside depletions. Another possibility is that the bottomside depletions evolved into plumes that merged (e.g., *Huang et al.*, 2012). We were not able to find any significant differences between bottomside depletions (e.g., relative brightness of the depletion compared to the background or its width) that form plumes and the ones that do not.

4.7 MTM effects on ESF

Finally, in this section I investigate how other perturbations in the upper atmosphere can interact with ESF airglow depletions.The midnight temperature maximum (MTM), discussed in Chapter 3 and the other major focus of this dissertation, is a distinct phenomena from ESF but they share some characteristics. They occur in the same altitude region of the upper atmosphere, typically occur in the same latitude range, and occur at night. ESF occurs mostly during post-sunset and the MTM occurs around midnight so simultaneous observations are infrequent. In this section I present a case where these two upper atmospheric perturbations unexpectedly interact.

The overlap between ESF and the MTM can be observed readily with an ASI at latitude, between about 10° and 30° from the magnetic equator. At these latitudes the effect of the MTM is observed as a brightness wave (BW) in the ASI FOV. Airglow depletions at these latitudes are associate with ESF structures that map to the topside of the ionosphere at the magnetic equator. The brightness wave can occur

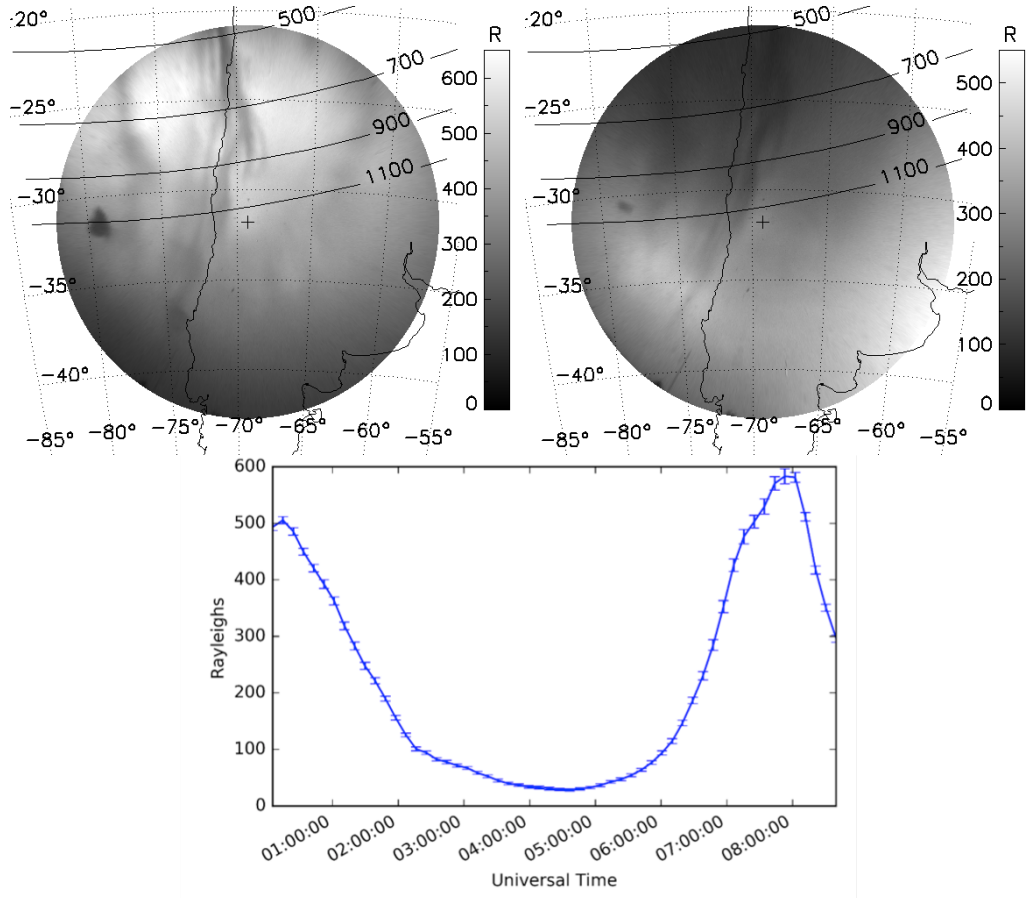

Fig. 4.21: Two unwarped images (top) from the El Leoncito ASI on 29 Oct 2014. The left image is at 07:24 UT. Dotted lines show latitude and longitude. Solid lines are lines of constant magnetic apex altitude and the numbers show the altitude in km at the equator. The gray scale shows the brightness in rayleighs. At this time a BW is visible in the image and con be identified by the increased emission to the North. The airglow depletion due to ESF is seen as the dark feature extending from the top of the image to zenith. The right image is at 08:39 UT, after the BW has passed through zenith. On the bottom is the brightness in rayleighs at zenith as a function of UT. This is calculated from a 16x16 pixel box at zenith and the error bars are the standard deviation of this measurement. The brightness wave is the increase in brightness that peaks at 08:00 UT.

during the same time period that ESF occurs, but when this happens it typically does not impact ESF. Figure 4.21 shows a night where both events occurred without any interaction. The two images (top) show ESF structures observed with the ASI at El Leoncito. The first image (left) occurs at the beginning of the brightness wave

and the second image (right) occurs after the brightness wave has passed through zenith. The plot on the bottom shows the 6300 Å emission as a function of time. The ESF structure is visible as the dark feature extending from the top of image down toward the bottom. As the background emission increases, the morphology and brightness of the depletions do not change. This is what typically is observed and what would generally be expected. The movement of the plasma down magnetic field lines from the MTM should not affect the depleted regions due to the presence of the electric fields within them.

Figure 4.22 shows another night where the BW associated with the MTM has an impact on the airglow depletions. In the earlier image of Figure 4.22, the airglow depletion is what is expected from a topside structure. As the BW passes through the region of the depletion, the depletion becomes filled in and ultimately ends up brighter than the background. There are nine frames between the two images presented here that unambiguously show that this is the same feature and it is observed as filling in. On this same night we also have observations from the Villa de Leyva ASI. There was only a brief period of time where it was clear enough to observe at Villa de Leyva so we are not able to determine if there was a brightness wave but we can identify a depletion associated with ESF. Figure 4.23 shows an image from Villa de Leyva (06:40 UT) along with a concurrent image from El Leoncito (06:38 UT). The bright airglow enhancement is still visible during this time in in the El Leoncito field of view. In the Villa de Leyva image, an airglow depletion is observed, extending from the bottom of image, past zenith between -70° and -75°. The location of this depletion is at the other end of the magnetic field lines that are within the El Leoncito airglow enhancement. To better compare the depletion and enhancement, brightness values along a line of constant latitude at Villa de Leyva, shown as the red line in Figure 4.23 (left), have been extracted and plotted in blue in Figure 4.24.The positions of

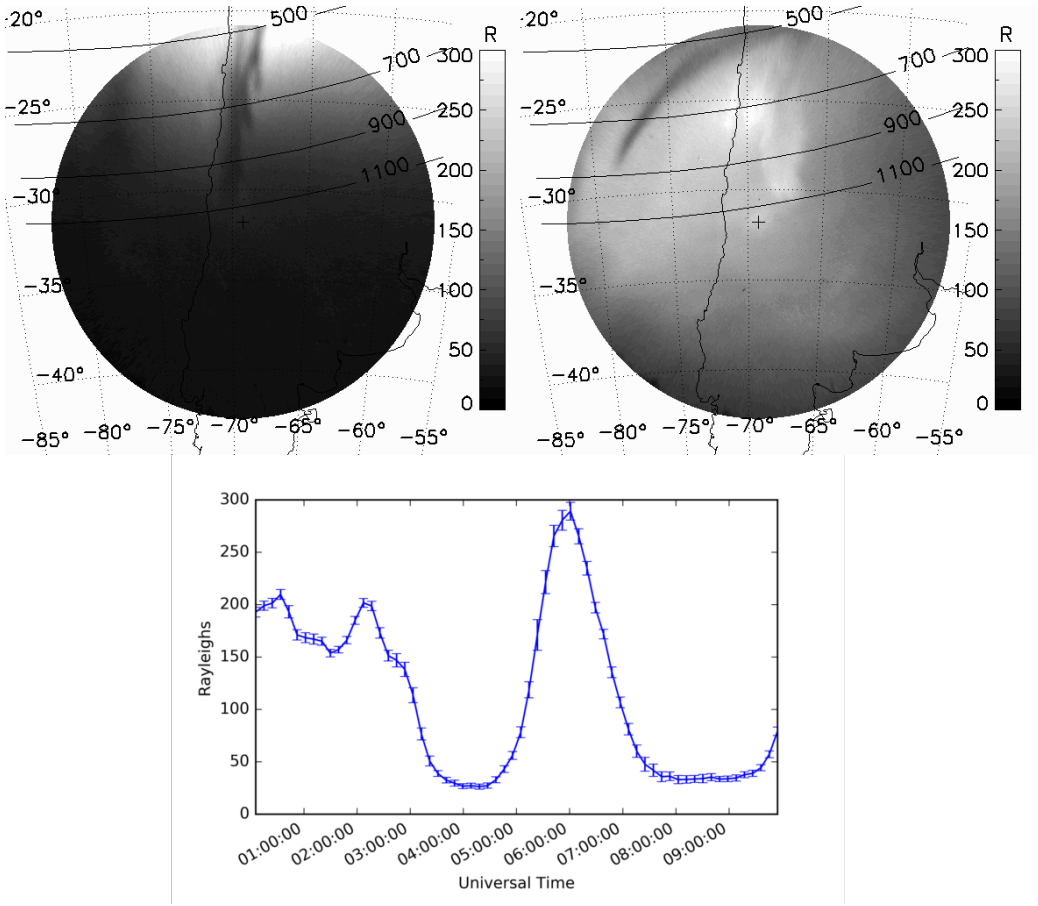

Fig. 4.22: Two unwarped images (top) from the El Leoncito ASI on 13 May 2015. The left image is at 04:46 UT. Solid lines are lines of consta nt magnetic apex altitude and the numbers show the altitude in km at the equator. The gray scale shows the brightness in rayleighs. At this time a BW is just starting to appear in the image and con be identified by the increased emission to the North. The airglow depletion due to ESF is seen as the dark feature extending from the top of the image to zenith. The right image is at 06:19 UT, after the BW has passed through zenith. The ESF structure is no longer an airglow depletion and is now brighter than the background. On the bottom is the brightness in rayleighs at zenith as a function of UT. This is calculated from a 16x16 pixel box at zenith and the error bars are the standard deviation of this measurement. The brightness wave is the increase in brightness that peaks at 06:00UT.

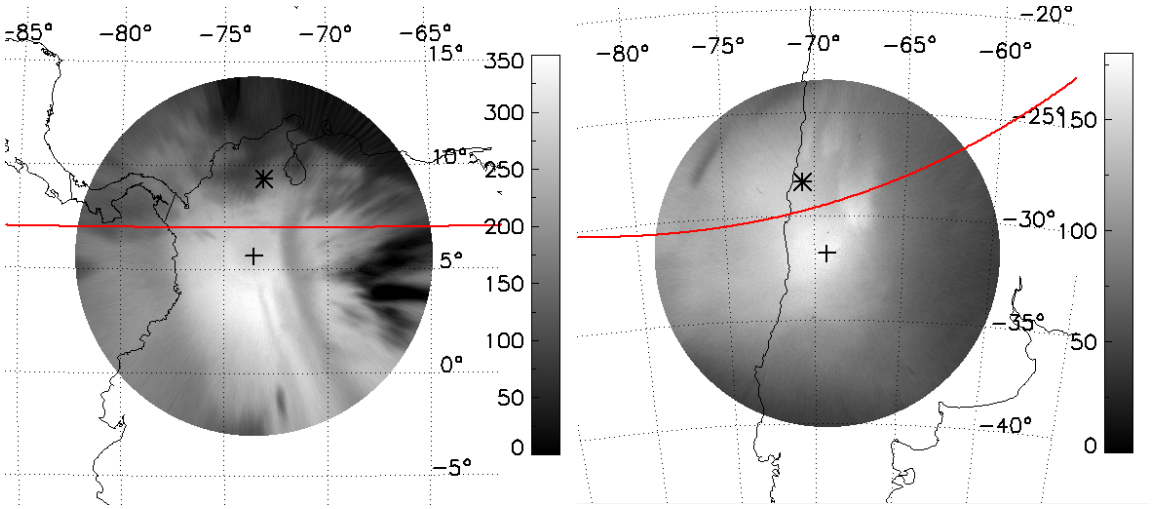

Fig. 4.23: Two unwarped images from 13 May 2015. (Left) An image from Villa de Leyva at 06:40 UT. The red line marks the location where brightness values are extracted for analysis. (Right) An image from El Leoncito at 06:38 UT. The red line is the conjugate line of the line in the Villa de Leyva image. The airglow enhancement between -65° and -70° is the same enhancement from Figure 4.22 and is conjugate to the depletion between -70° and -75° at Villa de Leyva

all the points of this line were mapped along magnetic field lines to the opposite hemisphere to measure the conjugate values in the El Leoncito image. The locations of these points are shown as the red line in Figure 4.23 (right) and are plotted in green in Figure 4.24. This plot shows a clear depletion around -72° longitude at Villa de Leyva (blue line). The El Leoncito points have been mapped to the Villa de Leyva field of view so that the two can be directly compared. The green line from El Leoncito shows that there is an airglow enhancement about -72°, the same place that there is a depletion at Villa de Leyva. This confirms that these two features are conjugate and further shows that there is only enhancement in one hemisphere.

To explain this event we look at previous studies that showed an airglow depletion becoming an enhancement when their was no MTM present. *Martinis et al.* (2009) showed examples of brightening of ESF airglow depletions. In this study the observations were made using the Arecibo ASI and all occurred during December sol-

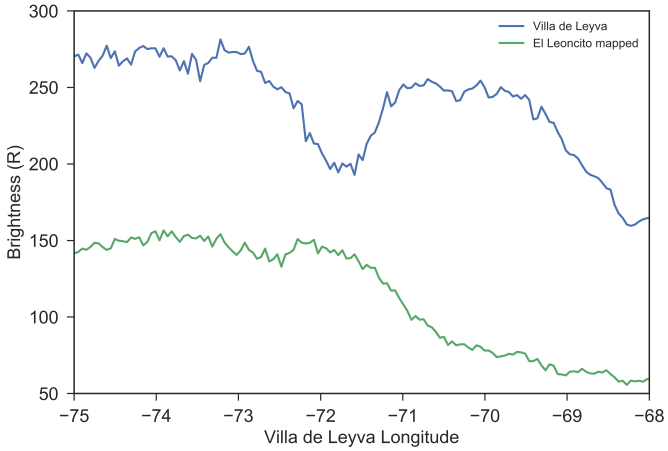

Fig. 4.24: The blue line in this plot shows the brightness values at constant latitude at Villa de Leyva, shown as the red line in Figure 4.23 (left). The green line shows the brightness values at the conjugate location at El Leoncito, shown as the red line in Figure 4.23 (right). The El Leoncito positions have been mapped back to the Villa de Leyva longitudes to remove the effects of the Earth's magnetic field.

stice. No BWs were detected in these observations. In addition to this paper *Krall et al.* (2009a) presented model results using the NRL ionosphere model SAMI3/ESF to reproduce this enhancement. These studies determined at Arecibo there must be a northward meridional wind and there must be converging zonal winds. The northward meridional wind will cause plasma to move down the angled magnetic field lines at Arecibo. As plasma moves down, the airglow increases. The converging zonal winds weaken the electric field of the airglow depletion so that it is not the background that becomes brighter but also the ESF structure. The converging wind is known to happen near sunrise when the meridional winds switch directions.

At El Leoncito, there must be a southward meridional wind to move plasma down the field lines. The converging zonal winds still apply at EL Leoncito. The MTM can create the conditions for this to happen. At El Leoncito the BW travels South-West. It is observed travelling in this direction and BW wave is know to be observed because the plasma is moving down the magnetic field lines. Additionally,

the MTM is known to create or enhance a poleward wind (*Meriwether et al.*, 2008). This shows that the first condition for enhancement is met. The MTM is also known to cause a reversal or abatement in the typically eastward zonal wind (*Colerico et al.*, 2006). This reversal can cause a convergence in the same way that the reversal near sunrise can. No brightening was observed at Villa de Leyva but we only have limited observations from that night due to clouds. There may not have been a BW at Villa de Leyva or it may have occurred at a different time. Thus, in some situations the MTM can produce the right conditions for the brightening of an ESF depletion.

4.8 ESF Summary

In this chapter I have discussed many observations of ESF with ASIs and the new science that has been learned from them. The ability to observe ESF at the magnetic equator and higher latitudes was discussed. I showed observations of both bottomside and topside ESF and how these observations are compared with the more well known radar observations of ESF. Early in the night when the airglow emission is weak only the radar is able to detect irregularities with 3 m scale sizes. Although it can be challenging to observe ESF at the magnetic equator due to the pre-reversal enhancement, the combination of instruments at Jicamarca can be used to analyze ESF in a way that cannot be done elsewhere.

I modeled the airglow emission using IRI and ISR data and found that using radar data and NRLMSISE-00, the Boston University airglow code reproduces accurately the trend in the observations, although the peak modeled values are a factor of 2- 3 smaller. This inconsistency could be due to contamination from nearby city lights.

A more in-depth analysis of the comparison between radar systems and the Jicamarca ASI was presented in order to better understand the connection between

large-scale ESF depletions and small-scale irregularities. We found that there is a higher occurrence of radar echoes coming from regions identified as the western wall of large-scale depletions in comparison with echoes coming from other regions within the depletion. We analyze the conditions present in the different depletion regions to determine what instabilities may be present and producing to the irregularities. The conditions for the wind driven gradient drift instability are met on the western wall of the depletion and our results suggest that this instability is responsible for the 0.34 m and 3 m radar echoes on the western wall. The sub-meter irregularities have not been well studied in the past but our results suggest that the conditions may be correct for the lower-hybrid drift instability to produce 0.34 m radar echoes on the eastern and western walls.

I found that bottomside airglow depletions at Jicamarca occur in groups separated by 400-500 km. Within the groups the separation tended to be 50-100 km. This indicates that a LSWS may be modulating bottomside depletions.

I presented a case study comparing the zonal speed of neutral winds and zonal plasma drift obtained from colocated FPI and ASI, respectively. Early in the night the depletions are moving faster than the neutral winds, a result attributed to downward drifts that modify an active F-region dynamo.

The connection between bottomside structures and topside structures is an active area of study. I observed that groups of bottomside depletions only formed one topside plume. It is not clear whether this plume is from one depletions within the group or a combination of them. No difference in the ASI images was found between bottomside depletions that form topside plumes and those that do not.

Finally, in this chapter I examined a case where the BW associated with an MTM had a significant impact on a topside airglow depletion. As the BW passed over the depletion, the depletion became brighter than the background. I found

that the conditions needed to produce this effect, southward meridional winds and converging zonal winds, often accompany the MTM and the associated BW.

These studies of various aspects of ESF combined create a more complete understanding of ESF and expand the knowledge of the formation, evolution, and connection between scale sizes of ESF, all active areas of study.

Chapter 5

Influence of the Earth's magnetic field on ESF at magnetically conjugate locations

5.1 Introduction

The flux tube integrated nature of ESF, as discussed in Chapter 4, implies that airglow depletions associated with ESF should be observed at both ends of magnetic field lines. Regions on the Earth that are on the same magnetic field but in opposite hemispheres are referred to as conjugate locations. The BU ASIs are well situated for measuring the conjugate nature of ionospheric processes. In this chapter I focus on topside ESF structures that are observed away from the magnetic equator with ASIs. Two imagers in South America are particularly useful for these observations, the ASI at Villa de Leyva, Colombia and the ASI at El Leoncito, Argentina. Figure 5.1, similar to Figure 2.3 in Chapter 2, shows the locations and fields of view for these two ASIs. The red dots show the locations of the imagers and the red triangles show the conjugate location of the imagers. The conjugate location of each imager is located within the field of view of the imager in the opposite hemisphere. The conjugate location is quite close to the location of the imager which allows for a comparison between the two sites. To compute the conjugate locations I use the International Geomagnetic Reference Field (IGRF-12) (*Thébault et al.*, 2015)

It is expected that that airglow structures associated with ESF should be observed concurrently at both sites since the overall process is flux-tube integrated (e.g.,

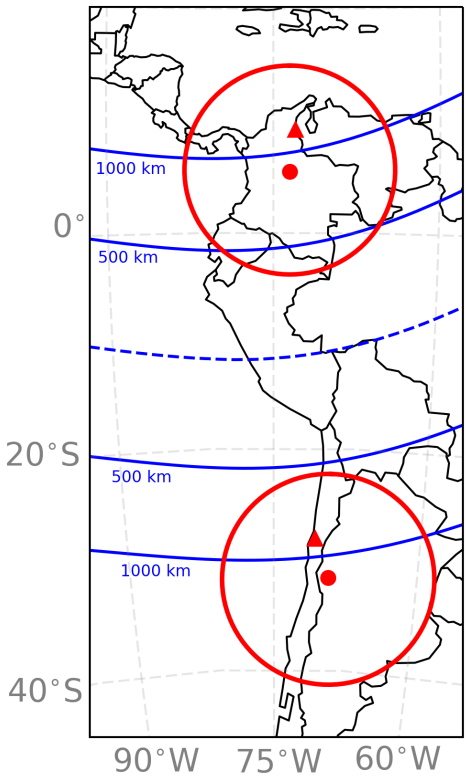

Fig. 5.1: A map of western South America showing the location of the Villa de Leyva (top) and El Leoncito (bottom) ASIs as red dots. The red circles around the dots are the fields of view for an airglow layer at 300 km and a zenith angle of 80°. The red triangle in the Villa de Leyva field of view is the conjugate location of the El Leoncito ASI. The red triangle in the El Leoncito field of view is the conjugate location of the Villa de Leyva ASI. The blue dotted line is the magnetic equator and the solid blue lines are lines of constant magnetic apex altitude.

Mendillo et al., 2005) and that they should have similar morphology and evolution. Modeling efforts have shown that these large scale depletions should be very similar at both ends of the magnetic field lines (e.g., *Yokoyama et al.*, 2014). Previous studies have shown that ASIs can observe ESF airglow depletions at both conjugate locations (e.g *Martinis and Mendillo*, 2007). There have also been some research on the differences in morphology between conjugate locations (*Otsuka et al.*, 2002; *Shiokawa et al.*, 2004) and on velocity comparisons of conjugate depletions (*Fukushima*

et al., 2015). These studies found that in general the morphology and velocities were similar between conjugate sites but small differences in size, shape, and velocity were observed.

Figure 5.2 shows an example of the conjugate nature of ESF depletions.The left image shows an unwarped image at Villa de Leyva on 10 Mar 2015 at 02:06 UT. The right image is the result of mapping an image from El Leoncito along magnetic field lines to it conjugate location in the Northern Hemisphere. In each image, two depletions with very similar structures are present. Figure 5.3 is a 5° latitude by 5° longitude region of each image to show how similar the features are. Although on this night these features match very well, after mapping along magnetic field lines, there are differences observed before they have been mapped and other nights do not match as well.

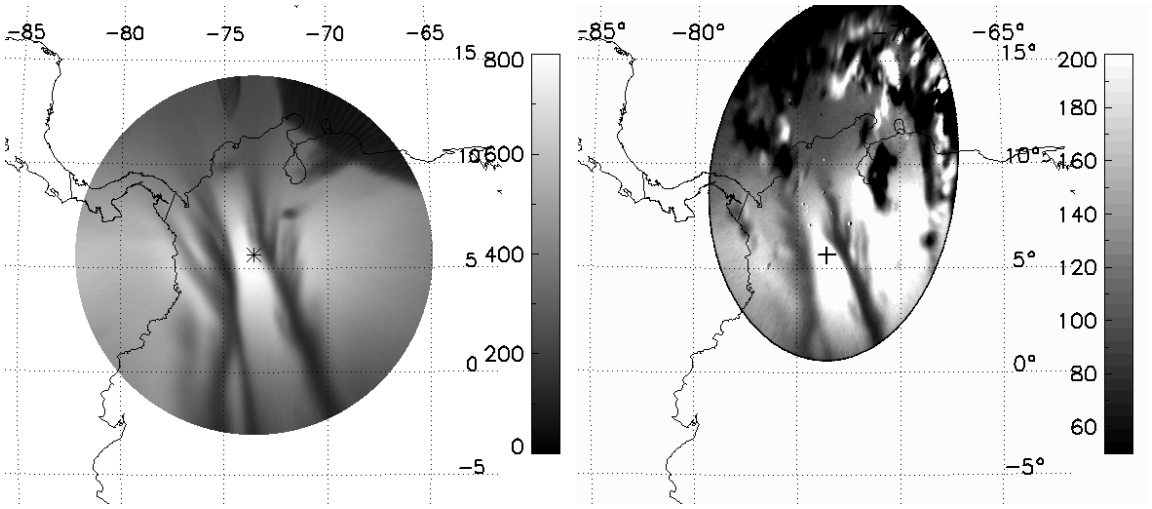

Fig. 5.2: (Left) An unwarped image at Villa de Leyva on 10 Mar 2015 at 02:06 UT. (Right) An image from the El Leoncito ASI at the same time that has been mapped along magnetic field lines to its conjugate location.

In this chapter I expand on the previous work done in order to better understand the differences in the morphology and velocity of ESF airglow depletions at conjugate sites in the American sector. This region is unique due to the presence of the South

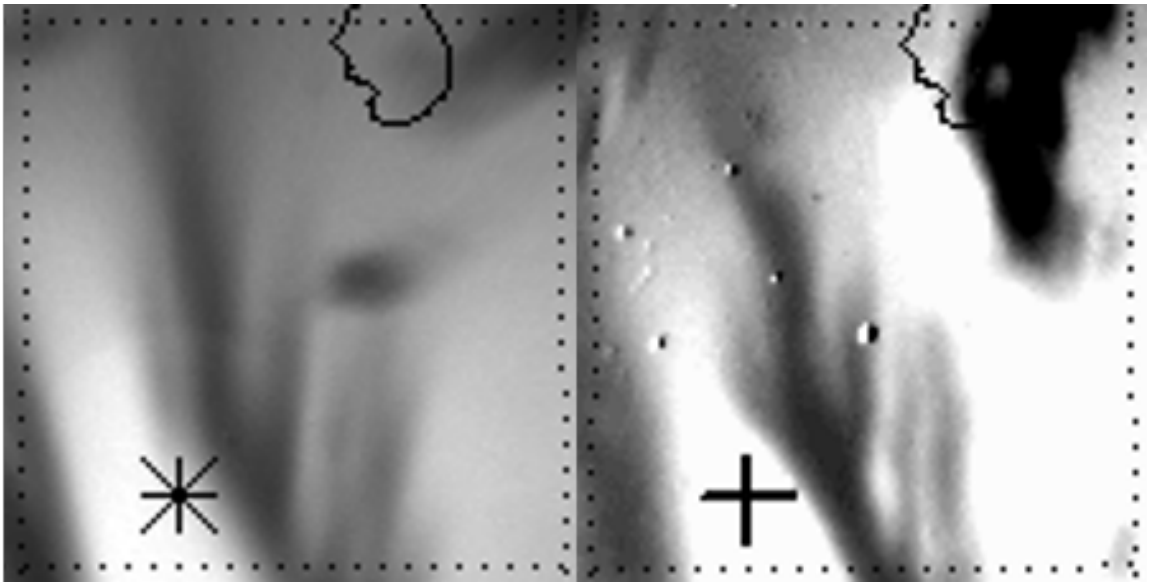

Fig. 5.3: A 5° latitude by 5° longitude region from each image in Figure 5.2

Atlantic Anomaly, a region of decreased magnetic field strength in the South Atlantic Ocean and South America. I compare the width, extent, and velocity of depletions at conjugate sites in western South America, which has not been done before at these locations. If differences in the morphology and velocity of airglow depletions are observed between conjugate sites then this can be used to infer information about upper atmospheric parameters such as airglow emission altitude and magnetic field strength.

5.2 Width of Airglow Depletions

Airglow depletions associated with topside ESF are expected to have nearly identical morphology at both ends of magnetic field lines. I compare the width of the airglow depletions observed with the ASIs at El Leoncito and Villa de Leyva. In order to accurately measure the width of the depletions I must determine the altitude of emission. This is done with the BU airglow code described in Section 2.2 and uses IRI-2016 for the ionospheric input into the airglow code and NRLMSISE for

the thermospheric inputs (neither of the two sites have colocated instruments that measure electron density).

Preliminary results indicated that airglow depletions over El Leoncito seem wider than those observed concurrently at Villa de Leyva. Figure 5.4 shows concurrent images from El Leoncito and Villa de Leyva on 14 Feb 2015 at 05:35 UT. The depletion that passes through zenith at Villa de Leyva (+ symbol) does not appear to be as wide as the conjugate depletion observed with the El Leoncito ASI (asterisk). The conjugate depletion is identified by its location in the conjugate point of the Villa de Leyva ASI. The BU Airglow model, using IRI-2016 and NRLMSISE-00 as inputs, determines the height that is used. For Villa de Leyva the calculate altitude was 220 km and for El Leoncito the calculated altitude is 260 km.

To accurately compare the width I choose a point in the center of a depletion in the Villa de Leyva image and take a cut along a constant geographic latitude. For the night shown in Figure 5.4 this line is through zenith, marked by the cross in the left panel. I calculate the conjugate point for the cross and take a cut along a constant geographic latitude at the latitude of the conjugate point, marked by the asterisk is the right panel. Since these two sites are at different latitudes, the distance between degrees of longitude varies between the two sites and they cannot simply be compared by plotting brightness versus longitude. For each site the center of the depletion is assumed to be the minimum of the depletion and then the distance in km of each point along the cut is calculated. Figure 5.5 shows the brightness in rayleighs of the conjugate depletions at each site. For each site, zero distance is defined as the minimum of the depletion so they can be directly compared. At Villa de Leyva the center of the depletion and thus zero distance is -73.45° longitude and at El Leoncito it is -70.51° longitude. The left plot shows the brightness in rayleighs. The emission is much greater at Villa de Leyva than at El Leoncito making it difficult to compare

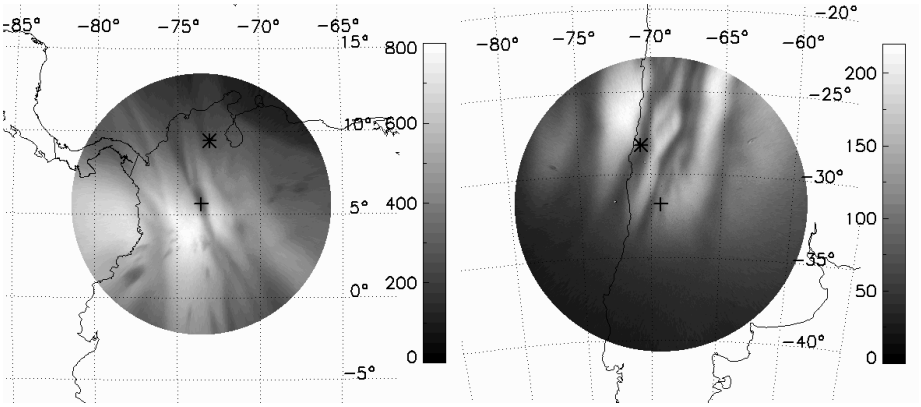

Fig. 5.4: (left) An image taken with the Villa de Leyva ASI at 05:35 UT on 14 Feb 2015. It has been unwarped at an altitude of 220 km. The cross is the location of the ASI and the asterisk is the location of the conjugate point of the El Leoncito ASI. (right) An image taken with the El Leoncito ASI at 05:33 UT on 14 Feb 2015. It has been unwarped at an altitude of 260 km. The cross is the location of the ASI and the asterisk is the location of the conjugate point of the El Leoncito ASI. The gray scale associated with each image shows the emission in rayleighs.

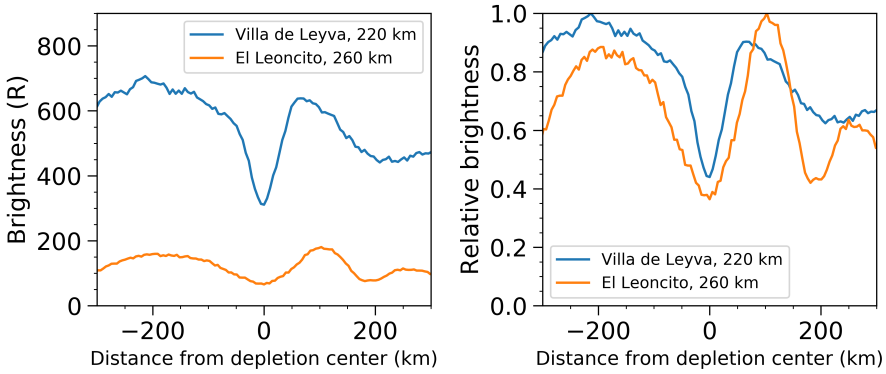

Fig. 5.5: (left)Plots showing cuts through conjugate depletions in Figure 5.4. The blue line shows the values along a constant geographic latitude at the cross (5.6° N) in the left panel of 5.4 at Villa de Leyva. The orange line is shows the values along a constant geographic latitude at the conjugate location of zenith at Villa de Leyva, which is at the asterisk in the right panel of Figure 5.4. Distances for each cut is measured from the center of the respective depletion such that the minimum of each appears at zero distance. (right) The values from the same locations as the left panel but now they have been normalized to their respective maxima.

them. Figure 5.5 (right) shows the brightness values from the same locations as Figure 5.5 (left) but each has been normalized to their respective maximum.

From Figure 5.5 it can be seen that the depletion at El Leoncito is wider than the depletion at Villa de Leyva. Additionally, the intensity difference between the background and the depletion is similar in percentage at each site even though the absolute emissions are different. At El Leoncito the depletion minimum is about 64% dimmer than the background and at Villa de Leyva the depletion minimum is about 56% dimmer than the background. To get a quantitative measure of the width, a Gaussian function is fit to each depletion. First a polynomial is fit to the background and then is subtracted to remove background variations in brightness. Then a Gaussian function is fit to the depletion using the least squares method. The parameters of the Gaussian function are then used to determine the full width at half the depletion depth, similar to determining the full width at half maximum. Using this method, the width of the Villa de Leyva depletion is 62 km. The width of the El Leoncito depletion is 130 km.

The assumed altitude of the airglow layers can impact the width comparisons. For a given image, the assumed altitude will be a factor in the measurement of the width. The higher the altitude of the airglow layer, the larger the depletion will appear because the same field of view is projected onto a larger area. The El Leoncito image is unwarped at a higher altitude than the Villa de Leyva image due to airglow calculations from the BU Airglow Model. If the two images are both unwarped at an altitude of 250 km, the depletion at El Leoncito is still wider by about 45 km. The Villa de Leyva image would have to be unwarped at a much higher altitude than the El Leoncito image to make up for the observed difference in width. The airglow emission is much greater at Villa de Leyva than at El Leoncito which means that the peak of the ionosphere is lower at Villa de Leyva, the electron density is greater

at Villa de Leyva, or both. Additional observations from TEC measurements near these sites from the Low Latitude Ionospheric Sensor Network (LISN) indicate that it is unlikely that the altitude of emission at Villa de Leyva is much higher than at El Leoncito. The TEC is larger at Villa de Leyva (∼40 TECU) than at El Leoncito (∼25 TECU) by a factor of 1.6. As seen in Figures 5.4 and 5.5 the background emission near the depletion at Villa de Leyva is about 700 R and the background emission near the depletion at El Leoncito is about 200 R. The Villa de Leyva emission is larger than the El Leoncito emission by a factor of 3.5. 6300 Å emission is directly proportional to electron density so if electron density was the only reason for the difference in emission than it would be expected that the TEC ratio would be similar to the emission ratio, ∼3.5. Thus, the TEC difference is not enough to account for the airglow emission difference between the two sites. In order to account for the greater emission at Villa de Leyva, the electron density peak, and thus the airglow emission layer, must also be at a lower altitude than at El Leoncito. This inference is consistent with the altitudes of emissions used in Figure 5.4 and the subsequent analysis, 220 km at Villa de Leyva and 260 km at El Leoncito. This means that on this night, the larger width at El Leoncito is not due to the assumed airglow altitudes and must be due to other factors.

The differences in width are likely related to variations in the configuration and magnitude of the magnetic field between the two sites. El Leoncito is located close to the South Atlantic Anomaly so the magnetic field is about 30% weaker here compared to its conjugate point. Additionally, the shape of ESF depletions is dependent on the orientation of the magnetic field of the Earth. They are flux tube aligned and travel perpendicular to magnetic field lines. Thus, the width of these depletions measured at a constant geographic latitude will be impacted by the tilt of the Earth's magnetic

field. The conjugate points of a line at a constant geographic latitude at Villa de Leyva do not fall along a line of constant geographic latitude at El Leoncito.

To investigate the extent to which the orientation and magnitude of the Earth's magnetic field impacts the difference in width I compare cuts through both images that are conjugate all along the cut. As in Figure 5.5, I start with a line at a constant latitude at Villa de Leyva, the same line used before. For each point along the line I calculate the conjugate location. This creates a line that is curved relative to lines of geographic latitude. Figure 5.6 shows this curved line at El Leoncito. With this curved line I take the brightness at each point along the line. This cut is then mapped back to the conjugate location at Villa de Leyva so that the effects from the tilted magnetic field and weaker field strength in the El Leoncito field of view have been removed.

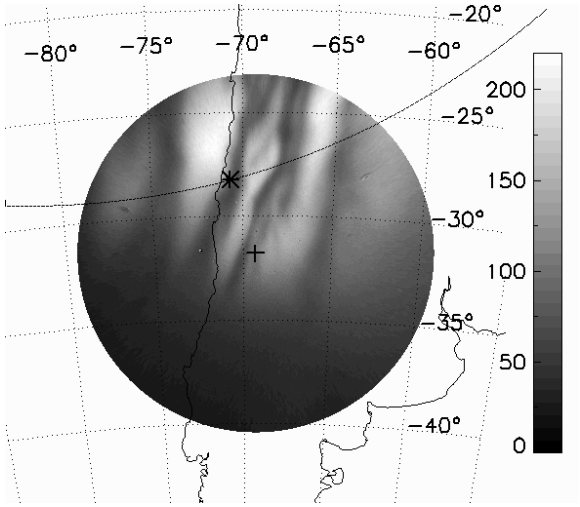

Fig. 5.6: An image taken with the El Leoncito ASI at 05:33 UT on 14 Feb 2015, the same image in Figure 5.4. This figure shows in a curved black line the result of a mapping a line of constant geographic latitude at Villa de Leyva along magnetic fields lines to it conjugate location. It has been unwarped at an altitude of 260 km. The cross is the location of the ASI and the asterisk is the location of the conjugate point of the El Leoncito ASI. The gray scale associated with each image shows the emission in rayleighs.

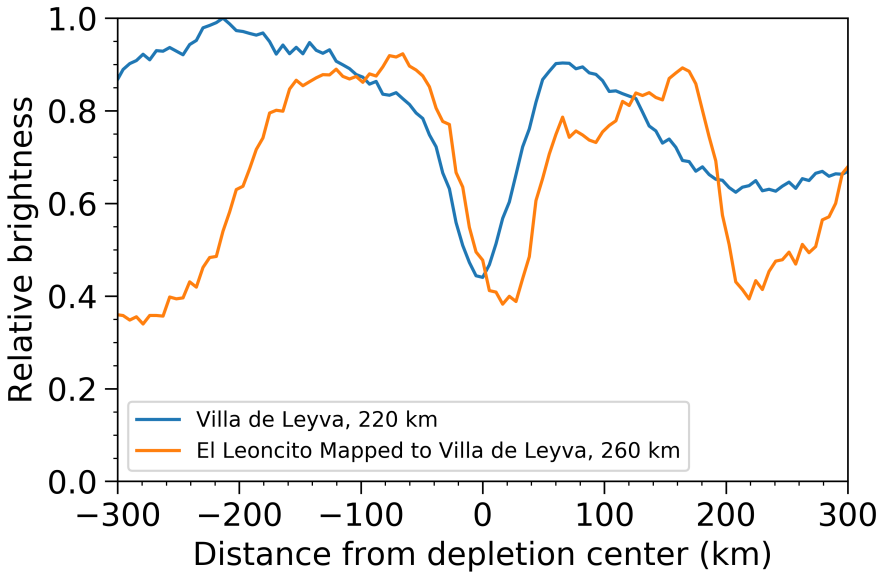

Fig. 5.7: Plot showing cuts through conjugate depletions in Figure 5.4. The blue line is a cut along a constant geographic latitude at the cross (5.6° N) in the left panel of 5.4 at Villa de Leyva. The orange line is a cut along the conjugate line marked in Figure 5.6 and mapped back to Villa de Leyva. Distances for each cut is measured from the center of the Villa de Leyva depletion. This is different from Figure 5.5 in order to show that the center of one depletion does not map exactly to the center of the other depletion. The brightness is much greater at Villa de Leyva so they have been normalized to their respective maxima.

The mapped El Leoncito cut is shown in Figure 5.7 along with the same Villa de Leyva cut from Figure 5.5. In this case, the zero point on the x-axis is the center of the Villa de Leyva depletion. The El Leoncito cut has not been adjusted to have the center at zero because if there was perfect conjugate mapping then the center of the two depletions should both be at zero. This highlights that the mapped El Leoncito depletion is offset by about 16 km, which is a difference of about 3 pixels in the Villa de Leyva field of view. Figure 5.7 shows that depletions are much more similar in width compared to Figure 5.5. Using the same method of fitting a Gaussian as before, the width of the mapped El Leoncito depletion at half the depth is 68 km, very close to the 62 km width of the Villa de Leyva depletion. This shows that

the difference in width can be attributed to the variations in the configuration and magnitude of the Earth's magnetic field between the two sites.

The 16 km offset between the depletions may be due to the altitudes that were determined for unwarping for the images. The two models used as inputs to determine the airglow altitude, IRI-2016 and NRLMSISE-00, are both empirical climatological models. These models may not be accurately representing the conditions on this day. I tested a variety of other combinations of altitudes to see if a different combination would remove the offset. Changing the altitude of emission changes the field lines that pass through a depletion due to size and position changes of the features at different altitudes and the angle of the field lines. I tried combinations using 220 km at Villa de Leyva and combinations using 260 km at El Leoncito but none of those worked. I then tested various combinations of altitudes using increments of 50 km as shown in Table 5.1. The columns are the altitudes at Villa de Leyva and the rows are altitudes at El Leoncito. The offsets are given in kilometers. One pixel is about

Table 5.1: Conjugate Depletion Offsets

	Villa de Leyva			
El Leoncito	200 km	250 km	300 km	350 km
200 km	43	27	5	-38
250 km	32	22	-5	-43
300 km	16	11	-16	-43
350 km	11	0	-11	-60

5 km so the smallest offset excluding zero is 5 km. Positive offsets are when the El Leoncito depletion is shifted to the east. Combinations where the El Leoncito altitude of emission is lower than the altitude of emission at El Leoncito are not expected to be accurate because the brightness differences and TEC differences discussed earlier indicate that El Leoncito should be at a higher altitude. Three combinations show very small offsets: 200 km at El Leoncito and 300 km at Villa de Leyva, 250 km at El Leoncito and 300 km at Villa de Leyva, and 350 km at El Leoncito and 250 km at

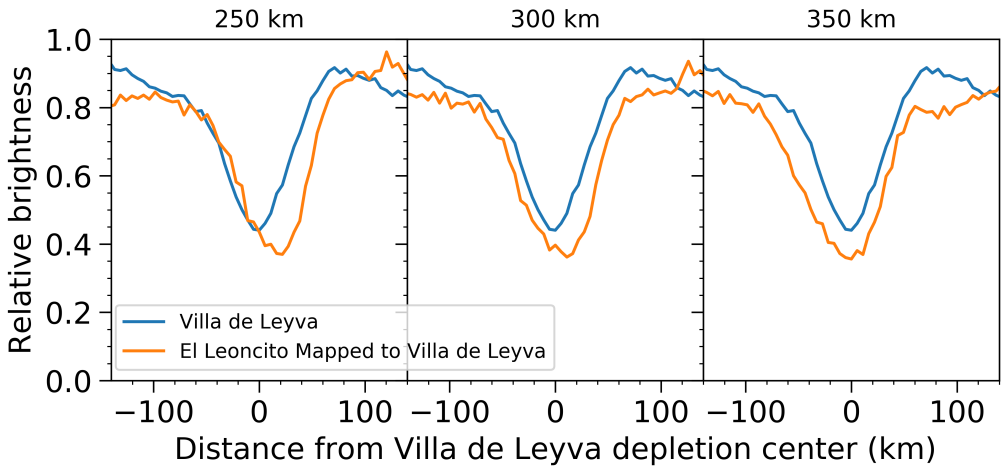

Fig. 5.8: Plots showing cuts through conjugate depletions in Figure 5.4, similar to Figure 5.7. The blue line is a cut along a constant geographic latitude at the cross (5.6° N) in the left panel of 5.4 at Villa de Leyva. For each plot the Villa de Leyva image has been unwarped at the same altitude, 250 km, so that the blue line is the same in each. The orange line is a cut along the conjugate line and mapped back to Villa de Leyva. Three different El Leoncito altitudes are used, 250 km, 300 km, and 350 km. Distances for each cut is measured from the center of the Villa de Leyva depletion. The brightness is much greater at Villa de Leyva so they have been normalized to their respective maxima.

Villa de Leyva. Two of these combinations have El Leoncito at a higher altitude than Villa de Leyva which is not likely to be the case. Additionally, the width comparison with these combinations still show a much wider width at El Leoncito. 350 km at El Leoncito and 250 km at Villa de Leyva shows the smallest offset. Figure 5.8 shows how the offset decreases with three different altitudes at El Leoncito and a constant altitude at Villa de Leyva.

The left panel shows cuts where images from both sites are unwarped at an altitude of 250 km. The Villa de Leyva cut is the same altitude, 250 km, for each panel. The middle panel shows El Leoncito unwarped at 300 km and the right panel shows El Leoncito unwarped at 350 km. Offsets are reduced when using 300 km and 350 km altitudes at El Leoncito. Unwarping El Leoncito at 350 km and Villa

de Leyva at 250 km gave the smallest offset of any combination of altitudes. The widths also match well with this altitude combination. Other combinations with offsets of 11 km not shown here had widths that did not match well. The decrease in the offset seen in the middle and right panel indicate that unwarping at these higher altitudes may be more accurate than using the altitudes determined with IRI-2016 and NRLMSISE-00.

Similar analysis is done by taking a horizontal cut in the Southern Hemisphere and at 31.8° S, the zenith latitude at El Leoncito, then taking the conjugate cut at Villa de Leyva. I started by using the same altitudes that gave the smallest offset in Figure 5.8 and also tried a variety of other combinations. Three altitude combinations are shown in Figure 5.9. This depletion is the same as the one in Figure 5.7 and Figure 5.8, the depletion to the west of zenith at El Leoncito that contains the asterisk at higher latitudes. The left panel of Figure 5.9 uses the same altitudes as the right panel in 5.8, 350 km at El Leoncito and 250 km at Villa de Leyva. Although this combination removed the offset between the depletions at the previous latitude, at the new latitude they are offset. Offsets are reduced when using 250 km and 280 km altitudes at El Leoncito and 250 km at Villa de Leyva. A 280 km altitude at El Leoncito and 250 km altitude at Villa de Leyva gave the smallest offset of any combination including those not shown here and those with different Villa de Leyva altitudes. This different combination of altitudes implies that the airglow layer is not uniform throughout the field of view. In Figure 5.4 a N-S brightness gradient can be seen at both sites. This is due to the presence of the EIA crest in both images, which are visible as the brightest region in each image. The EIA crest has a higher electron density than the rest of the image and the increased emission can also indicate that the peak of the ionosphere may be lower. A nonuniform altitude throughout the image can impact interpretation of the morphology of ESF airglow depletions.

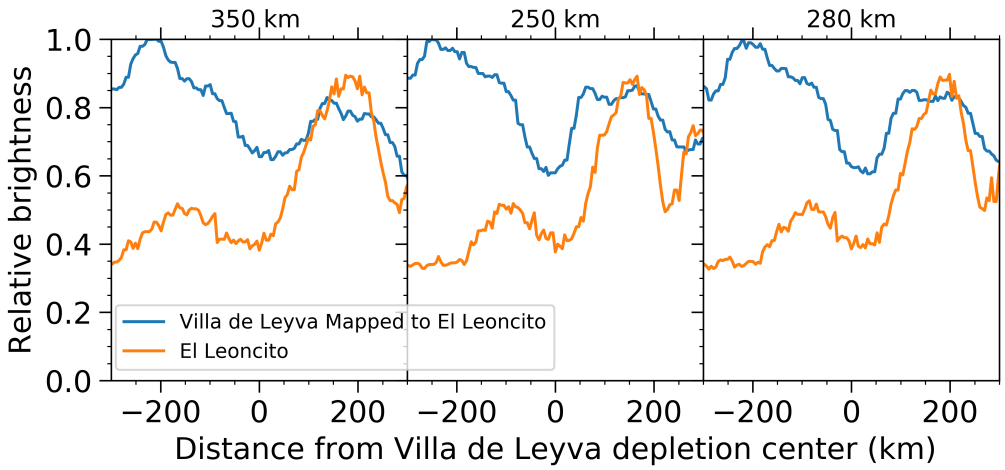

Fig. 5.9: Three plots showing cuts through conjugate depletions visible Figure 5.4, similar to Figure 5.7. The orange line is a cut along a constant geographic latitude at the cross (31.8° S) in the right panel of 5.4 at El Leoncito. The blue line is a cut along the conjugate line and mapped back to El Leoncito. Distances for each cut is measured from the center of the El Leoncito depletion. The El Leoncito image is unwarped at altitudes of 350 km, 250 km, and 280 km and the Villa de Leyva images are all unwarped at 250 km The brightness is much greater at Villa de Leyva so they have been normalized to their respective maxima.

In this section the difference in width of ESF airglow depletions was investigated. I showed that the difference in width is removed by taking a cut through the depletion at El Leoncito and mapping it to Villa de Leyva. Thus, the difference in width is due to variations in the magnitude and morphology of the Earth's magnetic field between the two sites. The initial altitudes determined using IRI-2016 and NRLMSISE-00, 220 km at Villa de Leyva and 260 km at El Leoncito, gave a small offset between the depletions but this could be removed using a different combination of altitudes that still matched the widths, 250 km at Villa de Leyva and 350 km at El Leoncito. This showed that the altitude of emission is likely higher than the models predicted at both sites. A similar analysis was done at another latitude within the image and a different combination of altitudes was found that removed the offset, 250 km at Villa de Leyva and 280 km at El Leoncito. This indicates that the airglow emission

altitude is not constant throughout the image. This can impact the interpretation of data collected with ASIs near the EIA crests or other strong airglow gradients.

5.3 Latitudinal Extent of Airglow Depletions

The different geomagnetic, ionospheric, and thermospheric conditions at conjugate sites can impact the morphology of airglow depletions beyond just their width. Differences in the latitudinal extent of conjugate airglow depletions at Villa de Leyva and El Leoncito along with large differences in airglow brightness have been observed. To measure the latitudinal extent of airglow depletions I use the geomagnetic apex altitudes of the field lines that the depletions intersect. The apex altitude is the altitude at which a geomagnetic field line crosses the magnetic equator. Using apex altitudes removes the need for a geomagnetic coordinate system and only requires an accurate model of the Earth's magnetic field. I use the IGRF-12 model to trace field lines at the airglow emission altitude to the magnetic equator to determine magnetic apex altitude. Since these airglow features are flux tube sampling the foot-point of a depleted flux tube, it is expected that an ESF plume will be connected to depleted airglow features in both hemispheres and that the depletions will share the same maximum geomagnetic apex altitude. I have found that the observations do not always support this assumption. In this section, I compare the latitudinal extent of depletions associated with ESF at Villa de Leyva and El Leoncito.

5.3.1 ASI Observations and Analysis

Figure 5.10 shows a series of six images taken on 29 Nov 2014, a geomagnetically quiet night, with the Villa de Leyva ASI. Black lines marked with numbers show lines of constant magnetic apex altitude at 500 km, 700 km, 900 km, and 1100 km in order to show the extent of the depletions. These are not all consecutive images, six

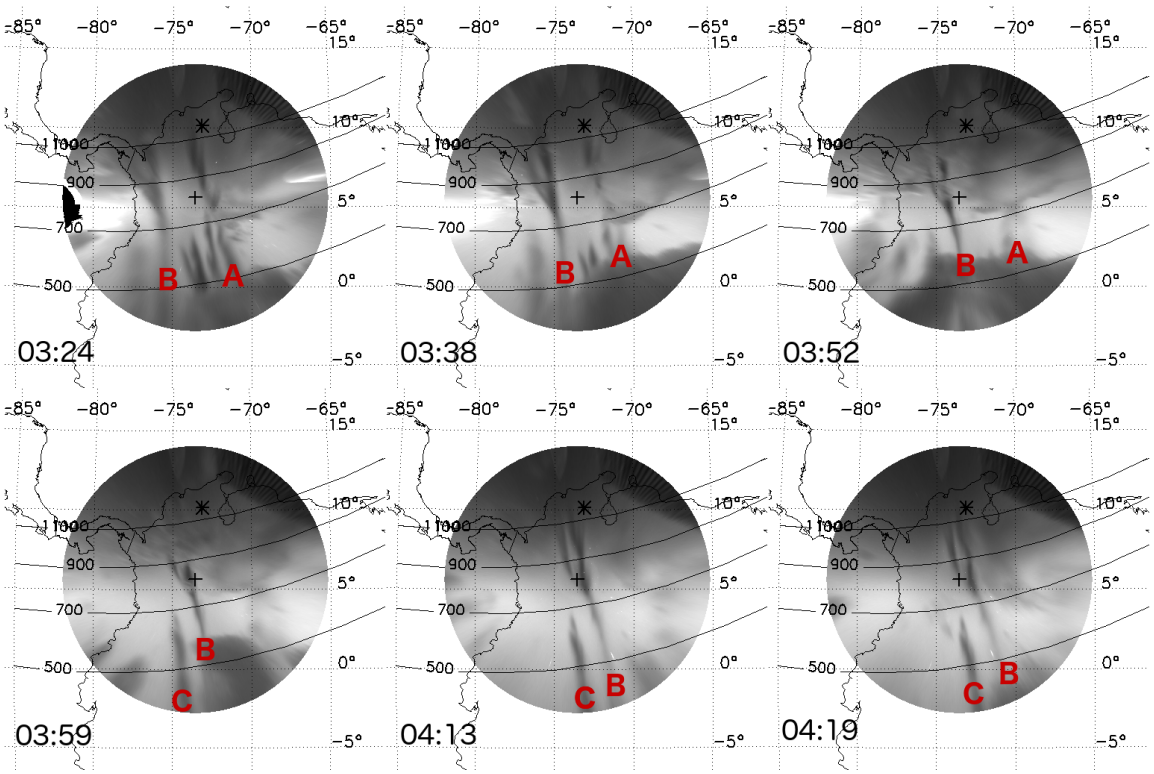

Fig. 5.10: Six 6300 Å images from Villa de Leyva on 29 Nov 2014 unwarped at an altitude of 240 km. These images are not calibrated to emission in rayleighs. The Universal Time for each image is marked in the lower left corner. Airglow depletions are observed as dark structures extending from the south towards the north. Three prominent depletions are marked with the letters A, B, and C and are tracked through the images. Clouds are visible in each image and sometimes obfuscate an entire depletion. The cross is the location of the ASI and the asterisk is the location of the conjugate point of the El Leoncito ASI.

images have been chosen in this time frame to show the depletions associated with ESF. Airglow depletions are visible as dark structures extending from the south to the north. As the night progresses, the depletions drift to the east. Three prominent depletions that can be observed in multiple images are identified with the letters A, B,and C. The top three images show the moon in the field of view to the west.

Figure 5.11 shows images from the same night, 29 Nov 2014, at El Leoncito. These images have been unwarped at an altitude of 300 km and as done in Figure 5.10 black lines show constant magnetic apex altitude at 500 km, 700 km, 900 km,

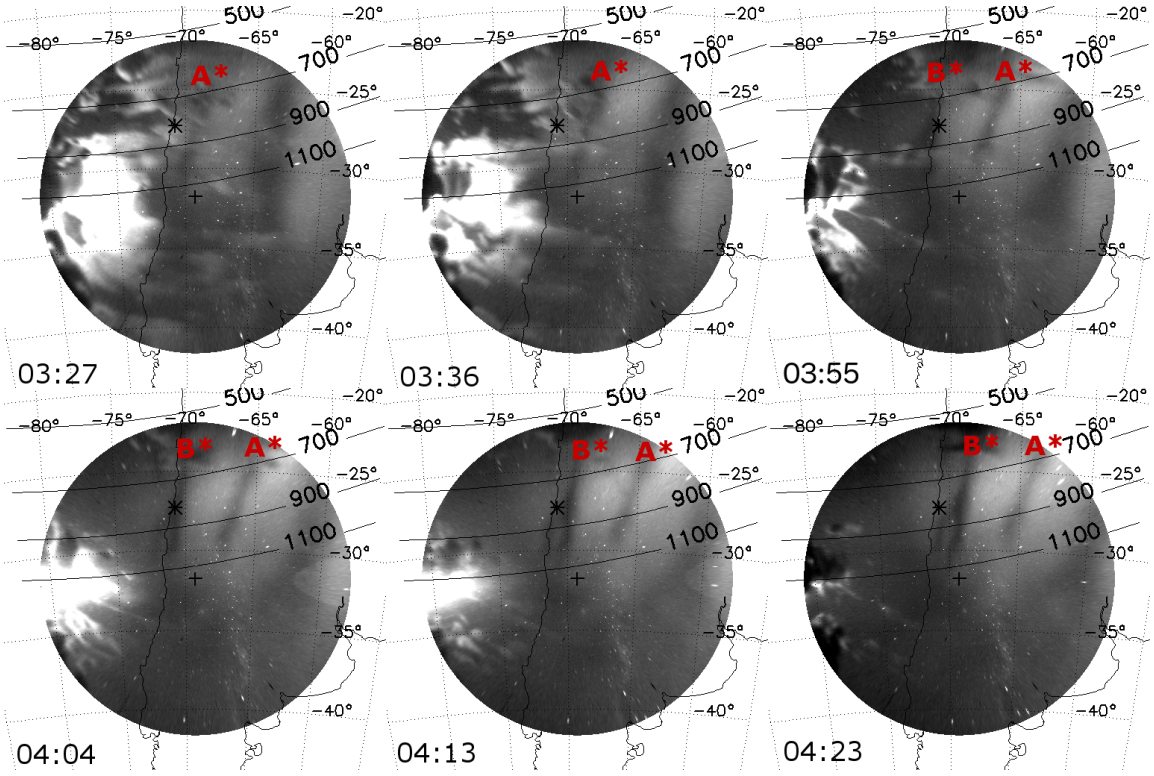

Fig. 5.11: Six 6300 Å images from El Leoncito on 29 Nov 2014 unwarped at an altitude of 300 km. These images are not calibrated to emission in rayleighs. The Universal Time for each image is marked in the lower left corner. Airglow depletions are observed as dark structures extending from the north towards the south. The depletions visible are conjugate to those in Figure 5.10 and share the same letter but with an asterisk such that depletion A* is conjugate to depletion A. Clouds are visible in each image and sometimes obfuscate an entire depletion. The cross is the location of the ASI and the asterisk is the location of the conjugate point of the Villa de Leyva ASI.

and 1100 km. Depletions that are conjugate to those in Figure 5.10 are shown with the same letter with an asterisk. Depletion C, observed at Villa de Leyva, does not reach the FOV at El Leoncito.

Figures 5.10 and 5.11 show that the depletions at Villa de Leyva appear to reach higher magnetic apex altitudes than the conjugate depletions at El Leoncito. Depletions A and B at Villa de Leyva both extend beyond a magnetic apex altitude of 1100 km while at El Leoncito the conjugate depletions, A* and B*, do not reach that

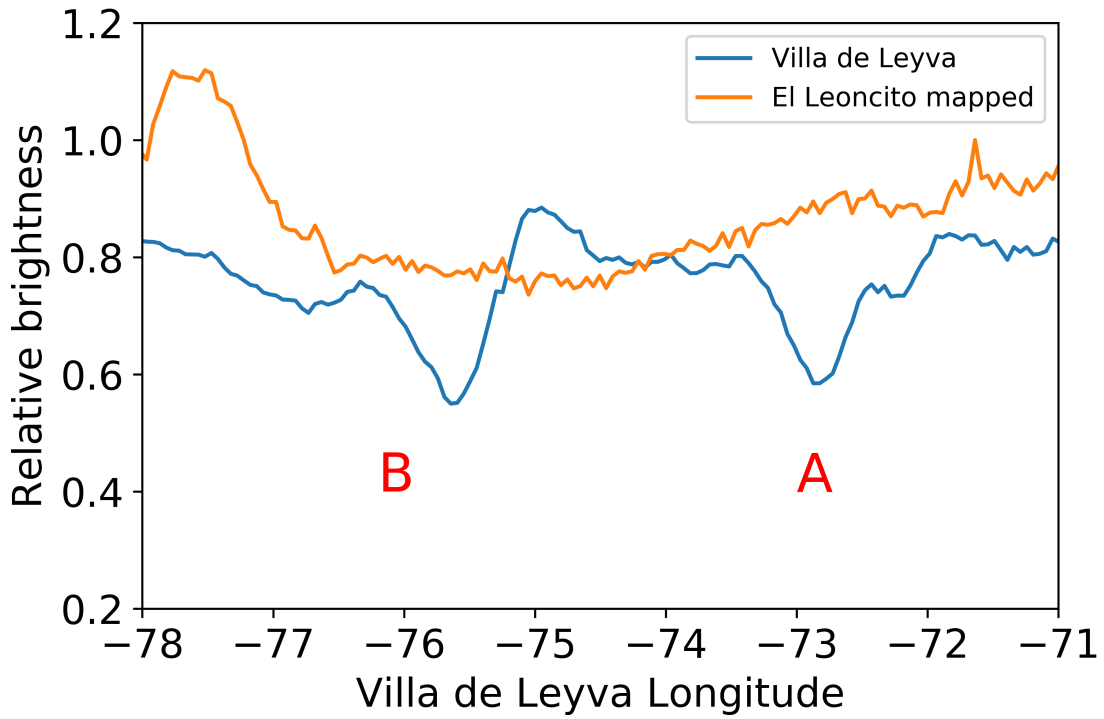

Fig. 5.12: A plot of relative brightness on the y axis and Villa de Leyva longitude on the x axis. The blue line is a cut from Villa de Leyva at 03:38 UT a constant geographic latitude of 8.5° N. Depletions A and B are marked on the plot. The orange line is a conjugate cut at El Leoncito that has been mapped along magnetic field lines to the Villa de Leyva coordinate system.he El Leoncito cut is at 03:55 UT, the closest time that is clear enough that two depletions are visible in the image.

apex altitude. In order to better determine the extent of these depletions, conjugate cuts are taken through the images. First, a cut is taken in the Villa de Leyva image at a constant geographic latitude of 8.5° N. The conjugate location for every point along the line has been computed using IGRF-12 to create a conjugate curve at El Leoncito. Figure 5.12 shows the brightness values from these lines in the images. Data from Villa de Leyva at 03:38 is shown in blue and data from El Leoncito is shown in orange and is mapped along magnetic field lines back to the northern hemisphere in order to display it in the same coordinates as Villa de Leyva. The values from El Leoncito are at a slightly later time, 03:55 UT, to avoid clouds. The data have been normalized

to the maximum value along the line since they from uncalibrated images. At Villa de Leyva depletions A and B are both visible. The conjugate curve at El Leoncito does not show any depletions. The increase in brightness to the left at El Leoncito is due to clouds. I next present concurrent images from 04:13 where only depletion B is visible at both sites.

Figure 5.13 shows concurrent images from Villa de Leyva (left) and El Leoncito (right) on 29 Nov 2014 at 04:13 UT. Horizontal red lines in the left panel show the location of the cuts that are used to examine the depletions in more detail. At Villa de Leyva depletion B extends past 1100 km apex altitude and bifurcates near zenith. At El Leoncito depletion B* extends from the top of the image to about 1000 km apex altitude and bifurcates near the asterisk.

The pair of images in Figure 5.13 show that depletion B has a similar morphology to B*, but their latitudinal extents are different. A visual comparison between the two images shows that the airglow depletions at Villa de Leyva seem to extend to higher apex altitudes than those at El Leoncito.

In these images the contrast can impact the visibility of the features. To better analyze the extent I plot the brightness values along a line in the image. This is first done at Villa de Leyva at a constant geographic latitude of 9° N. This is the northernmost horizontal red line in Fig 5.13 (left). Figure 5.14 shows the brightness values along the red line in the image as a blue line in the plot. The x-axis is the Villa de Leyva longitude and the y-axis is the normalized brightness. The conjugate location for every point along the cut has been computed using IGRF-12 to create a conjugate curve at El Leoncito. The southernmost curved red line in Fig 5.13 (right) is the location of this conjugate line. The normalized brightness from along the curve at El Leoncito is shown as the orange line in Figure 5.14 and is mapped

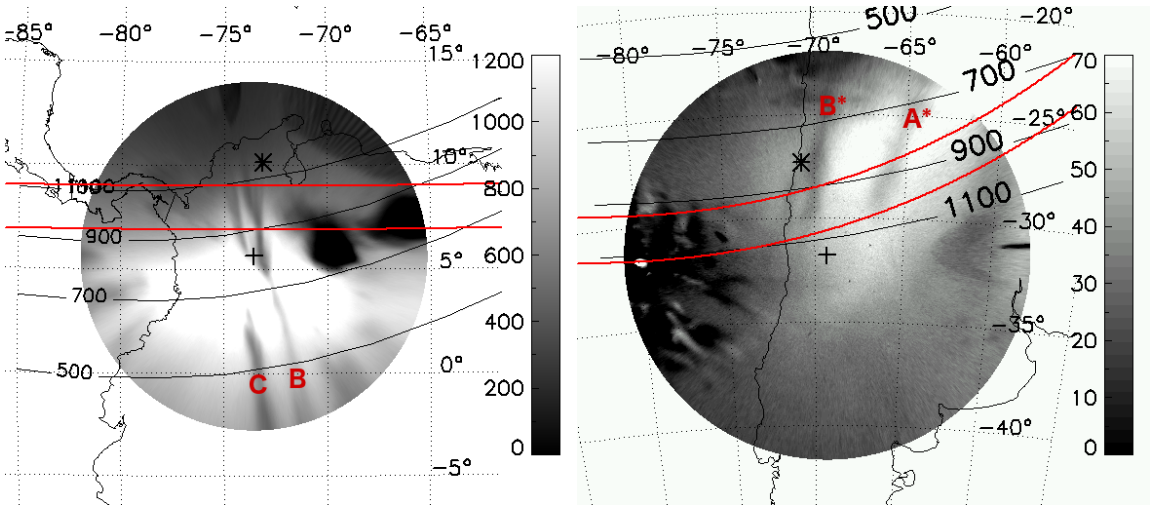

Fig. 5.13: (left) A 6300 Å image taken with the Villa de Leyva ASI at 04:13 UT on 29 Nov 2014. It has been unwarped at an altitude of 240 km. The cross is the location of the ASI and the asterisk is the location of the conjugate point of the El Leoncito ASI. The red lines are the location of cuts through the image at a constant geographic latitude of 9° N and 7° N. In each figure the solid black lines marked with numbers are lines of constant magnetic apex altitude with the altitude at the magnetic equator given in km. The gray scale associated with each image shows the emission in rayleighs. The red letters mark the different depletions. Depletion B in each image are conjugate structures. (right) A 6300 Å image taken with the El Leoncito ASI at 04:13 UT on 29 Nov 2014. It has been unwarped at an altitude of 300 km. The cross is the location of the ASI and the asterisk is the location of the conjugate point of the El Leoncito ASI. The curved red lines that are the conjugate cuts of the cuts at 9° N and 7° N in the left image.

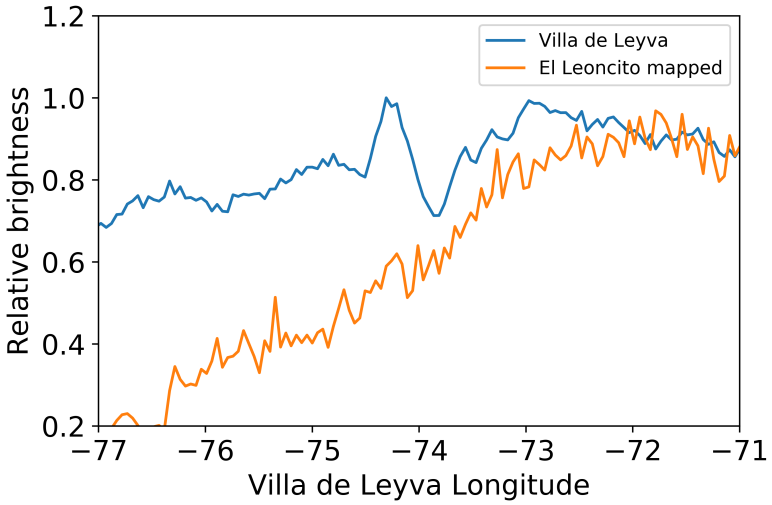

Fig. 5.14: A plot of relative brightness on the y axis and Villa de Leyva longitude on the x axis. The blue line is a cut from Villa de Leyva at a constant geographic latitude of 9° N. The orange line is a conjugate cut at El Leoncito that has been mapped along magnetic field lines to the Villa de Leyva coordinate system. Two depletions are visible at Villa de Leyva around -74 ° and -75 °. No depletions are visible at El Leoncito.

along magnetic field lines back to the northern hemisphere in order to display it in the same coordinates as Villa de Leyva.

At Villa de Leyva (blue, Figure 5.14) two decreases in brightness around -74 ° and -74.5 ° longitude are visible. These are two portions of depletion B above where it has bifurcated. The eastern branch is about 30% dimmer than the background emission of about 550 R at this latitude. The western edge of the branch to the west is not as prominent due to weaker background airglow emission. The El Leoncito airglow emission (orange) is much lower, a maximum of about 70 R, so the background has larger relative fluctuations of about 10% that correspond to about 7 rayleighs. There are no decreases in brightness at El Leoncito that indicate the presence of a depletion. These two conjugate cuts show that although the depletions reach over 1100 km at Villa de Leyva they do not extend that far at El Leoncito.

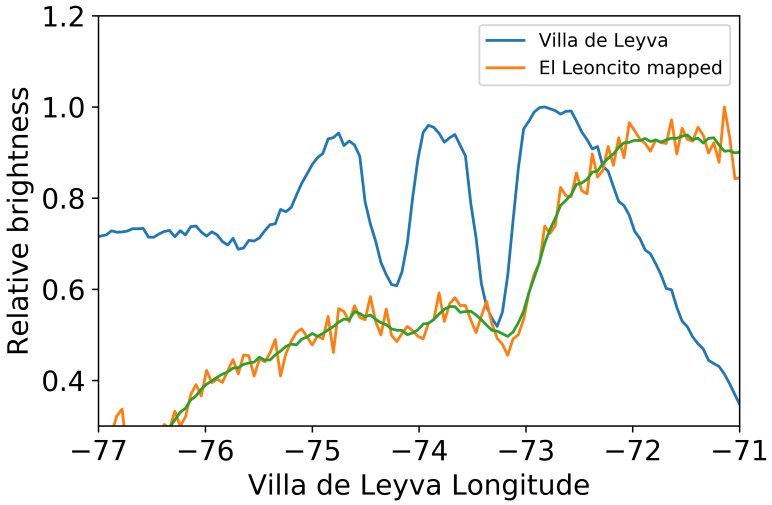

Fig. 5.15: A plot of relative brightness on the y axis and Villa de Leyva longitude on the x axis. The blue line is brightness from Villa de Leyva at a constant geographic latitude of 7° N, the southernmost red line in Figure 5.13 (left). The orange line is brightness from a conjugate line at El Leoncito, the northernmost red line in Figure 5.13 (right), that has been mapped along magnetic field lines to the Villa de Leyva coordinate system. The green line is a running average of 7 pixels to make the depletions more clearly visible. Two depletions are visible at Villa de Leyva and El Leoncito between -73 ° and -75 °.

For comparison, I show a another set of conjugate cuts from the same images in Figure 5.13 where depletions are visible at both sites in Figure 5.15. For this plot brightness values shown in blue are taken above the bifurcation point at a constant latitude of 7° N at Villa de Leyva. In Figure 5.13 (left) this is the southernmost red line. As in Figure 5.14, the brightness values from the conjugate line at El Leoncito, the northernmost red line in Figure 5.13 (right), are shown in orange. The green line is a running average of 7 pixels to make the depletions more clearly visible. These cuts are at an apex altitude of around 950 km near depletion B. Like Figure 5.14, two decreases in brightness, corresponding to two portions of depletion B, are visible at Villa de Leyva between -73 ° and -75 °. They are 40% and 50% dimmer than the 1100

R background at this latitude. Unlike Figure 5.14, two decreases in brightness are now visible at El Leoncito as well. By examining more slices through the image I am able to determine the difference in extent between the two sites. On this November night, the depletions at Villa de Leyva extend to magnetic apex altitudes that are about 150 km higher than those at El Leoncito.

In Section 5.2 I discussed how the altitude of emission can affect the width and offset of the airglow depletions. The altitude of emission can also change the extent of the depletions. An analysis using multiple combinations of altitudes was done to determine how that affects the apex altitude. In order for the apex altitudes to match, El Leoncito would have to be unwarped at an altitude 200 km higher than the altitude at Villa de Leyva, which is an unrealistic situation. The calculated altitudes of emission are not the source of the difference in latitudinal extent.

In addition to the difference in depletion extent between the two sites, there is also a large difference in 6300 Å emission. It is possible that the weaker emission at El Leoncito makes the detection of the tip of the depletions more difficult. The background emission of the El Leoncito images near the depletions does not change by more than a few rayleighs between the two cuts at El Leoncito. Additionally, the brightness gradient from north to south does not begin to decrease significantly until past the 1100 km apex altitude. The brightness gradients that are observed can be a result of changes in electron density or changes in the height of the F layer since 6300 Å emission is sensitive to both of these. 7774 Å emission, which peaks around 50 km above the peak 6300 Å altitude, is proportional to the electron density and does not depend on the altitude of the F layer. By analyzing 7774 Å images as well I gain vertical spatial information and can determine whether or not the difference in extent is simply due to observational limitations of 6300 Å. Figure 5.16 shows images taken in 7774 Å just a few minutes after the 6300 Å images in Figure 5.13. Contrast has

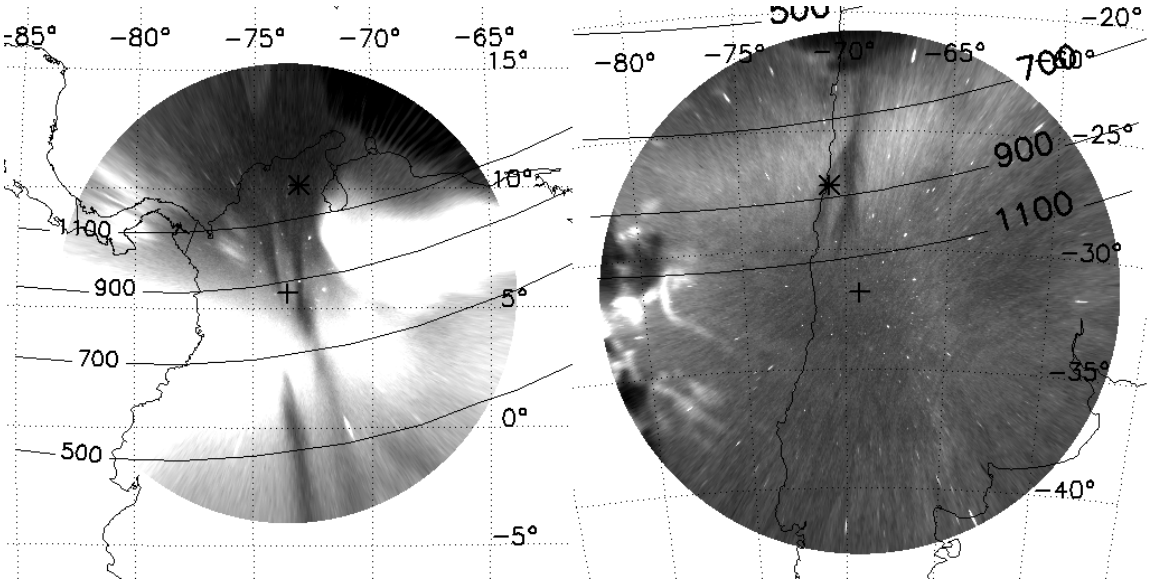

Fig. 5.16: (left) A 7774 Å image taken with the Villa de Leyva ASI at 04:15 UT on 29 Nov 2014. The cross is the location of the ASI and the asterisk is the location of the conjugate point of the El Leoncito ASI. It is has been unwarped at 290 km. In each figure the solid black lines marked with numbers are lines of constant magnetic apex altitude with the altitude at the magnetic equator given in km. These images have not been calibrated to absolute brightness (right) A 7774 Å image taken with the El Leoncito ASI at 04:16 UT on 29 Nov 2014. The cross is the location of the ASI and the asterisk is the location of the conjugate point of the El Leoncito ASI. It has been unwarped at 350 km.

been enhanced to show the edge of the airglow depletions. Apex altitudes are show as black lines in both of these images. The brighter bands around 700 km apex altitude at both sites are the crests of the EIA. At Villa de Leyva (left) the airglow depletion extends beyond 1100 km while at the same time the airglow depletion at El Leoncito does not reach 1100 km. The same difference in latitudinal extent that was observed in the 6300 Å images (Figure 5.13) is also observed in the 7774Å images (Figure 5.16). This means that the difference in latitudinal extent is not due to limitations in detectability at 6300 Å. Additionally, the brightness gradient at El Leoncito near 1100 km apex altitude and the sharp edges observed in the depletion indicate that there is not a significant decrease in 7774 Å that would cause the end of the depletions

fade into the background. The difference in extent is not an observational limitation, it is a real difference in the depletions between the two sites.

The low levels of emission at El Leoncito are not affecting the detectability of the latitudinal extent of the depletions but the difference in brightness between the two sites may offer some insight into why the depletions are different. Differences in the background emission at two conjugate sites is a regular occurrence. The gray scale next to each image in Figure 5.13 shows that on 29 Nov 2014 the background 6300 Å emission is greater at Villa de Leyva than at El Leoncito by a factor of about 15.

5.3.2 Airglow Model

Figures 5.13 and 5.16 show bright airglow emission at Villa de Leyva and significantly weaker airglow emission at El Leoncito. In order to assess the difference in 6300 Å emission between the two sites I analyze modeled emission profiles from the BU airglow model. Inputs for the model are taken from IRI-2016 and NRLMSISE-00 since there are not in-situ measurements of the densities at these sites. 6300 Å emission profiles from both sites are shown in Figure 5.17. The blue curve shows that the peak emission altitude at El Leoncito is at 300 km, which is the altitude used to unwarp the image in Figure 5.13 (right). The maximum volume emission rate is about 6 photons/cm^3/s. At Villa de Leyva the peak emission altitude is lower, 240 km, and that is the altitude that the image in Figure 5.13 (left) is unwarped at. The maximum volume emission rate at Villa de Leyva is greater, about 16 photons/cm^3/s. Both of models were run using parameters at zenith at the respective sites. At El Leoncito, the model outputs are a brightness of 72 rayleighs and at Villa de Leyva, the model results in a brightness of 170 rayleighs. The measurements at El Leoncito show that the background at zenith is about 70 rayleighs, very similar to the model

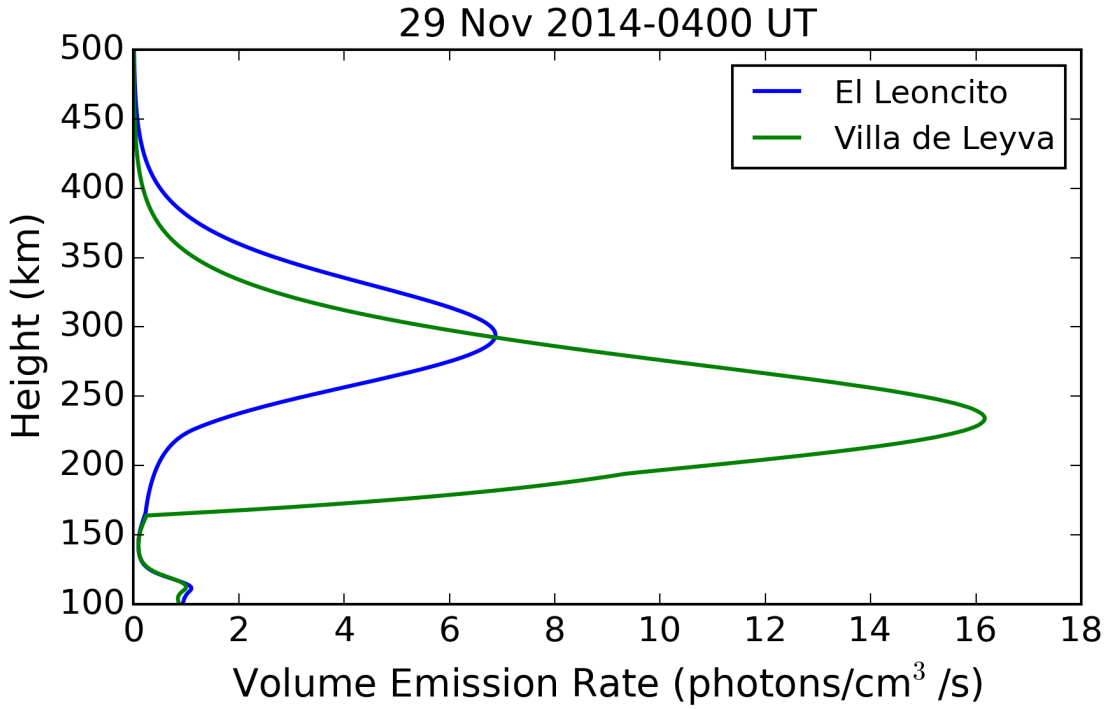

Fig. 5.17: Emission profiles showing volume emission rate on the x-axis and altitude on the y-axis. The blue line is from El Leoncito and the green line is Villa de Leyva. These profiles are determined using the BU Airglow model with inputs from IRI and NRLMSISE. Integration over these curves in altitude gives the brightness in rayleighs.

results. At Villa de Leyva, the background at zenith is around 1200 rayleighs, seven times greater than the model results.

Figure 5.18 shows altitude profiles of electron densities at both sites that I introduce to explain the differences in the modeled emission profiles. At Villa de Leyva the F-layer peak is at a lower altitude and the consequence is increased 6300 Å emission. The peak electron density at El Leoncito is actually greater but since it is at a higher altitude the overall emission is lower. This modeled electron density gives a greater emission at Villa de Leyva, consistent with the data, but underestimates the difference. Without a measured density profile to compare with the modeled

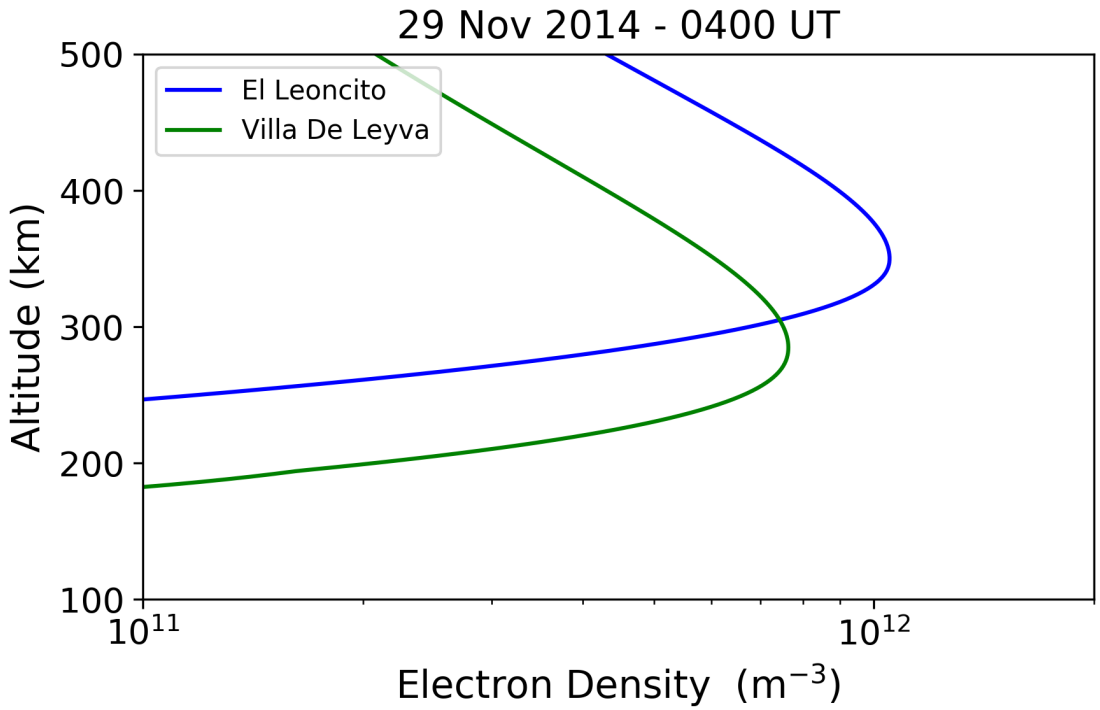

Fig. 5.18: Electron density profiles from IRI. The blue line is at El Leoncito and the green line is at Villa de Leyva. Both profiles are at 04:00 UT on 29 Nov 2014.

results, measured TEC can be used to give some insight into the difference. IRI not only provides the density profile but also TEC. At El Leoncito, the modeled TEC is 19 TECU. Measurements from that area, using the El Leoncito station from LISN, are about 20 TECU. For El Leoncito the model and the measurements agree quite well which is expected since the modeled rayleighs brightness is very similar to the measured value. At Villa de Leyva the modeled TEC is 12 TECU, smaller than at El Leoncito due to the smaller peak density as seen in Figure 5.18. Measurements from the Bogota GPS receiver from LISN indicate that the TEC is around 80 TECU, more than six times greater than the modeled TEC. This ratio of measured and modeled TEC ($\sim$6.6) is similar to ratio of measured and modeled emission ($\sim$ 7) and thus

accounts for most of the discrepancy between the modeled emission (170 R) and the measured emission (1200 R).

The combination of ASI observations, modeled emission, and measured TEC provides some insight into the background conditions that can affect the depletions associated with equatorial spread F. The large TEC values at Villa de Leyva and the greater brightness indicate that there is more plasma over Villa de Leyva than there is over El Leoncito. The model results show greater emission at Villa de Leyva but it is due to a lower F-layer since the modeled TEC is actually smaller than at El Leoncito. Combining these techniques shows that at Villa de Leyva there is more plasma and the peak is at a lower altitude which together creates a much greater background emission than at El Leoncito.

5.3.3 Neutral Winds

Neutral meridional winds have been previously shown to impact plasma distribution around the magnetic equator (*Rishbeth*, 1972). These winds can move plasma up or down in altitude. The ions will be dragged by ion-neutral collisions but the presence of the magnetic field will influence how they move. In the southern hemisphere a northward wind will cause the ions to move up in altitude and a southward wind will cause them to move down in altitude. In the northern hemisphere a northward wind will move the ions down in altitude and a southward wind will cause them to move up in altitude. Meridional winds that are in the same direction in both hemispheres have been shown to modify equatorial plasma distribution (e.g., *Krall et al.*, 2009b). A northward meridional wind can move plasma from south to north and push the northern crest of the EIA downward. Figure 5.19 shows model results of the meridional wind from Horizontal Wind Model 14 (HWM14) every two hours during the time of year and conditions present in Figure 5.13. The blue triangles show that throughout the night at El Leoncito there is a strong northward

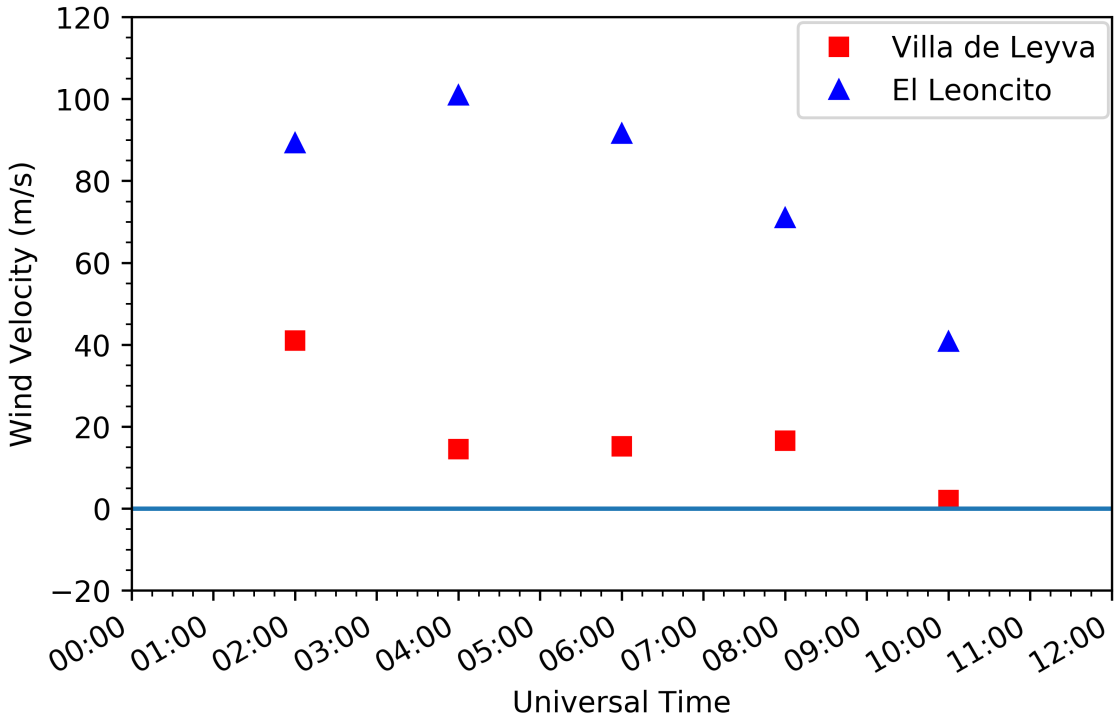

Fig. 5.19: Outputs from HWM14 showing meridional winds during on 29 November 2014. The red squares are at Villa de Leyva and the blue triangles are at El Leoncito. Positive velocity is northward.

wind. The red squares show that there is a northward wind at Villa de Leyva as well, although it is not as strong. This model shows that on this night a northward wind is occurring at both sites. It has been shown before that an interhemispheric wind can increase the plasma density and lower the peak of the F-layer in the hemisphere where the wind is poleward (*Krall et al.*, 2009b) HWM-14 is an empirical model so it is not expected to reproduce the exact conditions for this night but it is good for assessing the average case. Although there may be some other factors at play, the neutral meridional wind is likely the major cause of the difference in emission altitude, brightness, and TEC between the two sites.

On this night when the meridional winds are northward, the airglow is brighter and the depletions are extended in the northern hemisphere. Interhemispheric winds

are known to increase electron density and thus airglow emission in the hemisphere that the winds poleward. It also appears that the meridional winds may also be responsible for the extended depletions at Villa de Leyva. Previous work has been done on the relationship between neutral winds and plasma distribution, and the relationship between neutral winds and the onset of ESF (*Huba and Krall*, 2013) but asymmetries in the latitudinal extent of airglow depletions due to meridional winds has not been studied before. Although the latitudinal extent has not been investigated, *Krall et al.* (2009a) did model asymmetries in brightness of airglow depletions associated with ESF. This paper modeled the depletions shown in *Martinis et al.* (2009) where an airglow depletion became an airglow enhancement. A follow up study by *Park et al.* (2016) further confirmed that the airglow enhancement was only present in one hemisphere. Additionally, in Section 4.7 I showed an ESF enhancement that only occurred in one hemisphere. In these studies the consensus was that a northward neutral wind can lead to asymmetric north-south density profiles inside and outside of an ESF plume which ultimately lead to the ESF structures becoming an enhancement in the northern hemisphere. Since neutral winds can modify ESF depletions in one hemisphere to create an enhancement and the other hemisphere is unaffected, it seems reasonable that these winds can modify the overall structure of depletions by extending them in the hemisphere where the meridional winds are poleward.

I presented in this section conjugate observations of ESF depletions at El Leoncito and Villa de Leyva. Consistent results indicate that a) the depletions at Villa de Leyva extend to higher apex altitudes than they do at El Leoncito and b) at the same time the background airglow brightness is much greater at Villa de Leyva. Concurrent TEC measurements from GPS receivers showed that TEC was much greater at Villa de Leyva. BU Airglow model outputs using IRI indicate that

the airglow layer at Villa de Leyva is lower than at El Leoncito. HWM14 results shows a northward wind at both sites. This northward wind is the most probable cause for the higher TEC and lower airglow layer at Villa de Leyva. This wind is in the same direction as the extended depletion at Villa de Leyva and is the most likely explanation for the difference in depletion extent.

5.4 Velocity of ESF depletions

In the previous sections I analyzed differences in the morphology of airglow depletions associated with ESF at conjugate locations. In this section I investigate differences in the zonal velocities of these depletions between conjugate sites.

Three dates are used to compare the zonal velocity of depletions at Villa de Leyva and El Leoncito: 12 Jan 2015, 10 Mar 2015, and 13 Sep 2015. These dates were selected because the skies were clear enough to make a measurement and they are from different times of the year. As described earlier in the chapter, for each date I determine an altitude of emission at each site and unwarp the images at that altitude. Figure 5.20 shows an example of conjugate depletions from 10 Mar 2015. In these images the Villa de Leyva image (left) has been unwarped at an altitude of 230 km and the El Leoncito image (right) has been unwarped at an altitude of 250 km. This altitude is used for the entire time that the velocity is measured. Two depletions are visible at each site. Although not shown here, the images from the other two nights have at least one depletion and sometimes multiple depletions. For 12 Jan 2015 the Villa de Leyva images are unwarped at an altitude of 240 km and the El Leoncito images are unwarped at 300 km. For 13 Sep 2015 the Villa de Leyva images are unwarped at 250 km and the El Leoncito images have been unwarped at 260 km. These altitudes have be calculated using the BU Airglow model with NRLMSISE-00 and IRI-2016 as inputs.

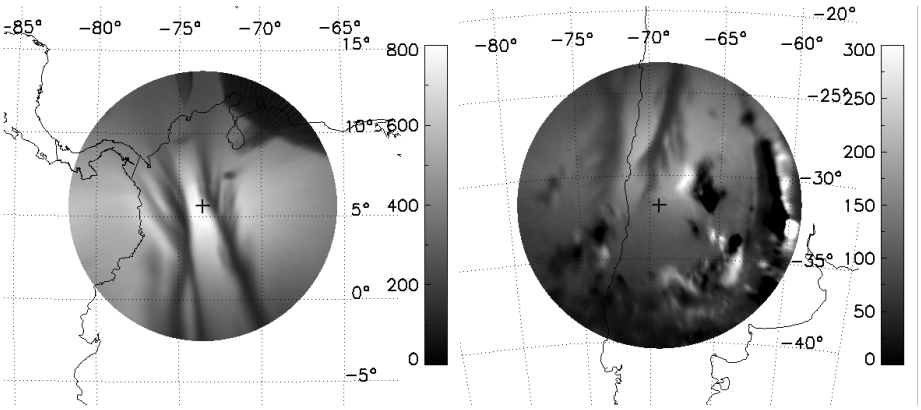

Fig. 5.20: (left) A 6300 Å image taken with the Villa de Leyva ASI at 02:06 UT on 10 Mar 2015. The cross is the location of the ASI. It has been unwarped at an altitude of 230 km. (right) A 6300 Å image taken with the El Leoncito ASI at 02:06 UT on 10 Mar 2015. The cross is the location of the ASI. It has been unwarped at an altitude of 250 km.

To determine the velocity, depletions are tracked through multiple images as they move from west to east. The center of a depletion is determined in each image and the location is recorded. If there are multiple depletions in the field of view then this is done for each depletion. The distance traveled between images is calculated using the difference in position. The images are time stamped at one second of precision. The zonal velocity is the change in position divided by the change time. Figure 5.21 shows the velocity as a function of Universal Time for the three nights mentioned earlier. Velocities from Villa de Leyva are shown in orange and velocities from El Leoncito are shown in blue. Vertical bars show the error in the determination of the velocity. There are two main sources of error for the velocities. The first source of error is due to emission altitude. For a given image, the higher the assumed emission altitude, the larger the velocity. This is because the same image is projected onto a larger area and the distance the depletion travels between two images will increase. The error here is calculated using an altitude uncertainty of $\pm$ 25 km. The other source of error is in determining the center of the depletion. For these velocities

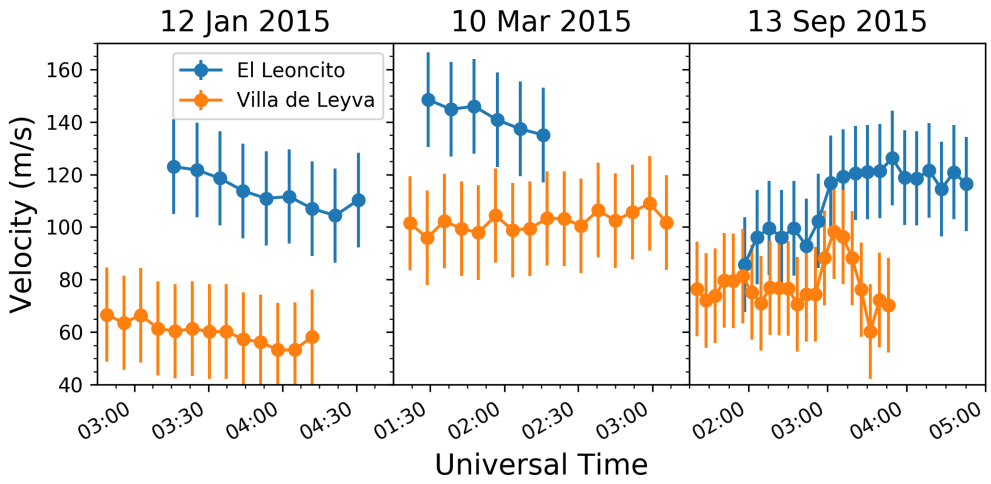

Fig. 5.21: Three plots with zonal velocity on the y-axis and Universal Time on the x-axis. In each plot velocities from Villa de Leyva in are in orange and El Leoncito is in blue. The y-axis covers the same range of velocities for each plot. The panels show three different nights:(left) 12 Jan 2015, (middle) 10 Mar 2015, and (right) 13 sep 2015.

the error assumes that the center of the depletion can be determined within ± 8 km. These to sources of error result in an error in the velocity determination of ~ 20 m/s. Each night presented in 5.21 shows that the velocities at El Leoncito are consistently higher than those at Villa de Leyva.

In addition to the velocity differences at Villa de Leyva and El Leoncito, differences at other conjugate sites have been observed. Figure 5.22 shows zonal velocities of airglow plasma depletions measured at the Arecibo observatory and its conjugate location in Mercedes, Argentina (*Martinis et al. in prep*). In this figure higher velocites are also observed in the Southern Hemisphere. The difference in velocity is similar to the differences observed at El Leoncito and Villa de Leyva.

As discussed in Section 5.2, a major difference between the two ASI sites, El Leoncito and Villa de Leyva, is that the magnetic field at El Leoncito is significantly weaker than at the conjugate location at Villa de Leyva. This is because El Leoncito

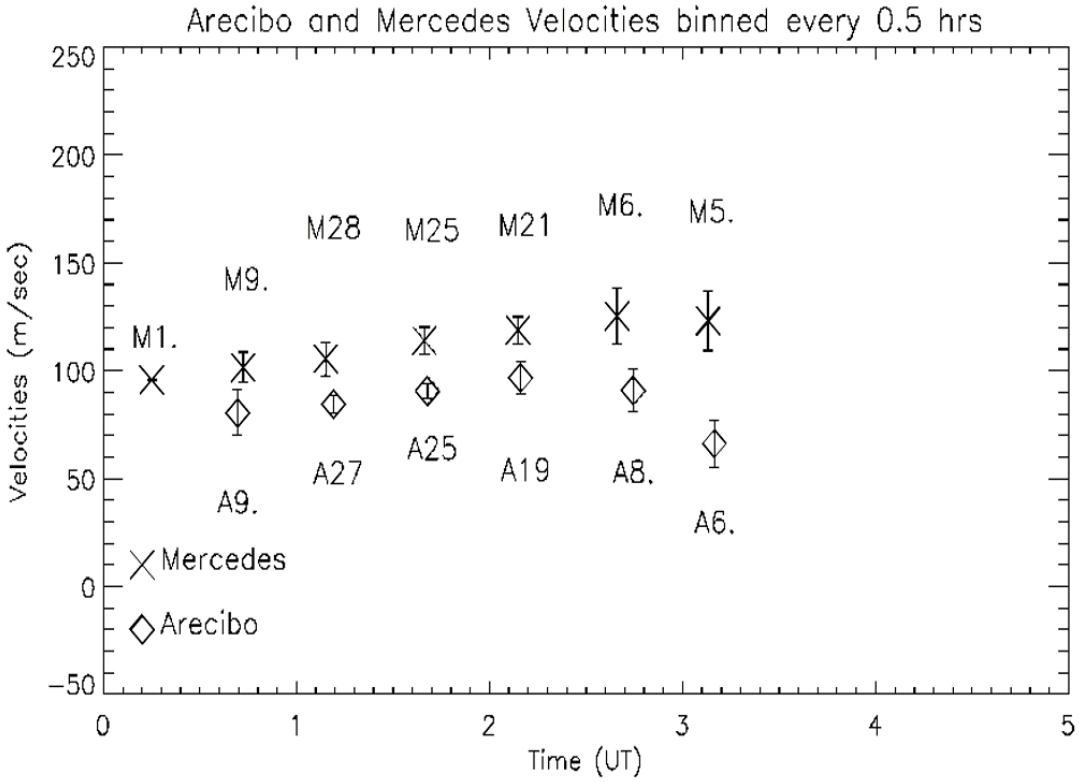

Fig. 5.22: Zonal velocities from conjugate locations at Arecibo, Puerto Rico and Mercedes, Argentina. Data were taken during equinox conditions from 2010-2012. The numbers following each letter indicate the number of data points used to obtain the average result.

is near the South Atlantic Anomaly. The zonal drift velocity, and thus the velocity of depletions, depends on the strength of the magnetic field. This difference impacts the zonal plasma drift and thus the velocity of the depletions.

The plasma has a zonal drift due the presence of orthogonal magnetic and electric fields. The zonal velocity is given by the following equation:

$$\mathbf{v} = \frac{\mathbf{E} \times \mathbf{B}}{B^2} \tag{5.1}$$

E is the electric field vector and **B** is the magnetic field of the Earth. The electric field is mainly due to the F-region dynamo given by the following equation:

$$\mathbf{E} = -\mathbf{U} \times \mathbf{B} \tag{5.2}$$

U is the Pedersen conductivity-weighted neutral zonal wind **B** is the magnetic field of the Earth. These equations determine the velocity of the plasma depletions and can be used to determine the ratio of the velocities at the two sites. The magnetic field is easily calculated at both sites. The electric field requires a more complex analysis so I refer to the analysis in *Laundal and Richmond* (2017) regarding electric fields and conjugate velocities. In this paper they discuss various coordinate systems for the Earth's magnetic field. One coordinate system that they discuss is Quasi-Dipole coordinates, a non-orthogonal system that uses IGRF and defines magnetic latitudes and longitudes such that they are constant along field lines. They set up a system of basis vectors that are used to map the electric field along magnetic field lines. Mapping electric fields in this coordinate system allows for **v** to be mapped along field lines as well using Equation 5.1. In their paper they show that the drift velocity can be separated into to components that are constant along magnetic field lines by using their basis vectors. Using this technique they create a map showing the difference in magnetic east velocities between conjugate locations. I have reproduced the relevant section of this map in Figure 5.23. From this map it is expected that the velocities at El Leoncito should be about 1.35 times greater than the velocities at Villa de Leyva. Additionally, the velocities at Mercedes are expected to be about 1.4 times greater than at Arecibo. If the Earth's field was a pure dipole then their model would show no difference in velocity. It also indicates that a portion of the magnetic east velocity at Villa de Leyva translates into about a 10% magnetic meridional velocity at El Leoncito. This ratio of velocities is consistent with our results. The

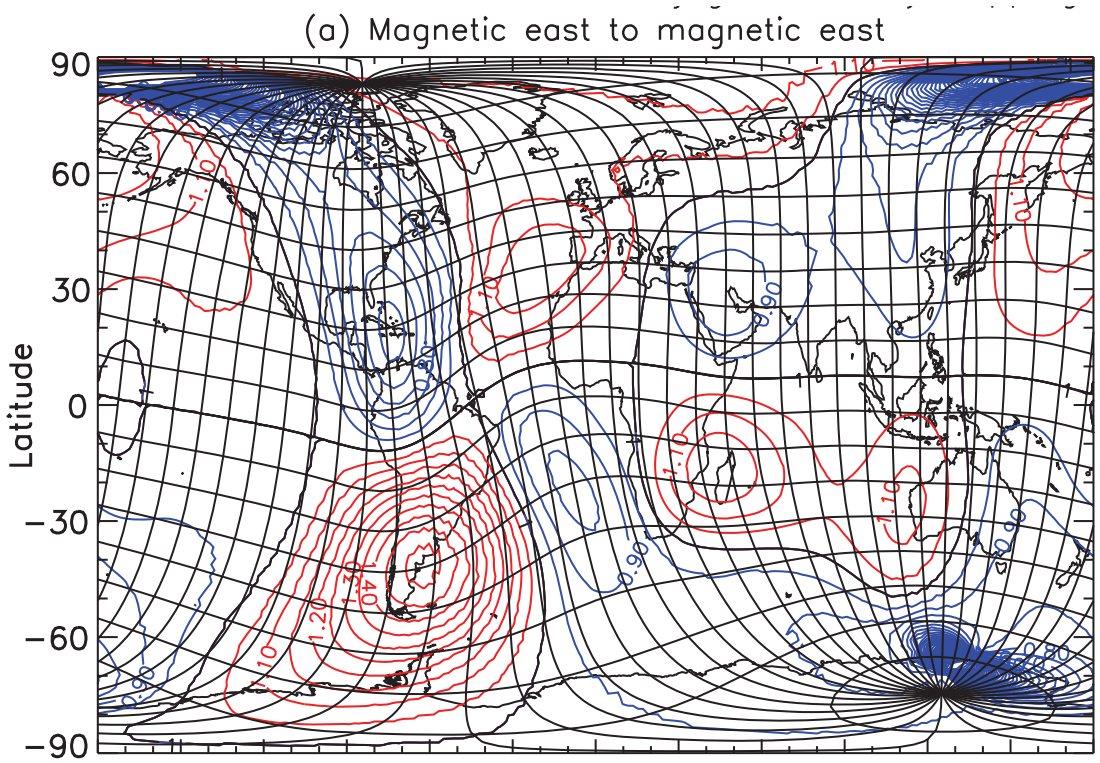

Fig. 5.23: A map of zonal velocity differences between conjugate locations. Blue contours show by what factor the velocity is smaller by compared to the conjugate location. Red contours show the factor the velocity is larger by compared to the conjugate location (*Laundal and Richmond*, 2017).

difference in velocity between the to sites can be explained by the weaker magnetic field in the Southern Hemisphere and the non-dipole nature of the Earth's magnetic field.

In this section I presented measurements of zonal velocities at conjugate sites from three nights: 12 Jan 2015, 10 Mar 2015, and 13 Sep 2015. For each night the zonal velocities were consistently larger at El Leoncito than at Villa de Leyva. The faster velocities are attributed to the weaker magnetic field at El Leoncito. The weaker magnetic field and the orientation of the magnetic field means that there is a smaller zonal ExB drift. The difference in magnetic field is consistent with the difference in measured velocity.

5.5 Summary

In this section I compared the morphology and velocity of depletions associated with ESF. For the morphology, I investigated differences in width and extent. I found that depletions were wider at El Leoncito than at Villa de Leyva. This is due to difference in magnetic field strength and morphology between the two sites. The proximity of the El Leoncito ASI to the South Atlantic Anomaly means the magnetic field is much weaker at this site. When widths are compared with the effects of the magnetic field removed, they are consistent. In this investigation an offset was found between the depletions that can mostly eliminated by some adjustments to the altitudes of emission. This highlights the limitations of using empirical climatological models to determine emission altitude. Different offsets were observed at different latitudes indicating that the airglow emission altitude is not consistent throughout the image, a result that impacts the interpretation of airglow observations. I then compared the latitudinal extent of the depletions at the two sites. In the case presented, the depletions reached higher magnetic apex altitudes at Villa de Leyva than at El Leoncito. Additionally, the brightness is much greater at Villa de Leyva. Both effects were attributed to a northward meridional neutral wind in both hemispheres. This wind is increasing the plasma density, lowering the altitude of emission, and extending the depletions. Finally, zonal velocities of depletions at the two sites are compared. Larger zonal velocities are found at El Leoncito throughout the year. This is attributed to the difference in the $\mathbf{E} \times \mathbf{B}$ zonal plasma drift. The $\mathbf{E} \times \mathbf{B}$ drift is larger at El Leoncito due to the weaker overall magnetic field strength at El Leoncito and the orientation of the Earth's magnetic field. This is the first in depth analysis of conjugate depletions in western South America.

Chapter 6

Summary

In this dissertation I have presented multi-instrument analysis of the midnight temperature maximum and equatorial spread F. Three questions were presented in Chapter 1. I answer those three questions here and summarizes other the other results as well.

6.1 What are the characteristics of the midnight temperature maximum on a global scale?

I addressed this question in Chapter 3 where I presented results from three studies that provide new measurements of the MTM.

In the first study, published in *Martinis et al.* (2013), we used 60 years of ISR ion temperatures to detect and characterize the MTM at the Arecibo observatory in Puerto Rico. The ISR technique measures temperature at multiple altitudes and the MTM was detected in range of altitudes on a given night, up to 467 km. A seasonal analysis of MTM characteristics revealed that the MTM tended to occur earlier and to have larger amplitude during local summer months.

In the second MTM study, published in *Hickey et al.* (2015), multiple instruments in the Northern Hemisphere were used to measure MTM characteristics. We used the steerable ISR at the Millstone Hill Observatory in Massachusetts to expand the detection of the MTM to higher latitudes. The MTM was detected in past observations with concurrent observations at Arecibo and Millstone Hill. New

experiments were run with concurrent measurements at Millstone Hill along with an FPI. We detected the MTM above 30° N with an ISR, a first for this technique. Simultaneous observations from Arecibo ISR during two of the MTM observations indicate that the MTM also occurred during the same time period at lower latitudes (18° N). Larger amplitude and later occurrence time are found at higher latitudes.

In the third MTM study, published in *Hickey et al.* (2018), we compared the timing of a brightness wave observed with the El Leoncito ASI with the timing of the MTM at Jicamarca. The BW occurred later and to the east of Jicamarca at the higher latitudes in a way that is not consistent with an MTM propagating south from a lower latitude, as has been suggested in previous studies.

These three studies presented have further characterized the extent and timing of the MTM on a global scale. Our concurrent multiple latitude observations are not consistent with the theory that the MTM propagates from lower latitudes to higher latitudes. Our interpretation is that the MTM occurs over a range of latitudes and longitudes, making a sideways V-shape, and that the whole structure migrates westward following the apparent motion of the sun. This is the same interpretation that was presented in *Akmaev et al.* (2009). This theory results in the observed later occurrence at higher latitudes and is also consistent with the seasonal variations observed so that the model results from WAM are consistent with all the observations presented here. The concurrent observations of the MTM at multiple latitudes and altitudes presented here support the theory that the MTM is generated by an interaction of atmospheric tides that can be traced to the lower atmosphere (*Akmaev et al.*, 2009) and that the MTM does not propagate from low-latitudes to higher latitudes but instead occurs over a span of latitudes and that the entire structure moves westward.

6.2 What are the characteristics of large-scale (10-500 km) ESF plasma density structures and how do they relate to small-scale (0.3-3 m) density irregularities?

This question is addressed in Chapter 4 and is accompanied by additional analysis of equatorial spread F. In chapter 4 I discussed a variety of ESF observations using ASIs and the new science that has been learned from them. Within this chapter, Sections 4.2, 4.4, 4.5, and 4.6 are published in *Hickey et al.* (2018) and Section 4.3 is published in *Hickey et al.* (2015).

I first showed the capabilities of the ASIs to observe ESF at the magnetic equator and higher latitudes. I showed observations of both bottomside ESF at Jicamarca and topside ESF at El Leoncito and Villa de Leyva and compared these large-scale airglow depletions with the more well known radar observations of ESF. Early in the night when the 6300 Å airglow emission is too weak for ASI observations, only the radar is able to detect ESF via irregularities with 3 m scale sizes. Later in the night, after the small-scale irregularities have dissipated, 'fossilized' large-scale depletions can still be observed.

I modeled the 6300Å airglow emission at Jicamarca using IRI and ISR data as ionospheric inputs and NRLMSISE-00 as thermospheric inputs. The Boston University airglow code found values that are a factor of 2-3 smaller than the measured values. This inconsistency is likely due to contamination from nearby city lights that varies throughout the field of view, throughout the night, and from night to night making it a challenge to accurately account for it. Although the absolute values of the measurements and the model did not match, the model accurately reproduces the trend in the 6300 Å ASI observations when using measured values from the ISR and NRLMSISE-00.

A more in-depth analysis of the comparison between radar systems and the Jicamarca ASI was presented in order to better determine the connection between large-scale airglow depletions associated with ESF and small-scale irregularities. We compared airglow observations with concurrent 50 Mhz and 445 Mhz radar observations and found that there is a higher occurrence of radar echoes coming from regions identified as the western wall of large-scale depletions in comparison with echoes coming from other regions within the depletion. These results suggest that the gradient drift instability is responsible for the at 0.34 m and 3 m radar echoes on the western wall and that the lower-hybrid drift instability is responsible for the 0.34 m radar echoes on the eastern wall and may also contribute to the echoes on the western wall.

Next, I presented work where we measured the separation of bottomside airglow depletions at Jicamarca and they were typically observed in groups separated by 400-500 km. The separation within the groups was typically 50-100 km. Previous studies have shown that large scale wave structures, with similar wavelengths to the group separation measure here, can impact the development of ESF plumes. The results from this study indicate that a LSWS may be modulating bottomside ESF depletions.

I used the movement of the bottomside depletions observed with an ASI at Jicamarca to measure the zonal plasma drift. The velocities were compared with zonal neutral wind measurements from a colocated FPI. Early in the night the speed of the depletions was greater than the neutral winds, a result attributed to downward drifts that modify the plasma velocity that results from the F-region dynamo.

The bottomside depletions observed at Jicamarca sometimes evolve into topside plumes that can be observed with ASIs at higher latitudes such as at El Leoncito and Villa de Leyva. We compared concurrent observations at Jicamarca and El Leoncito to look for a relationship between the bottomside and topside structures.

No difference in the ASI images was found between bottomside depletions that form topside plumes and those that do not. Groups of bottomside depletions observed at Jicamarca tended to only form one topside plume at El Leoncito. It is not clear whether the resulting plume is from one depletions within the group or a combination of them.

In the last section of Chapter 4 I examined a case at El Leoncito where a brightness wave associated with an MTM changed the characteristics of a topside airglow depletion. In this case, the BW passed over the depletion and the depletion became brighter than the background. Typically, when a BW passes over a topside depletion, there is no effect on the brightness of the depletion. A previous modeling study found that the conditions needed to produce a brightening of and ESF are a poleward meridional wind and converging zonal winds. The MTM and associated BW can produce these conditions and explains the airglow enhancement. This study brings together the work from Chapter 3 on the MTM and the work in Chapter 4 on ESF. These are typically unconnected phenomena that occur in overlapping regions but I have shown that they can interact. This connects two prominent features of the low-latitude upper atmosphere that are often considered separately.

The combined results of various aspects of ESF from this chapter help to create a more complete understanding of ESF. I have determined a relationship between small-scale size irregularities and I have expanded the knowledge of the formation and evolution of ESF, all active areas of study.

6.3 To what extent does the Earth's magnetic field influence magnetically conjugate observations of ESF?

This question is addressed in Chapter 5. The El Leoncito and Villa de Leyva ASIs in South America are located at opposite ends of magnetic field lines. This pair

of imagers can observe conjugate topside ESF depletions simultaneously. Observations from these two sites showed differences in the morphology and zonal velocities of airglow depletions. In regards to morphology, I compared the zonal width and latitudinal extent of airglow depletions.

In Section 5.2 I measure the width of depletions at conjugate locations by fitting a Gaussian curve. I found that depletions were wider at El Leoncito than at Villa de Leyva. I then map a depletion along magnetic fields to the opposite hemisphere and then the widths with the effects of the magnetic field removed are consistent. The differences between the sites are thus due to the weaker magnetic field strength at El Leoncito and the orientation of the magnetic field at each site.

In the investigation of the width it was found that the centers of the conjugate depletions where not perfectly conjugate, there was an offset of about 16 km. The altitude of emission for each site can impact how well they are aligned along field lines and for these cases the altitudes were determined with the BU airglow model using IRI-2016 and NRLMSISE-00 as inputs. These are climatological models that may not be accurately reproducing the upper atmospheric conditions on a given day. By adjusting the altitude of emission, the offset was removed and the widths were still consistent. This highlights the limitations of using empirical climatological models to determine emission altitude. Different offsets were observed at different latitudes indicating that the airglow emission altitude is not consistent throughout the image, a result that impacts the interpretation of airglow observations.

In Section 5.3 the latitudinal extent of conjugate depletions was found to be different. In the case presented the depletions reached higher magnetic apex altitudes at Villa de Leyva than at El Leoncito. Additionally, the brightness is much greater at Villa de Leyva. Model results from HWM-14 show that there is a northward meridional neutral wind that occurs in both hemispheres. Due to the angle of the

magnetic field lines and ion drag this wind is increasing the plasma density and lowering the altitude of 6300 Å emission at Villa de Leyva and it is decreasing the plasma density and raising the altitude of 6300 Å emission at El Leoncito. The depletions extend farther north in the northern hemisphere, in the same direction as the wind. Local conditions have been previously shown to alter ESF depletions in one hemisphere and not the other. I suggest that these winds are also extending the airglow depletions.

Finally, in Section 5.4 zonal velocities of depletions at the Villa de Leyva and El Leoncito are compared. I present three nights of data from different times of the year and on each night greater zonal velocities are found at El Leoncito than at Villa de Leyva. These depletions are travelling with the background plasma that moves as a result of $\mathbf{E} \times \mathbf{B}$ zonal drift. At El Leoncito the magnetic field is much weaker which contributes to the difference in the zonal drift. Additionally, previous results have shown both the difference in magnetic field strength and the tilted magnetic field of the Earth will affect how electric fields map along magnetic field lines. Those previous model results indicated that that the drift velocity should be 1.35 greater at El Leoncito than at Villa de Leyva, consistent with our measured velocity differences. The difference in velocity is attributed to weaker magnetic field at El Leoncito and the tilt of the Earth's magnetic field.

6.3.1 Overall Results

I have presented here results from three topics related to ESF and the MTM.

- I presented new observations of the MTM that better constrain its extent and morphology of the MTM. These results support the theory that the MTM is in part generated in the lower atmosphere.

- I showed the connection between the large-scale depletions (10-500 km) and small-scale irregularities (0.3-3 m) of ESF. I presented observations of grouping of bottomside depletions that may be due to a LSWS and along with additional results I provided new insights into the observation, development, evolution, and variability of ESF.

- I explained that differences in ESF morphology between magnetically conjugate points are due to different magnetic field strength and orientation and neutral winds.

Additionally, the two upper atmosphere processes that are focused on of this dissertation, ESF and the MTM, have been considered independently in the past but I have shown new results on the impact of the MTM on ESF. Together, all the results presented here provide new insight into the low-latitude and mid-latitude regions of the Earth's upper atmosphere.

References

Ajith, K. K., S. Tulasi Ram, M. Yamamoto, Y. Otsuka, and K. Niranjan (2016), On the fresh development of equatorial plasma bubbles around the midnight hours of June solstice, *Journal of Geophysical Research: Space Physics*, pp. 1–12, doi:10.1002/2016JA023024.

Akmaev, R. A. (2011), Whole atmosphere modeling: Connecting terrestrial and space weather, *Reviews of Geophysics*, *49*(4), RG4004, doi:10.1029/2011RG000364.

Akmaev, R. A., T. J. Fuller-Rowell, F. Wu, J. M. Forbes, X. Zhang, A. F. Anghel, M. D. Iredell, S. Moorthi, and H. M. Juang (2008), Tidal variability in the lower thermosphere: Comparison of Whole Atmosphere Model (WAM) simulations with observations from TIMED, *Geophysical Research Letters*, *35*(3), 1–5, doi:10.1029/2007GL032584.

Akmaev, R. a., F. Wu, T. J. Fuller-Rowell, and H. Wang (2009), Midnight temperature maximum (MTM) in Whole Atmosphere Model (WAM) simulations, *Geophysical Research Letters*, *36*(7), n/a–n/a, doi:10.1029/2009GL037759.

Akmaev, R. a., F. Wu, T. J. Fuller-Rowell, H. Wang, and M. D. Iredell (2010), Midnight density and temperature maxima, and thermospheric dynamics in Whole Atmosphere Model simulations, *Journal of Geophysical Research*, *115*(A8), A08,326, doi:10.1029/2010JA015651.

Appleton, E., and M. A. F. Barnett (1925), Local reflection of wireless waves from the upper atmosphere, *Nature*, *115*, 333–334, doi:10.1038/115333a0.

Appleton, E. V. (1946), Two Anomalies in the Ionosphere, doi:10.1038/157691a0.

Aveiro, H. C., and D. L. Hysell (2010), Three-dimensional numerical simulation of equatorial F region plasma irregularities with bottomside shear flow, *Journal of Geophysical Research: Space Physics*, *115*(A11), n/a–n/a, doi:10.1029/2010JA015602.

Bamgboye, D. K., and J. P. McClure (1982), Seasonal variation in the occurrence time of the equatorial midnight temperature bulge, *Geophysical Research Letters*, *9*(4), 457–460, doi:10.1029/GL009i004p00457.

Baumgardner, J., J. Wroten, J. Semeter, J. Kozyra, M. Buonsanto, P. Erickson, and M. Mendillo (2008), A very bright SAR arc: implications for extreme magnetosphere-ionosphere coupling, *Annales Geophysicae*, *25*(12), 2593–2608, doi:10.5194/angeo-25-2593-2007.

Baumgardner, J. L. (1993), Monochromatic imaging instrumentation for applications in aeronomy of the earth and planets, *Optical Engineering*, *32*(12), 3028, doi:10.1117/12.149194.

Behnke, R. A., and R. M. Harper (1973), Vector measurements of F region ion transport at Arecibo, *Journal of Geophysical Research*, *78*(34), 8222–8234, doi:10.1029/JA078i034p08222.

Bilitza, D. (2015), The International Reference Ionosphere – Status 2013, *Advances in Space Research*, *55*(8), 1914–1927, doi:10.1016/j.asr.2014.07.032.

Bilitza, D., D. Altadill, V. Truhlik, V. Shubin, I. Galkin, B. Reinisch, and X. Huang (2017), International Reference Ionosphere 2016: From ionospheric climate to real-time weather predictions, *Space Weather*, pp. 1–12, doi:10.1002/2016SW001593.

Booker, H. G., and H. W. Wells (1938), Scattering of radio waves by the F -region of the ionosphere, *Journal of Geophysical Research*, *43*(3), 249, doi:10.1029/TE043i003p00249.

Carlson, H. C. (1966), Ionospheric heating by magnetic conjugate-point photoelectrons, *Journal of Geophysical Research*, *71*(1), 195–199, doi:10.1029/JZ071i001p00195.

Chao, C. K., S.-Y. Su, and H. C. Yeh (2003), Presunrise ion temperature enhancement observed at 600 km low- and mid-latitude ionosphere, *Geophysical Research Letters*, *30*(4), 1187, doi:10.1029/2002GL016268.

Chapagain, N. P., M. J. Taylor, and J. V. Eccles (2011), Airglow observations and modeling of F region depletion zonal velocities over Christmas Island, *Journal of Geophysical Research: Space Physics*, *116*(2), doi:10.1029/2010JA015958.

Chapagain, N. P., D. J. Fisher, J. W. Meriwether, J. L. Chau, and J. J. Makela (2013), Comparison of zonal neutral winds with equatorial plasma bubble and plasma drift velocities, *Journal of Geophysical Research: Space Physics*, *118*(4), 1802–1812, doi:10.1002/jgra.50238.

Colerico, M., et al. (1996), Coordinated measurements of F region dynamics related to the thermospheric midnight temperature maximum, *Journal of Geophysical Research: Space Physics*, *101*(A12), 26,783–26,793, doi:10.1029/96JA02337.

Colerico, M. J., M. Mendillo, C. G. Fesen, and J. Meriwether (2006), Comparative investigations of equatorial electrodynamics and low-to-mid latitude coupling of the thermosphere-ionosphere system, *Annales Geophysicae*, *24*(2), 503–513, doi:10.5194/angeo-24-503-2006.

Crary, D. J., and J. M. Forbes (1986), The dynamic ionosphere over Arecibo: A theoretical investigation, *Journal of Geophysical Research*, *91*(A1), 249, doi:10.1029/JA091iA01p00249.

Demyanov, V. V., Y. V. Yasyukevich, A. B. Ishin, and E. I. Astafyeva (2012), Ionospheric super-bubble effects on the GPS positioning relative to the orientation of signal path and geomagnetic field direction, *GPS Solutions*, *16*(2), 181–189, doi:10.1007/s10291-011-0217-9.

Drob, D. P., et al. (2015), An Update to the Horizontal Wind Model (HWM): The Quiet Time Thermosphere, *Earth and Space Science*, pp. n/a–n/a, doi:10.1002/2014EA000089.

Evans, J. (1969), Theory and practice of ionosphere study by Thomson scatter radar, *Proceedings of the IEEE*, *57*(4), 496–530, doi:10.1109/PROC.1969.7005.

Evans, J. V., and I. J. Gastman (1970), Detection of conjugate photoelectrons at Millstone Hill, *Journal of Geophysical Research*, *75*(4), 807–815, doi:10.1029/JA075i004p00807.

Faivre, M., J. W. Meriwether, C. G. Fesen, and M. a. Biondi (2006), Climatology of the midnight temperature maximum phenomenon at Arequipa, Peru, *Journal of Geophysical Research*, *111*(A6), A06,302, doi:10.1029/2005JA011321.

Fejer, B. G., L. Scherliess, and E. R. de Paula (1999), Effects of the vertical plasma drift velocity on the generation and evolution of equatorial spread F, *Journal of Geophysical Research: Space Physics*, *104*(A9), 19,859–19,869, doi:10.1029/1999JA900271.

Fesen, C. G. (1996), Simulations of the low-latitude midnight temperature maximum, *Journal of Geophysical Research*, *101*(A12), 26,863–26,874, doi:10.1029/96JA01823.

Fesen, C. G., G. Crowley, R. G. Roble, A. D. Richmond, and B. G. Fejer (2000), Simulation of the pre-reversal enhancement in the low latitude vertical ion drifts, *Geophysical Research Letters*, *27*(13), 1851–1854, doi:10.1029/2000GL000061.

Fukushima, D., K. Shiokawa, Y. Otsuka, M. Nishioka, M. Kubota, T. Tsugawa, T. Nagatsuma, S. Komonjinda, and C. Y. Yatini (2015), Geomagnetically conjugate observation of plasma bubbles and thermospheric neutral winds at low latitudes, *Journal of Geophysical Research: Space Physics*, *120*(3), 2222–2231, doi:10.1002/2014JA020398.

Glassmeier, K.-H., and B. T. Tsurutani (2014), Carl friedrich gauss - general theory of terrestrial magnetism - a revised translation of the german text, *History of Geo- and Space Sciences*, *5*(1), 11–62, doi:10.5194/hgss-5-11-2014.

Gong, Y., Q. Zhou, S. Zhang, N. Aponte, M. Sulzer, and S. Gonzalez (2012), Midnight ionosphere collapse at Arecibo and its relationship to the neutral wind, electric field, and ambipolar diffusion, *Journal of Geophysical Research: Space Physics*, *117*(A8), n/a–n/a, doi:10.1029/2012JA017530.

Gordon, W. E. (1964), Arecibo Ionospheric Observatory: Studies of the upper atmosphere and planets are made with the aid of a huge reflector in Puerto Rico, *Science*, *146*(3640), 26–30, doi:10.1126/science.146.3640.26.

Green, A. (1974), Early history of the ionosphere, *Journal of Atmospheric and Terrestrial Physics*, *36*(12), 2159 – 2165, doi:https://doi.org/10.1016/0021-9169(74)90146-9, fifty Years of the Ionosphere.

Harper, R. (1973), Nighttime meridional neutral winds near 350 km at low to mid-latitudes, *Journal of Atmospheric and Terrestrial Physics*, *35*(11), 2023–2034, doi:10.1016/0021-9169(73)90116-5.

Herrero, F. A., and N. W. Spencer (1982), On the horizontal distribution of the equatorial thermospheric midnight temperature maximum and its seasonal variation, *Geophysical Research Letters*, *9*(10), 1179–1182, doi:10.1029/GL009i010p01179.

Hickey, D. A., C. R. Martinis, P. J. Erickson, L. P. Goncharenko, J. W. Meriwether, R. Mesquita, W. L. Oliver, and A. Wright (2014), New radar observations of temporal and spatial dynamics of the midnight temperature maximum at low latitude and midlatitude, *Journal of Geophysical Research: Space Physics*, *119*(12), 10,499–10,506, doi:10.1002/2014JA020719.

Hickey, D. A., C. R. Martinis, F. S. Rodrigues, R. H. Varney, M. A. Milla, M. J. Nicolls, A. Strømme, and J. F. Arratia (2015), Concurrent observations at the magnetic equator of small-scale irregularities and large-scale depletions associated with equatorial spread F, *Journal of Geophysical Research A: Space Physics*, *120*(12), doi:10.1002/2015JA021991.

Hickey, D. A., C. R. Martinis, M. Mendillo, J. Baumgardner, J. Wroten, and M. Milla (2018), Simultaneous 6300 å airglow and radar observations of ionospheric irregularities and dynamics at the geomagnetic equator, *Annales Geophysicae*, *36*(2), 473–487, doi:10.5194/angeo-36-473-2018.

Huang, C.-S., and M. C. Kelley (1996), Nonlinear evolution of equatorial spread F : 1. On the role of plasma instabilities and spatial resonance associated with gravity wave seeding, *Journal of Geophysical Research: Space Physics*, *101*(A1), 283–292, doi:10.1029/95JA02211.

Huang, C.-S., O. de La Beaujardiere, P. A. Roddy, D. E. Hunton, J. O. Ballenthin, and M. R. Hairston (2012), Generation and characteristics of equatorial plasma bubbles detected by the C/NOFS satellite near the sunset terminator, *Journal of Geophysical Research: Space Physics*, *117*(A11), n/a–n/a, doi:10.1029/2012JA018163.

Huba, J., and S. Ossakow (1979), On the generation of 3-m irregularities during equatorial spread F by low-frequency drift waves, *Journal of Geophysical Research*, *84*(A11), 6697, doi:10.1029/JA084iA11p06697.

Huba, J., and S. Ossakow (1981a), Physical mechanism of the lower-hybrid-drift instability in a collisional plasma, *Journal of Atmospheric and Terrestrial Physics*, *43*(8), 775 – 778, doi:https://doi.org/10.1016/0021-9169(81)90053-2, equatorial Aeronomy - II.

Huba, J. D., and J. Krall (2013), Impact of meridional winds on equatorial spread F: Revisited, *Geophysical Research Letters*, *40*(7), 1268–1272, doi:10.1002/grl.50292.

Huba, J. D., and S. L. Ossakow (1981b), On 11-cm irregularities during equatorial spread F, *Journal of Geophysical Research*, *86*(A2), 829, doi:10.1029/JA086iA02p00829.

Hysell, D. (2000), An overview and synthesis of plasma irregularities in equatorial spread F, *Journal of Atmospheric and Solar-Terrestrial Physics*, *62*(12), 1037–1056, doi:10.1016/S1364-6826(00)00095-X.

Hysell, D., and J. Burcham (2002), Long term studies of equatorial spread F using the JULIA radar at Jicamarca, *Journal of Atmospheric and Solar-Terrestrial Physics*, *64*(12-14), 1531–1543, doi:10.1016/S1364-6826(02)00091-3.

Hysell, D. L. (1996), Radar imaging of equatorial F region irregularities with maximum entropy interferometry, *Radio Science*, *31*(6), 1567–1578, doi:10.1029/96RS02334.

Hysell, D. L., and J. L. Chau (2006), Optimal aperture synthesis radar imaging, *Radio Science*, *41*(2), n/a–n/a, doi:10.1029/2005RS003383.

Hysell, D. L., R. B. Hedden, J. L. Chau, F. R. Galindo, P. a. Roddy, and R. F. Pfaff (2009), Comparing F region ionospheric irregularity observations from C/NOFS and Jicamarca, *Geophysical Research Letters*, *36*(18), 1–5, doi:10.1029/2009GL038983.

Immel, T. J., E. Sagawa, S. L. England, S. B. Henderson, M. E. Hagan, S. B. Mende, H. U. Frey, C. M. Swenson, and L. J. Paxton (2006), Control of equatorial ionospheric morphology by atmospheric tides, *Geophysical Research Letters*, *33*(15), n/a–n/a, doi:10.1029/2006GL026161, l15108.

Joshi, L. M. (2016), LSWS linked with the low-latitude E s and its implications for the growth of the R-T instability, *Journal of Geophysical Research: Space Physics*, pp. 1–26, doi:10.1002/2016JA022659.

Kelley, M., and D. Hysell (1991), Equatorial spread-F and neutral atmospheric turbulence : a review and a comparative anatomy, *Journal of Atmospheric and Terrestrial Physics*, *53*(8), 695–708, doi:10.1016/0021-9169(91)90122-N.

Kelley, M. C., J. J. Makela, L. J. Paxton, F. Kamalabadi, J. M. Comberiate, and H. Kil (2003), The first coordinated ground- and space-based optical observations of equatorial plasma bubbles, *Geophysical Research Letters*, *30*(14), 1766, doi:10.1029/2003GL017301.

Kelley, M. C., R. R. Ilma, and G. Crowley (2009), On the origin of pre-reversal enhancement of the zonal equatorial electric field, *Annales Geophysicae*, *27*(5), 2053–2056, doi:10.5194/angeo-27-2053-2009.

Kelly, M. a., J. M. Comberiate, E. S. Miller, and L. J. Paxton (2014), Progress toward forecasting of space weather effects on UHF SATCOM after Operation Anaconda, *Space Weather*, *12*(10), 601–611, doi:10.1002/2014SW001081.

Keskinen, M. J., S. L. Ossakow, S. Basu, and P. J. Sultan (1998), Magnetic-flux-tube-integrated evolution of equatorial ionospheric plasma bubbles, *Journal of Geophysical Research: Space Physics*, *103*(A3), 3957–3967, doi:10.1029/97JA02192.

Kil, H., R. A. Heelis, L. J. Paxton, and S. J. Oh (2009), Formation of a plasma depletion shell in the equatorial ionosphere, *Journal of Geophysical Research: Space Physics*, *114*(11), 1–7, doi:10.1029/2009JA014369.

Krall, J., J. D. Huba, and C. R. Martinis (2009a), Three-dimensional modeling of equatorial spread F airglow enhancements, *Geophysical Research Letters*, *36*(10), 3–6, doi:10.1029/2009GL038441.

Krall, J., J. D. Huba, G. Joyce, and S. T. Zalesak (2009b), Three-dimensional simulation of equatorial spread-F with meridional wind effects, *Annales Geophysicae*, *27*(5), 1821–1830, doi:10.5194/angeo-27-1821-2009.

Laundal, K. M., and A. D. Richmond (2017), Magnetic Coordinate Systems, *Space Science Reviews*, *206*(1-4), 27–59, doi:10.1007/s11214-016-0275-y.

Makela, J. J., and M. C. Kelley (2003), Field-aligned 777.4-nm composite airglow images of equatorial plasma depletions, *Geophysical Research Letters*, *30*(8), 1–4, doi:10.1029/2003GL017106.

Makela, J. J., S. L. Vadas, R. Muryanto, T. Duly, and G. Crowley (2010), Periodic spacing between consecutive equatorial plasma bubbles, *Geophysical Research Letters*, *37*(14), 1–5, doi:10.1029/2010GL043968.

Makela, J. J., J. W. Meriwether, A. J. Ridley, M. Ciocca, and M. W. Castellez (2012), Large-Scale Measurements of Thermospheric Dynamics with a Multisite Fabry-Perot Interferometer Network: Overview of Plans and Results from Midlatitude Measurements, *International Journal of Geophysics*, *2012*(3), 1–10, doi:10.1155/2012/872140.

Martinis, C., and M. Mendillo (2007), Equatorial spread F-related airglow depletions at Arecibo and conjugate observations, *Journal of Geophysical Research: Space Physics*, *112*(A10), n/a–n/a, doi:10.1029/2007JA012403.

Martinis, C., J. V. Eccles, J. Baumgardner, J. Manzano, and M. Mendillo (2003), Latitude dependence of zonal plasma drifts obtained from dual-site airglow observations, *Journal of Geophysical Research*, *108*(A3), 1129, doi:10.1029/2002JA009462.

Martinis, C., J. Baumgardner, S. M. Smith, M. Colerico, and M. Mendillo (2006), Imaging science at El Leoncito, Argentina, *Annales Geophysicae*, *24*(5), 1375–1385, doi:10.5194/angeo-24-1375-2006.

Martinis, C., J. Baumgardner, M. Mendillo, S. Y. Su, and N. Aponte (2009), Brightening of 630.0 nm equatorial spread-F airglow depletions, *Journal of Geophysical Research: Space Physics*, *114*(6), 1–9, doi:10.1029/2008JA013931.

Martinis, C., D. Hickey, W. Oliver, N. Aponte, C. Brum, R. Akmaev, A. Wright, and C. Miller (2013), The midnight temperature maximum from Arecibo incoherent scatter radar ion temperature measurements, *Journal of Atmospheric and Solar-Terrestrial Physics*, *103*, 129–137, doi:10.1016/j.jastp.2013.04.014.

Mendillo, M., and J. Baumgardner (1982), Airglow characteristics of equatorial plasma depletions, *Journal of Geophysical Research*, *87*(A9), 7641, doi:10.1029/JA087iA09p07641.

Mendillo, M., E. Zesta, S. Shodhan, P. J. Sultan, R. Doe, Y. Sahai, and J. Baumgardner (2005), Observations and modeling of the coupled latitude-altitude patterns of equatorial plasma depletions, *Journal of Geophysical Research: Space Physics*, *110*(A9), 1–7, doi:10.1029/2005JA011157.

Meriwether, J., M. Faivre, C. Fesen, P. Sherwood, and O. Veliz (2008), New results on equatorial thermospheric winds and the midnight temperature maximum, *Annales Geophysicae*, *26*(3), 447–466, doi:10.5194/angeo-26-447-2008.

Meriwether, J., J. Makela, D. Fisher, R. Buriti, a.F. Medeiros, R. Akmaev, T. Fuller-Rowell, and F. Wu (2013), Comparisons of thermospheric wind and temperature measurements in equatorial Brazil to Whole Atmosphere Model Predictions, *Journal of Atmospheric and Solar-Terrestrial Physics*, *103*, 103–112, doi:10.1016/j.jastp.2013.04.002.

Meriwether, J. W., J. J. Makela, Y. Huang, D. J. Fisher, R. A. Buriti, A. F. Medeiros, and H. Takahashi (2011), Climatology of the nighttime equatorial thermospheric winds and temperatures over Brazil near solar minimum, *Journal of Geophysical Research: Space Physics*, *116*(A4), n/a–n/a, doi:10.1029/2011JA016477.

Miller, E. S., J. J. Makela, K. M. Groves, M. C. Kelley, and R. T. Tsunoda (2010), Coordinated study of coherent radar backscatter and optical airglow depletions in the central Pacific, *Journal of Geophysical Research: Space Physics*, *115*(A6), n/a–n/a, doi:10.1029/2009JA014946.

Narayanan, V. L., A. Taori, A. K. Patra, K. Emperumal, and S. Gurubaran (2012), On the importance of wave-like structures in the occurrence of

equatorial plasma bubbles: A case study, *Journal of Geophysical Research: Space Physics*, *117*(1), 1–8, doi:10.1029/2011JA017054.

Nelson, G., and L. Cogger (1971), Dynamical behaviour of the nighttime ionosphere at Arecibo, *Journal of Atmospheric and Terrestrial Physics*, *33*(11), 1711–1726, doi:10.1016/0021-9169(71)90219-4.

Ochs, G. (1960), The large 50 mc/s dipole array at Jicamarca radio observatory, in *1963 Antennas and Propagation Society International Symposium*, vol. 1, pp. 237–241, Institute of Electrical and Electronics Engineers, doi:10.1109/APS.1963.1148638.

Oliver, W. L. (1984), Millstone Hill incoherent scatter observations of exospheric temperature over 25 to 60 degrees north latitude, *Geophysical Research Letters*, *11*(9), 915–918, doi:10.1029/GL011i009p00915.

Oliver, W. L., C. R. Martinis, D. a. Hickey, a. D. Wright, and C. Amory-Mazaudier (2012), A nighttime temperature maximum in the thermosphere above Saint Santin in winter, *Journal of Geophysical Research: Space Physics*, *117*(A6), n/a–n/a, doi:10.1029/2012JA017855.

Otsuka, Y., K. Shiokawa, T. Ogawa, and P. Wilkinson (2002), Geomagnetic conjugate observations of equatorial airglow depletions, *Geophysical Research Letters*, *29*(15), 43–1–43–4, doi:10.1029/2002GL015347.

Otsuka, Y., K. Shiokawa, T. Ogawa, T. Yokoyama, M. Yamamoto, and S. Fukao (2004), Spatial relationship of equatorial plasma bubbles and field-aligned irregularities observed with an all-sky airglow imager and the Equatorial Atmosphere Radar, *Geophysical Research Letters*, *31*(20), L20,802, doi:10.1029/2004GL020869.

Park, J., C. R. Martinis, H. Lühr, R. F. Pfaff, and Y.-S. Kwak (2016), Hemispheric asymmetry in transition from equatorial plasma bubble to blob as deduced from 630.0 nm airglow observations at low latitudes, *Journal of Geophysical Research: Space Physics*, *121*(1), 881–893, doi:10.1002/2015JA022175.

Patra, A. K., A. Taori, P. P. Chaitanya, and S. Sripathi (2013), Direct detection of wavelike spatial structure at the bottom of the F region and its role on the formation of equatorial plasma bubble, *Journal of Geophysical Research: Space Physics*, *118*(3), 1196–1202, doi:10.1002/jgra.50148.

Picone, J. M., A. E. Hedin, D. P. Drob, and A. C. Aikin (2002), NRLMSISE-00 empirical model of the atmosphere: Statistical comparisons and scientific issues, *Journal of Geophysical Research: Space Physics*, *107*(A12), SIA 15–1–SIA 15–16, doi:10.1029/2002JA009430.

Pinto, O., W. Gonzalez, I. Pinto, A. Gonzalez, and O. Mendes (1992), The South Atlantic Magnetic Anomaly: three decades of research, *Journal of Atmospheric and Terrestrial Physics*, *54*(9), 1129–1134, doi:10.1016/0021-9169(92)90137-A.

Retterer, J. M. (2010), Forecasting low-latitude radio scintillation with 3-D ionospheric plume models: 1. Plume model, *Journal of Geophysical Research: Space Physics*, *115*(A3), n/a–n/a, doi:10.1029/2008JA013839.

Rino, C. L., C. S. Carrano, K. M. Groves, and P. A. Roddy (2016), A characterization of intermediate-scale spread F structure from four years of high-resolution C/NOFS satellite data, *Radio Science*, pp. 1–10, doi:10.1002/2015RS005841.

Rishbeth, H. (1971), Polarization fields produced by winds in the equatorial F-region, *Planetary and Space Science*, *19*(3), 357–369, doi:10.1016/0032-0633(71)90098-5.

Rishbeth, H. (1972), Thermospheric winds and the F-region: A review, *Journal of Atmospheric and Terrestrial Physics*, *34*(1), 1–47, doi:10.1016/0021-9169(72)90003-7.

Rodrigues, F. S., D. L. Hysell, and E. R. de Paula (2008), Coherent backscatter radar imaging in Brazil: large-scale waves in the bottomside F-region at the onset of equatorial spread <I>F</I>, *Annales Geophysicae*, *26*(11), 3355–3364, doi:10.5194/angeo-26-3355-2008.

Rodrigues, F. S., M. J. Nicolls, M. A. Milla, J. M. Smith, R. H. Varney, A. Strømme, C. Martinis, and J. F. Arratia (2015), AMISR-14: Observations of equatorial spread F, *Geophysical Research Letters*, *42*(13), 5100–5108, doi:10.1002/2015GL064574.

Rodrigues, F. S., D. A. Hickey, W. Zhan, C. R. Martinis, B. G. Fejer, M. A. Milla, and J. F. Arratia (2018), Multi-instrumented observations of the equatorial f-region during june solstice: large-scale wave structures and spread-f, *Progress in Earth and Planetary Science*, *5*(1), 14, doi:10.1186/s40645-018-0170-0.

Ruan, H., J. Lei, X. Dou, S.-R. Zhang, J. Noto, and S. Kapali (2013), Enhancements of nighttime neutral and ion temperatures in the F region over Millstone Hill, *Journal of Geophysical Research: Space Physics*, *118*(4), 1768–1776, doi:10.1002/jgra.50202.

Sekar, R., D. Chakrabarty, S. Sarkhel, A. K. Patra, C. V. Devasia, and M. C. Kelley (2007), Identification of active fossil bubbles based on coordinated

VHF radar and airglow measurements, *Annales Geophysicae*, *25*(10), 2099–2102, doi:10.5194/angeo-25-2099-2007.

Semeter, J., M. Mendillo, J. Baumgardner, J. Holt, D. E. Hunton, and V. Eccles (1996), A study of oxygen 6300 Å airglow production through chemical modification of the nighttime ionosphere, *Journal of Geophysical Research: Space Physics*, *101*(A9), 19,683–19,699, doi:10.1029/96JA01485.

Shiokawa, K., Y. Otsuka, T. Ogawa, and P. Wilkinson (2004), Time evolution of high-altitude plasma bubbles imaged at geomagnetic conjugate points, *Annales Geophysicae*, *22*(9), 3137–3143, doi:10.5194/angeo-22-3137-2004.

Spencer, N. W., G. R. Carignan, H. G. Mayr, H. B. Niemann, R. F. Theis, and L. E. Wharton (1979), The midnight temperature maximum in the Earth's equatorial thermosphere, *Geophysical Research Letters*, *6*(6), 444–446, doi:10.1029/GL006i006p00444.

Sultan, P. J. (1996), Linear theory and modeling of the Rayleigh-Taylor instability leading to the occurrence of equatorial spread F, *Journal of Geophysical Research: Space Physics*, *101*(A12), 26,875–26,891, doi:10.1029/96JA00682.

Thébault, E., et al. (2015), International Geomagnetic Reference Field: the 12th generation, *Earth, Planets and Space*, *67*(1), doi:10.1186/s40623-015-0228-9.

Tsunoda, R. T. (1980), Backscatter measurements of 11-cm equatorial spread-F irregularities, *Geophysical Research Letters*, *7*(10), 848–850, doi:10.1029/GL007i010p00848.

Tsunoda, R. T., and B. R. White (1981), On the generation and growth of equatorial backscatter plumes 1. Wave structure in the bottomside F layer, *Journal of Geophysical Research*, *86*(A5), 3610, doi:10.1029/JA086iA05p03610.

Weber, E. J., J. Buchau, R. H. Eather, and S. B. Mende (1978), North-south aligned equatorial airglow depletions, *Journal of Geophysical Research*, *83*(A2), 712, doi:10.1029/JA083iA02p00712.

Weber, E. J., et al. (1996), Equatorial plasma depletion precursor signatures and onset observed at 11 south of the magnetic equator, *Journal of Geophysical Research: Space Physics*, *101*(A12), 26,829–26,838, doi:10.1029/96JA00440.

Woodman, R. F. (2009), Spread F – an old equatorial aeronomy problem finally resolved?, *Annales Geophysicae*, *27*(5), 1915–1934, doi:10.5194/angeo-27-1915-2009.

Woodman, R. F., and C. La Hoz (1976), Radar observations of F region equatorial irregularities, *Journal of Geophysical Research*, *81*(31), 5447–5466, doi:10.1029/JA081i031p05447.

Yokoyama, T., H. Shinagawa, and H. Jin (2014), Nonlinear growth, bifurcation, and pinching of equatorial plasma bubble simulated by three-dimensional high-resolution bubble model, *Journal of Geophysical Research: Space Physics*, *119*(12), 10,474–10,482, doi:10.1002/2014JA020708.

Yue, X., W. S. Schreiner, Y. H. Kuo, and J. Lei (2015), Ionosphere equatorial ionization anomaly observed by GPS radio occultations during 2006-2014, *Journal of Atmospheric and Solar-Terrestrial Physics*, *129*(4), 30–40, doi:10.1016/j.jastp.2015.04.004.

Zhang, S. R., and J. M. Holt (2004), Ionospheric plasma temperatures during 1976-2001 over Millstone Hill, *Advances in Space Research*, *33*(6), 963–969, doi:10.1016/j.asr.2003.07.012.

Curriculum Vitae